Summer 9-1-2014

Investigation and Optimization of Extraordinary Electroconductance (EEC) Sensors & The Role of Magnetic Disorder in the Formation of Spin Glasses

Fletcher M. Werner
Washington University in St. Louis

WASHINGTON UNIVERSITY IN ST. LOUIS

Department of Physics

Dissertation Examination Committee:
Stuart A. Solin, Chair
Parag Banerjee
James Buckley
Tyrone Daulton
Viktor Gruev
Zohar Nussinov

Investigation and Optimization of Extraordinary Electroconductance (EEC) Sensors & The Role of Magnetic Disorder in the Formation of Spin Glasses

by

Fletcher M. Werner

A dissertation presented to the
Graduate School of Arts and Sciences
of Washington University in St. Louis
in partial fulfillment of the
requirement of the degree
of Doctor of Philosophy.

August 2014

St. Louis, Missouri

Contents

PART II: The Role of Magnetic Disorder in the Formation of Spin Glasses

List of Figures

List of Tables

Acknowledgements

I am deeply grateful for the network of support and encouragement that made this thesis and PhD possible. Funding was supplied, in part, by the National Science Foundation (NSF Grant # ECCS-0725538) and National Institute of Health (NIH Grant #1U54CA11934201).

First, I would like to thank my advisor, Prof. Stuart Solin. His methodical and determined approach to problem-solving has been the model that I have attempted to follow over the past five years. His generous support and patience have made it possible to explore many interesting subjects, while his knowledge and focus have helped to bind those subjects into a coherent body of work.

I would like to thank former group members Lauren Tran and Jian Wu, who helped make this research enjoyable and acted as mentors in their respective fields. I also extend my appreciation to the previous members of our group, upon whose shoulders I have stood. I thank the PixelEXX group, specifically Ken Bradley, Renee Carder and Chris Knutson, for their funding and collaborative efforts.

I would like to thank Tyrone Daulton and Anup Gangopadhyay for their training on the SEM and PPMS, respectively. I am indebted to Nathan Reed for his extensive clean room training and aid in trouble-shooting. I would also like to thank Prof. James Buckley, Prof. Henric Krawczynski, Prof. James Schilling and Dr. Sam Wickline for allowing me to use the experimental facilities in their labs.

I owe much of my academic success to my parents and appreciate all of the sacrifices they have made throughout my life to make this opportunity possible. To my mom, for instilling

in me the belief that I was capable of accomplishing anything I set my mind to and to my dad, whose motto of ‘think smarter, not harder’ has been a guiding principle throughout this work.

A special thanks to my wife, Annie Werner. Her unfaltering support and encouragement have helped me overcome many of the challenges in the lab. I am inspired by her focus, work ethic and intelligence. Her persistence is also a major factor in my timely completion of this work and for that I am most thankful.

Finally, I dedicate this thesis to the memory of my sister Ginny Thomas, who always believed that I would someday earn a patched corduroy jacket.

Preface

Some chapters have been previously published as follows:

- Part I – Chapter 5: Photoeffects at the Schottky Interface in Extraordinary Optoconductance, L.C. Tran, F. M. Werner, A.K.M. Newaz and S. A. Solin, Journal of Applied Physics **114**, 153110 (2013)

- Part II – Chapter 4: Spin glassiness and power law scaling in anisotropic triangular spin-1/2 antiferromagnets, Jian Wu, Julia S. Wildeboer, Fletcher Werner, Alexander Seidel, Z. Nussinov and S.A. Solin, European Physics Letters **93**, 67001 (2011)

ABSTRACT OF THE DISSERTATION

Investigation and Optimization of Extraordinary Electroconductance (EEC) Sensors

&

The Role of Magnetic Disorder in the Formation of Spin Glasses

by

Fletcher M. Werner

Doctor of Philosophy in Physics

Washington University in St. Louis, 2014

Professor Stuart A. Solin, Chair

PART I: Investigation and Optimization of Extraordinary Electroconductance (EEC) Sensors

This thesis presents an investigation and geometric optimization of Extraordinary Electroconductance (EEC) sensors, a member of an established class of sensors that exhibit 'extraordinary' phenomenon driven by interfaces that maximize current redistribution under an applied perturbation. EEC sensors are responsive to both applied electrical fields and optical illumination and show promising application in the detection of complex biological signals that can aid in conclusive diagnoses.

The EEC device response to nonuniform illumination establishes greater versatility for EEC devices by allowing for position-dependent light sensing while under local illumination. Additionally, an enhanced light responsivity of EEC sensors via modification of shunt geometry, as well as a bifurcation in sensor response to direct reverse bias and light irradiance based on measurement lead location was observed. Significantly increased light responsivity was achieved by simultaneously biasing the EEC device while exposing to light, resulting in an over

614% increase in resistance from 11mW/cm^2 irradiance of HeNe laser light and maximum a specific detectivity of $D^* = 3.67 \times 10^{11}$ cm$\sqrt{\text{Hz}}$/W.

PART II: The Role of Magnetic Disorder in the Formation of Spin Glasses

This thesis presents data on the magnetic properties of two classes of layered spin S=1/2 antiferromagnetic quasi-triangular lattice materials: $Cu_{2(1-x)}Zn_{2x}(OH)_3NO_3$ ($0 \leq x \leq 0.65$) and its long organic chain intercalated derivatives $Cu_{2(1-x)}Zn_{2x}(OH)_3C_7H_{15}COO.mH_2O$ ($0 \leq x \leq 0.29$), where non-magnetic Zn substitutes for Cu isostructurally. It is found that the intercalated compounds, even in a clean system in the absence of dilution, *x*=0, show spin-glass behavior, as evidenced by DC and AC susceptibility measurements, and by time dependent magnetization measurements. A striking feature is the observation of a sharp crossover between two successive power law regimes in the DC susceptibility above the freezing temperature. In contrast to standard theoretical expectations, these power laws are insensitive to doping. Specific heat data are consistent with a conventional phase transition in the unintercalated compounds, and glassy behavior in the intercalated compounds.

The emergence of a cluster spin glass under no imposed magnetic disorder suggests that the historical assumption that magnetic disorder is required to form a spin glass may be wrong. Research into additional examples of non-diluted spin glasses should lend phenomenological insight into the factors driving the frustrated magnetic system into a spin glass phase.

PART I

Investigation and Optimization of Extraordinary Electroconductance (EEC) Sensors

1 Introduction to Extraordinary Electroconductance Sensors

1.1 Background and Motivation

Since the invention of the point-contact transistor by John Bardeen, Walter Brattain and William Schockley in 1947 [1], the field of solid state sensor technology has rapidly expanded, with current research ranging from maintaining the advancement of Moore's Law [2] to the development of "lab-on-a-chip" devices [3], i.e. low-cost and easily transported diagnostic tools capable of detecting the presence of biologically relevant material in a complex organic suspension. The following chapters of this thesis will present the fundamental material physics of metal-semiconductor hybrid (MSH) sensors and new research concerning the development of a class of geometrically driven MSH sensors with future application as biosensors and detectors.

The motivation behind the research presented in this thesis is the investigation and geometric optimization of an established class of sensors. These sensors fall under a family of sensors exhibiting 'extraordinary' phenomenon driven by interfaces that are geometrically optimized to maximize current redistribution under an applied perturbation. To date, this class of phenomenon includes the following: extraordinary magnetoresistance (EMR) [4] [5], extraordinary piezoconductance (EPC) [6], extraordinary optoconductance (EOC) [7] [8], inverse extraordinary optoconductance (I-EOC) [9] and extraordinary electroconductance (EEC) [10] [11]. While the main body of the research presented in this thesis focuses on EEC sensors, a discussion of all extraordinary phenomenon, collectively referred to as EXX, will be included in Part I, Section 3 – Metal Semiconductor Hybrid (MSH) Devices.

1.2 Outline of Part I

Following this Introduction, Part I of this thesis is organized as follows: Section 2 will present the relevant fundamentals concerning the physics and properties of solids with focus

placed on metals and semiconductors. Specifically, the charge carrier transport dynamics of metals will be presented, with historical theories (as well as the failures of those theories) discussed. Much of this section will be devoted to elucidating semiconductor physics, starting with the fundamentals of crystal structure and formation of energy bands to carrier transport properties and light-matter interactions. The discussion will follow Ref. [12] when relevant.

Section 3 will introduce the fundamentals of MSH devices with a discussion of metal-semiconductor junctions, followed by two common MSH devices. The discussion will follow reference [13] when relevant. This section will also include a full discussion of all the different EXX devices developed to date.

Section 4 will present the techniques involved in the fabrication of EEC sensors. The fabrication of micron-scale EEC sensors was accomplished entirely at Washington University within the University's Nano Research Facility (NRF) and Institute of Materials Science & Engineering (IMSE).

Section 5 will present collaborative research that studied the responsivity of EEC sensors to non-uniform illumination [14]. While the bulk of this section is from a previously published paper, an addendum has been added that presents unpublished material as of the date this thesis was written, showing the open-circuit voltage response of an EEC sensor to local light irradiance.

Section 6 will present research into optimizing the EEC sensor response to uniform optical illumination. This research explores the influence of shunt geometry on sensor responsivity, investigates the influence of relative lead location on the performance of EEC sensors and establishes a tunable responsivity to light. This research achieves a significantly enhanced light responsivity to uniform light illumination previously unobserved in EEC sensor.

Finally, some closing statements will be made concerning the current and future progress in EEC device optimization.

2 Physics and Properties of Solids

2.1 Classification of Solids

Broadly speaking, solids can be organized based on their conductive properties into the following three categories: conductors (or metals), semiconductors and insulators. Conductors are characterized by their excellent electrical conductivity, while insulators represent the other extreme end of the conductive spectrum, having very low electrical conductivity. Semiconductors have an electrical conductivity that lies somewhere between these two extremes and are simultaneously both poor conductors and poor insulators.

2.2 Metals

Metals exhibit excellent thermal and electrical conductivity. Many metals are malleable and ductile, allowing them to be shaped into useful structures or pulled into conductive wires of tunable gauge. These properties account for the high utility of metals and the pressing demand for a theoretical model to account for their useful properties. The following will present, in historical order, the two major theories used to model the electrical properties of metals as well as address the limitations and failures of these models.

2.2.1.1 Drude Theory of *Metals*

In 1900, following the discovery of the electron by J.J. Thompson in 1897, Paul Drude published his theory of metallic conduction, in which he treated a metal as a gas of electrons and analyzed their properties by applying the kinetic theory of gases [15]. The kinetic theory of gases assumes that the molecules of the gas are all identical, spherical particles, travelling in straight lines until they collide and scatter off of one another. These collisions occur over an infinitesimal amount of time and, after the collision, the scattered molecules resume their ballistic travel. Aside from these intermittent collisions, the model assumes no other forces interact between the particles.

Drude's model assumes that the "molecules" in the system are the valence electrons of the metal that are loosely bound to the nuclei and can move relatively freely through the solid. In the context of a metal, these electrons are referred to as the *conduction* electrons. In order to achieve net charge neutrality, the conduction electrons' negative charge is compensated by positive ions within the metal structure. The positive ions have a very limited mobility and can be considered fixed in the context of this thesis. It is tempting to assume that the scattering inherent to the kinetic theory of gases must also occur between the conduction electrons and the positive ions. While Drude initially proposed this as a reasonable explanation to account for electron scattering, it cannot be the case. The scattering is assumed to occur over a negligible amount of time, while scattering between charges must follow a Coulombic force interaction of $1/r^2$. When the conduction electrons are treated as having no interaction with the positive ions of the system, this treatment is defined as the *free electron approximation*. The scattering mechanism is left as an unknown

If an external field is applied to the system, each conduction electron in the system is assumed to respond to the field following Newton's law of motion. If the complex interaction between the electrons is also ignored, this is termed the *independent electron approximation*. Electron scattering within the system occurs randomly, with an average characteristic time, τ, between scattering events for any one electron. This time is referred to as the relaxation time, collision time or mean free time and represents the amount of time, on average, that an electron will have travelled after its last collision. These collisions also serve as the means by which the electrons achieve thermal equilibrium with their surroundings. The collisions are assumed to remove any history of the electron, resulting in a recently collided electron having a velocity independent of its velocity and position prior to the collision.

It is worth discussing the density of the electron gas. A metallic element contains Avogadro's number of atoms per mole, i.e. 6.022 x 10^{23} atoms/mole. The volume of one mole of an atomic element can be found by taking the atomic mass, A, and dividing by the metal's density, ρ_m,, i.e. $V_{mol} = \rho_m/A$. If we define the number of valence electrons per atom as Z, then the number of electrons per cubic centimeter is given by

$$n = 6.022 \times 10^{23} \frac{Z\rho_m}{A} \quad \textbf{(1)}$$

For copper, this yields a conduction electron density of 8.47 x $10^{22}/cm^3$. This density is ~10^3 larger than those found in typical gases at standard temperature and pressure (STP) [12]. Another common way of expressing the electronic density is by calculating the radius, r_s, of a sphere whose volume, v_s, is equal to the volume per conduction electron, i.e.

$$v_s = \frac{V}{N} = \frac{1}{n} \rightarrow r_s = \left(\frac{3}{4\pi n}\right)^{1/3} \quad \textbf{(2)}$$

For copper, this value is 1.41 Å or $2.67a_0$, where a_0 is the Bohr radius, defined as $a_0=\hbar^2/m_e e^2$.

Having established the key assumptions of the Drude Theory, it is possible to theoretically predict the DC conductivity of a metal. The microscopic form of Ohm's Law is given as

$$\vec{j} = \sigma\vec{E}, \quad \textbf{(3)}$$

where $\vec{j}$ is the current density vector, $\vec{E}$ is the imposed electric field and σ is the material conductivity.

If an electric field is present, it will act on each electron according to Newton's Law of motion. That is,

$$m_e\vec{a} = -e\vec{E} \quad \textbf{(4)}$$

where $\boldsymbol{m_e}$ is the electron mass, $\vec{\boldsymbol{a}}$ is the acceleration, $\boldsymbol{e}$ is the absolute value of the charge of the electron and $\vec{\boldsymbol{E}}$ is the imposed electric field. The acceleration of an individual electron will be

$$\vec{a} = \frac{-e\vec{E}}{m_e} \quad \textbf{(5)}$$

Since the average time between collisions is given as the mean free time, τ, the average velocity must be the product of the acceleration and τ, ie

$$\vec{v} = \vec{a}\tau = \frac{-e\tau}{m_e}\vec{E} = \mu\vec{E}, \quad \textbf{(6)}$$

where μ is defined as the electron mobility and characterizes how well a current carrying element in a material can move when acted on by an electric field.

If *n* electrons per unit volume all move with velocity v, parallel to the electric field, then this motion of charge will give rise to a current density, *j*, that will also be parallel to the electric field. In a given time *dt*, $nvdtA$ electrons with charge *–e* will have travelled across an area *A*. Thus,

$$\vec{j} = -ne\vec{v} = \frac{ne^2\tau}{m_e}\vec{E} = ne\mu\vec{E} \quad \textbf{(7)}$$

Comparing Eqs (3) and (7), we find that

$$\sigma = \frac{ne^2\tau}{m_e} = ne\mu \equiv \frac{1}{\rho} \quad \textbf{(8)}$$

If the conductivity (or inversely, the resistivity, ρ) of a material is known, along with the charge density, it is possible to calculate the mean free time, τ, which is usually 10^{-14}-10^{-15}

seconds at room temperature for metals [12]. The resistivity of copper at room temperature is 1.56 μΩ-cm [12]. Therefore, calculated mean free time for copper at room temperature is 2.7 x 10^{-14} seconds. When Drude first worked out his theory, it was assumed that the electron system behaved classically. It was therefore reasonable to estimate the velocity of the conduction electrons from classical equipartion of energy, i.e. $^1/_2\, m_e v^2 = {}^3/_2\, k_B T$, where k_B is the Boltzmann constant. Knowing the mass of the electron, this estimates a room temperature velocity ~10^7 cm/s and a mean-free path of $l = v\tau \sim 1 - 10$ Å. This would be a reasonable estimate for the mean free path if the scattering were due to scattering off of the ions (interatomic spacing in metals ~angstroms), however that violates that assumption that scattering occurs over a negligible amount of time. Also, the actual mean-free path length in a metal at room temperature is known to be least an order of magnitude larger. Furthermore, larger mean-free path lengths can be achieved at lower temperature, which contradicts the inverse temperature behavior predicted by the velocity's dependence on temperature, as shown above.

A major fault in the Drude Theory was that it assumes a classical Maxwell-Boltzmann velocity distribution, which is not applicable for elementary particles that exhibit quantum mechanical behavior. It would take several years and the development of quantum mechanics to correct this error. However, the theory does provide a very good explanation of both DC and AC electrical conductivity in metals.

2.2.1.2 Sommerfeld Theory of Metals

The most significant difference between the Drude and Sommerfeld Theory of Metals is that the Sommerfeld Theory assumes a Fermi-Dirac distribution of velocities over the aforementioned Maxwell-Boltzmann distribution assumption made by Drude. The application of Fermi-Dirac statistics to the electron gas comes as a consequence of the quantum nature of the

electron. Neglecting spin and taking the free and independent electron approximation, the wave-function of a single electron with energy ε satisfies the time independent Schrödinger equation:

$$-\frac{\hbar^2}{2m}\nabla^2\psi(\vec{r}) = \varepsilon \cdot \psi(\vec{r}) \tag{9}$$

subject to the boundary conditions:

$$\begin{aligned}\psi(x = L, y, z) &= \psi(x, y, z)\\ \psi(x, y = L, z) &= \psi(x, y, z)\\ \psi(x, y, z = L) &= \psi(x, y, z)\end{aligned} \tag{10}$$

where $L = V^{1/3}$ is the length of the enclosing volume to which the conduction electrons are bound by the attractive force of the ions. The solutions to this differential equation are plane waves of the form

$$\psi(\vec{r}) = \frac{1}{\sqrt{V}} e^{i\vec{k}\cdot\vec{r}} \tag{11}$$

with energies

$$\varepsilon(\vec{k}) = \frac{\hbar^2 k^2}{2m}, \tag{12}$$

where $\vec{k}$ is the wave-vector defined as

$$k_\mu = \frac{2\pi n_\mu}{L}, \qquad n_\mu \in integers \; and \; \mu = \{x, y, z\}. \tag{13}$$

Assuming that the metal region in question is very large and not too irregularly shaped, the total number of allowed points in k-space can be approximated as the volume of the k-space contained in that region (defined as Ω) divided by the volume of k-space per point, i.e. $(2\pi/L)^3$. Thus, the total number of allowed points in k-space is

$$\frac{\Omega}{\left({}^{2\pi}/_{L}\right)^{3}} = \frac{\Omega V}{8\pi^{3}} \tag{14}$$

and the density of states in k-space is therefore ${}^{V}/_{8\pi^{3}}$.

Assuming the electrons are non-interacting, an N-electron system can be created by simply placing an electron into each allowed one-electron level. Since the electrons are spin ½ particles, they obey the Pauli exclusion principle and only one electron (ignoring spin) is allowed to fill each energy level. For a large enough value of N, the k-space filled by the electrons can be approximated as a sphere with radius k_F, where k_F is the Fermi wave-vector, or the wave-number of the most excited state of the system. Multiplying the volume of the sphere by the density of states in k-space, it is possible to calculate the number, N, of allowed values of $\vec{k}$, ie

$$N = 2 \cdot \left({}^{4}/_{3}\,\pi k_F^3\right) \cdot \left(\frac{V}{8\pi^3}\right) = \frac{k_F^3}{3\pi^2} V, \tag{15}$$

where a factor of 2 is included to account for spin degeneracy. Thus, the electronic density is

$$n = \frac{N}{V} = \frac{k_F^3}{3\pi^2} \tag{16}$$

The Fermi momentum is related to the Fermi wave-vector as $p_F = \hbar k_F$ and the Fermi-velocity is therefore $v_F = \frac{\hbar}{m}(3\pi^2 n)^{1/3}$. For copper, this yields a Fermi velocity of 1.57x10^8 m/s. Using this velocity, the calculated mean free path length is $l = v_F \tau = 39\ nm$, much more than the 1-10Å calculated previously using the Drude model.

The Fermi-Dirac distribution for the electron gas describes the probability an electron has a certain energy. It is arrived at by careful consideration of energy level filling. The probability that, in an N-particle system, an electron has some energy E is given by

$$P_N(E) = \frac{e^{-E/k_BT}}{\sum e^{E_\alpha^N/k_BT}} \tag{17}$$

where E_α^N is the energy of the α^{th} stationary state for an N-electron system, with the summation taken over all stationary states.

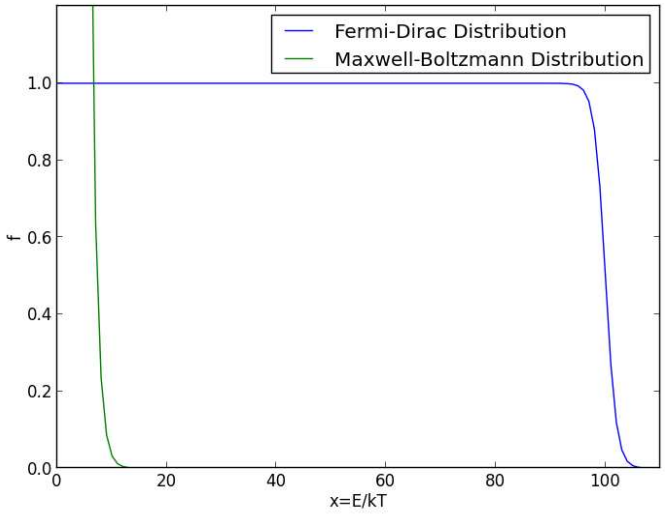

Figure 1: Maxwell-Boltzmann and Fermi-Dirac distribution at room temperature. Adapted from Ref [12] p31.

Since electrons are spin ½ particles, they obey the Pauli exclusion principles and fill N-energy bands with N-electrons. Following several manipulations that can be found in any text that includes Pauli-Dirac statistics, it is arrived at that the probability of an electron occupying an energy state ε is given by the *Fermi function*, defined as

$$f(\varepsilon) = \frac{1}{e^{(\varepsilon-\mu)/k_BT} + 1}, \tag{18}$$

where μ is the chemical potential, commonly referred to as the Fermi energy. Figure 1 shows a comparison of the Fermi function to the Maxwell-Boltzmann distribution.

While the Sommerfeld Theory does resolve the Drude Theory's underestimation of the mean free path length and overestimation of the conduction electron contribution to the specific heat at low temperature, it still suffers from many problems inherent to the free and independent electron approximation and infinitesimal scattering times [12]. Progress has been made on improving these models by relaxing these approximations and they're agreement with experiment has led to a greater ability to predict the properties of metal-semiconductor junctions.

2.3 Semiconductors

Semiconductors are materials that have a conductivity somewhere between that of a conductor and an insulator, hence the term *semi*conductor. While the research on semiconductors extends as far back as the 19th century, the development of the "Technology Age" in the 20th century has relied heavily on the tunable properties of semiconductors, resulting in a rapid expansion of work within the field.

The field of semiconductor research is both broad in topic and deep in complexity. What follows will be a presentation of introductory material, with emphasis placed on those topics germane to the research presented in this dissertation. Specifically, the following sections will discuss crystal structure, energy bands, carrier transport properties and optical properties.

2.4 Crystal Structure

The structure of a solid can be classified as crystalline, quasicrystalline or amorphous, depending on the system's long range order. In amorphous materials, there exists no long range order. An example of an amorphous material is a metallic glass, which is formed by the rapid cooling of a viscous liquid and contains no long range order, though local short range order may still be present. Solids that exhibit long range order are defined as crystals or quasicrystal.

Quasicrystals exhibit non-crystallographic rotational symmetries and lack periodicity in all or some dimensions. Crystals exhibit three-dimensional periodicity.

2.4.1.1 *Bravais Lattice and Basis*

The foundation of crystal structure analysis is based on the concept of the lattice and basis. The lattice that defines the periodic array of components in a crystal is defined as the *Bravais lattice.* In their book, Solid State Physics, Ashcroft and Mermin define the Bravais lattice in the following equivalent ways:

(a) A Bravais lattice is an infinite array of discrete points with an arrangement and orientation that appears *exactly* the same, from whichever of the points the array is viewed.

(b) A (three-dimensional) Bravais lattice consists of all point with position vectors **R** of the form

$$\mathbf{R} = n_1\mathbf{a}_1 + n_2\mathbf{a}_2 + n_3\mathbf{a}_3 \quad [12]$$

where the coefficients n_μ are integers and the vectors $\mathbf{a}_\mu$ are *primitive vectors* that span the lattice. The decoration of that Bravais lattice is called the basis. The basis can contain one or several atoms.

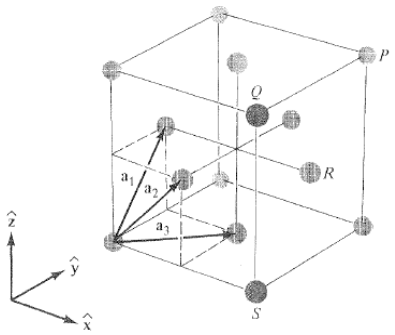

Figure 2: Face-centered Cubic Bravais lattice. Scanned from Ref. [12] p69.

The choice of primitive vectors for a given Bravais lattice is not unique; different combinations of Bravais lattices and bases can describe the same crystal structure. Typically, the preferred primitive vectors are those that are compact and symmetric, but any set of primitive

vectors that satisfies the above definition are acceptable. The face-centered cubic (FCC) Bravais lattice, shown in Figure 2, can be expressed using the following primitive vectors:

$$\mathbf{a}_1 = \frac{a}{2}(\hat{\boldsymbol{y}} + \hat{\boldsymbol{z}}) \qquad \mathbf{a}_2 = \frac{a}{2}(\hat{\boldsymbol{x}} + \hat{\boldsymbol{z}}) \qquad \mathbf{a}_3 = \frac{a}{2}(\hat{\boldsymbol{x}} + \hat{\boldsymbol{y}}), \tag{19}$$

where a is the crystal lattice spacing, typically 1-10 Å. The basis in this case contains only one atom placed on the Bravais lattice point.

The Bravais lattice defines the locations of the repeating elements of the crystal. The physical description of those repeating elements is defined as the *basis* of the crystal. In other words, at each position spanned by the Bravais lattice, there exists the same physical unit occupying that space in the same orientation and volume and that physical unit is the basis. The periodicity of the crystal lattice makes it possible to further characterize it by the number of nearest neighbors, i.e. the points in the Bravais lattice that are closest to a given point within the Bravais lattice.

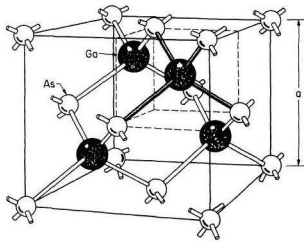

Figure 3: GaAs crystal structure. Scanned from Ref [16] p12

An example of a crystal structure that can be described using a multi-atom basis is the zincblende structure, shown in Figure 3, favored by GaAs. This structure can be described using a FCC Bravais Lattice ((19) together with a two atom basis $\{\mathbf{0}$ and $a/2\,(\hat{\boldsymbol{x}} + \hat{\boldsymbol{y}} + \hat{\boldsymbol{z}})\}$, with Ga assigned to one position and As assigned to the other position. If, on the other hand, both basis positions host the same element, the "diamond" lattice results.

2.4.1.2 *Reciprocal Lattice*

The periodic location of ions within a crystal naturally leads to a consideration of the electron momentum within the crystal. The reciprocal lattice of a crystal defines the crystal structure in momentum, or *k*-, space. The reciprocal lattice is defined as all wave vectors **K** that yield plane waves with the same periodicity as that of the Bravais lattice, ie

$$\boldsymbol{e^{iK\cdot R} = 1} \qquad \textbf{(20)}$$

As such, the reciprocal lattice describes the crystal structure in momentum or k-space. The reciprocal lattice is spanned by the primitive vectors a_1*, a_2* and a_3*. They are related to the Bravais lattice primitive vectors by $a_1{}^* = \frac{a_2 \times a_3}{a_1 \cdot (a_2 \times a_3)}$, $a_2{}^* = \frac{a_3 \times a_1}{a_2 \cdot (a_3 \times a_1)}$ and $a_3{}^* = \frac{a_1 \times a_2}{a_3 \cdot (a_1 \times a_2)}$.

Of particular interest is the *first Brillouin zone*. The first Brillouin zone has the unique feature that, for any vector **k**' not in the first Brillouin zone, it may be re-written as **k'**=**k** + **K**, where **K** is a reciprocal lattice vector and **k** lies in the first Brillouin zone. The first Brillouin zone is equal to the *Wigner-Seitz primitive cell* [12]. The Wigner-Seitz primitive cell is

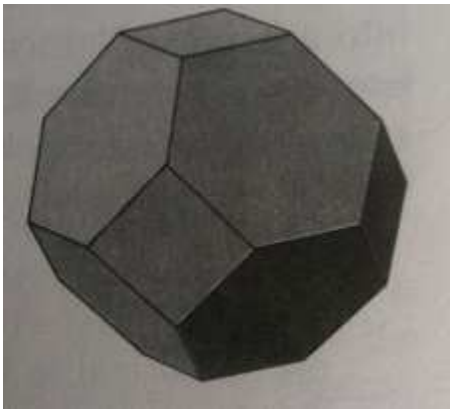

Figure 4: Wigner-Seitz cell for FCC lattice. Scanned from Ref. [12] p.89

constructed by choosing a lattice point in the Bravais lattice, then drawing lines to connect the chosen point to all other points within the lattice. Next, each line is bisected with a plane normal

to that line and the smallest polyhedron containing the point bounded by those planes is the Wigner-Seitz primitive cell. The first Brillouin zone, or Wigner-Seitz primitive cell, for a FCC Bravais lattice is shown in Figure 4.

In discussing a particular direction within a crystal, a common convention is to refer to the orientation using *Miller indices*. The notation is used extensively by crystallographers and represents a family of planes normal to the reciprocal lattice vectors h$\mathbf{a}_1$*+k$\mathbf{a}_2$*+l$\mathbf{a}_3$*. The planes are expressed using (hkl) notation. For expanded details, consult any introductory solid state or crystallography textbook.

2.5 Energy Bands

2.5.1.1 *Periodic Potentials*

A major consequence of the ion periodicity within a crystal is the development of energy bands and an energy gap. The development of energy bands can be understood in one dimension by extending the result found for a free electron to the case of an electron subject to diffraction off of a periodic lattice. For a free electron confined to a line of length L, the solution to the time-independent Schrödinger equation results in plane waves with energy

$$E = \frac{\hbar^2}{2m} k^2, \tag{21}$$

where *k* is the wave vector defined as $k = \frac{2\pi}{L} n$, where n is an integer.

If the free electron is then placed in a one-dimensional lattice of ions, with lattice constant *a*, Bragg diffraction will occur. The Bragg's condition is $m\lambda = 2a$ in one-dimension, which predicts that destructive interference of electron waves will occur whenever $= m \cdot {}^{\pi}/_{a}$. The diffraction at these momenta require the spatial solution to be a superposition of both a right

and left travelling wave, i.e. $k = \pm m\,{}^{\pi}/_{a}$. The two states created from the linear combinations are

$$\psi_1 = \frac{2i}{\sqrt{L}} \sin \frac{m\pi x}{L}$$
$$\psi_2 = \frac{2}{\sqrt{L}} \cos \frac{m\pi x}{L}. \quad \textbf{(22)}$$

The probability an electron is at any given location is given by $|\psi_i|^2$. The peaks in $|\psi_i|^2$ for the two solutions show that, for ψ_1, the probability peaks between the ions while, for ψ_2, the probability peaks over the ions (Figure 5).

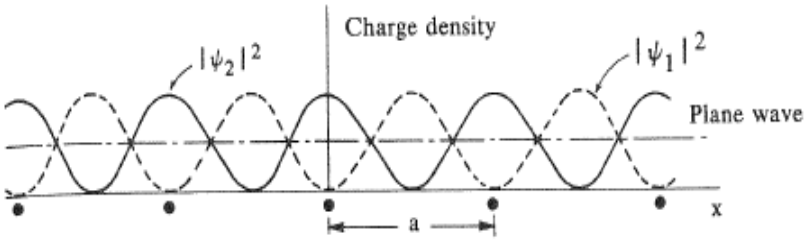

Figure 5: Spatial dependence of charge density as described in text. Scanned from Ref. [17] p245.

If we approximate the potential energy due to the ion lattice as $V(x) = V_0\cos(2\pi x/a)$, the band gap can be calculated using first-order perturbation theory as follows

$$E_g = <\psi_2|V(x)|\psi_2> - <\psi_1|V(x)|\psi_1> \quad \textbf{(23)}$$

The first order result is a predicted bandgap of $E_g = V_0$ at $k = \pm m\pi/a$, shown on Figure 6. This simple example shows that the periodic potential of a crystal generates a periodic bandgap within the electronic dispersion relation, creating forbidden energy regions due to Bragg destructive interference.

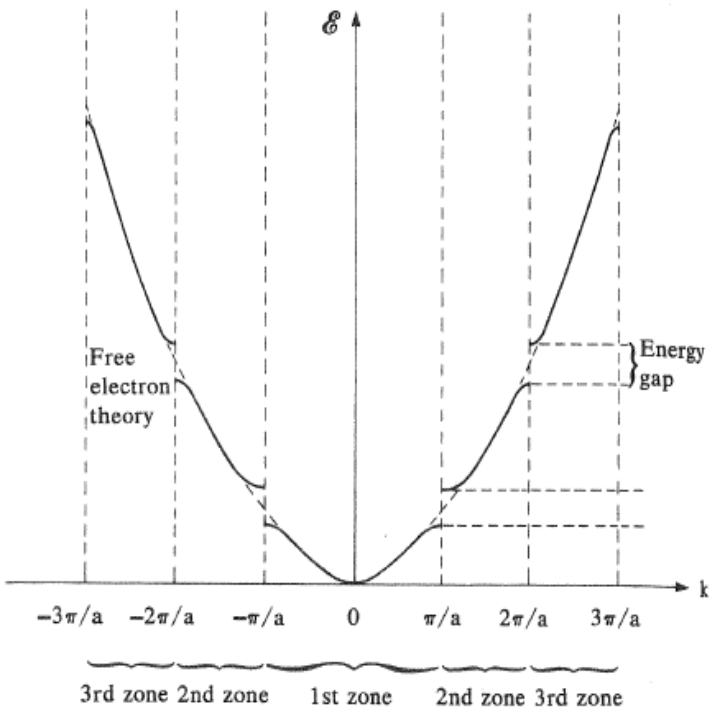

Figure 6: Energy vs. wave vector for free elecrons (dashed parabola) and for almost free electrons as described in text. Scanned from Ref. [17] p244.

The ions located within a three-dimensional crystal structure generate a periodic potential that mirrors their periodicity described by their Bravais lattice and basis. The periodicity of the potential has the property

$$\boldsymbol{U}(\boldsymbol{r}+\boldsymbol{R}) = \boldsymbol{U}(\boldsymbol{r}), \tag{24}$$

for all **R** bravais lattice vectors.

The time-independent Schrödinger equation with a potential is

$$-\frac{\hbar^2}{2m}\nabla^2\psi(\boldsymbol{r}) + U(\boldsymbol{r})\psi(\boldsymbol{r}) = E\psi(\boldsymbol{r}). \tag{25}$$

If the electrons within the crystal are treated as non-interacting (ie the independent electron approximation) they are referred to as *Bloch electrons* and Eq. (25) is valid for all electrons in the

crystal. As a consequence of the periodicity of the potential, the Bloch electron's eigenstate solutions have the following property:

$$\psi_k(\boldsymbol{r}) = e^{i\boldsymbol{k}\cdot\boldsymbol{r}} u_k(\boldsymbol{r}) \tag{26}$$

where

$$u_k(\boldsymbol{r} + \boldsymbol{R}) = u_k(\boldsymbol{r}). \tag{27}$$

For clarity, it should be noted that the wave-vector ***k*** is not proportional to the momentum of the electron like the case of a free electron where **p**=ħ**k**. In this case, ***k*** refers to the *crystal momentum* of the electron and is related to the translational symmetry of a periodic potential. Eq. (26) is *Bloch's Theorem*, which defines the *Bloch function* as the product of a *plane wave factor* and a *periodic function factor* with the property shown in Eq. (27). As a result of Bloch's Theorem, $\psi_K(\mathbf{r}+\mathbf{R}) = \psi_K(\mathbf{r})$.

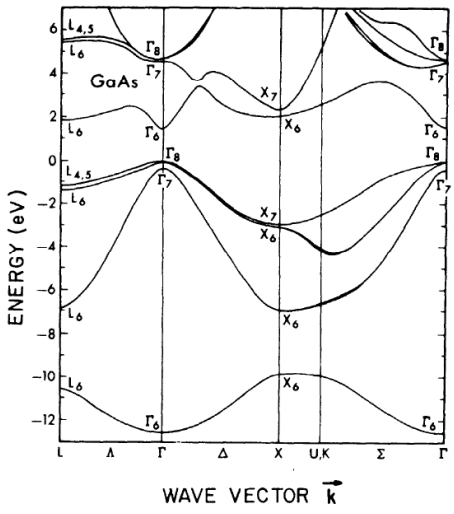

Figure 7: Band structure of GaAs. Figure from Ref [18]

Analogous to the previously discussed one-dimensional lattice of ions example, the periodicity of the Bravais lattice potential results in periodic energy bands and band gaps. The energy vs crystal momentum curve is continuous within a given Brillouin zone but experiences a discontinuity at the Brillouin zone boundaries forming a band gap and creating energy bands. The full set of energy levels can be described with **k** restricted to the cell formed using only the primitive basis. However, it can be useful to allow **k** to span all of *k*-space. This leads to several degenerate energy levels, but also creates a family of continuous function $\varepsilon_n(\mathbf{k})$.

Since **k'**=**k** + **K,** where **k** and **k'** are vectors differing by a reciprocal lattice vector, the indexed eigenstates and eigenvalues are periodic functions of **k** in the reciprocal lattice such that $\psi_{n,\mathbf{k}+\mathbf{K}}(\mathbf{r}) = \psi_{n,\mathbf{k}}(\mathbf{r})$ and $\varepsilon_{n,\mathbf{k}+\mathbf{K}} = \varepsilon_{n,\mathbf{k}}$. These functions form a family of continuous functions, each with the same periodicity as the reciprocal lattice and are referred to as the *band structure* of the solid. The band diagram for GaAs is shown in Figure 7.

2.5.1.2 *Calculating Band Structure*

The band structure of a crystal can be measured directly, using such methods as angle-resolved photoemission spectroscopy (ARPS). An active region of research in Condensed Matter physics is developing theoretical models that agree with the measured band structures of crystals. There are many advantages to developing accurate theoretical models capable of predicting the band structure of crystals, from increasing our understanding of electron interactions within a crystal to designing novel materials with advantageous electronic band structures.

The full Schrödinger equation for an ideal crystal with *n* electrons and *N* ions is

$$\left[-\sum_{i=1}^{n}\frac{\hbar^2}{2m}\nabla_i^2-\sum_{k=1}^{N}\frac{\hbar^2}{2M_k}\nabla_k^2+\frac{1}{2}\sum_{i,j=1}^{n}\frac{e^2}{r_{ij}}+V_{ij}(\boldsymbol{R_1},\dots,\boldsymbol{R_N})+V_{ei}(\boldsymbol{r_1},\dots,\boldsymbol{r_n},\boldsymbol{R_1},\dots,\boldsymbol{R_N})\right]\psi = E\psi, \quad \textbf{(28)}$$

where $\mathbf{r}_i$ represents the electronic coordinates and $\mathbf{R}_i$ represents the ionic coordinates. The first and second term are the electronic and ionic kinetic energies, respectively. The third term is the electron-electron Coulombic interaction, the fourth term is the ion-ion Coulombic interaction and the final term the electron-ion interaction. The adiabatic approximation, proposed by Born and Oppenheimer in 1927, states that the electronic distribution adjusts to the ionic position at a high rate compared to ion motion and therefore, in the electronic frame, the ions can be assumed to be at rest. Under this approximation, the Schrödinger equation for the electronic eigenfunction simplifies to

$$\left[-\sum_{i=1}^{n}\frac{\hbar^2}{2m}\nabla_i^2+\frac{1}{2}\sum_{i,j=1}^{n}\frac{e^2}{r_{ij}}+V_{ei}(\boldsymbol{r_1},\dots,\boldsymbol{r_n},\boldsymbol{R_1},\dots,\boldsymbol{R_N})\right]\psi = E\psi, \quad \textbf{(29)}$$

The presence of the electron-electron interaction makes an analytical solution extremely challenging. However, some methods have been developed to achieve approximate solution.

The Hartree-Fock method expresses the N-electron eigenfunction is expressed as the Slater determinant of one-electron functions, ie

$$\psi_N(r_1 s_1,\dots,r_N s_N)=\frac{1}{\sqrt{N}}\begin{vmatrix}\varphi_1(\boldsymbol{r}_1)\alpha_1(s_1) & \dots & \varphi_N(\boldsymbol{r}_1)\alpha_N(s_1)\\ \vdots & \ddots & \vdots\\ \varphi_1(\boldsymbol{r}_{N1})\alpha_1(s_N) & \cdots & \varphi_N(\boldsymbol{r}_N)\alpha_N(s_N)\end{vmatrix} \quad \textbf{(30)}$$

where φ and α represent the one-electron spatial and spin eigenfunction, respectively. The spatial eigenfunctions are determined using the variational approach, i.e. minimizing the

expectation value of the Hamiltonian. This approach leads to an exchange term that can sometimes lead to erroneous physical results [12].

There are many other methods for calculating band structure, such as density functional theory (DFT), where the electron-electron potential can be modelled as spatially dependent electron density functionals. Accurately calculating the energy bands for semiconductors is a very active topic of research, with advances published regularly.

2.6 Carrier Transport Properties

The electrical character of a semiconductor depends on its charge carrier transport properties, specifically the carrier concentrations. The charges within a semiconductor are Fermi particles and therefore follow a Fermi-Dirac distribution with respect to the occupation number of a state with energy $E_{\mathbf{k}}$ in thermal equilibrium at temperature T. Of particular interest are the charges within the conduction band. These charges can be generated in the following ways: thermal or optical excitations of electrons from the valence band to the conduction band, excitations from impurity states within the material, or injected from an outside source.

Semiconductors are classified into two categories based on the primary source of their current carriers: intrinsic and extrinsic. An intrinsic semiconductor is either a 'pure' semiconductor, i.e. with no impurities, or a semiconductor with impurities that is operated at such a high temperature that the primary charge carriers are those thermally generated from the intrinsic semiconductor material and not the impurities. In contrast, an extrinsic semiconductor is a semiconductor that has doped impurities as its primary source of current carriers. It is termed extrinsic since its electrical properties arise from the non-intrinsic properties of the bulk semiconductor.

2.6.1.1 *Intrinsic semiconductors*

The Fermi-Dirac (FD) distribution specifies the occupation number of an electron within the semiconductor band with a band energy E_k at thermal equilibrium with a given temperature T. At T = 0K, i.e. absolute zero, the FD distribution is a step function, with $f_{FD}(E_{\boldsymbol{k}} < E_f) = 1$

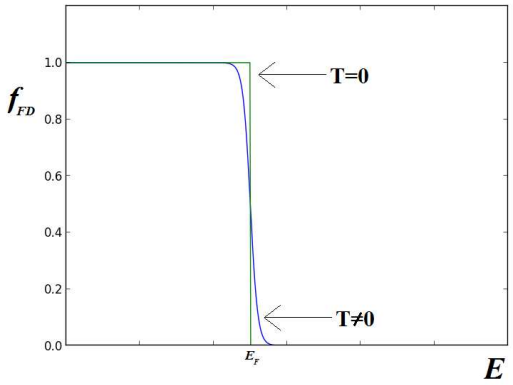

Figure 8: Fermi-Dirac distribution at nonzero temperature

and $f_{FD}(E_{\boldsymbol{k}} > E_f) = 0$. As the temperature is increased, thermal excitation promotes electrons into the conduction band and the FD distribution extends into energies greater than E_F, as shown in Figure 8.

The concentration of electrons in the conduction band at finite temperature can be calculated by making the following approximations. First, assuming that the energy difference between the conduction band and Fermi energy is much greater than the thermal energy, $(E_{c\boldsymbol{k}} - E_f) \gg k_B T$, the denominator of the FD distribution can be approximated as $e^{\beta(E_{c\boldsymbol{k}} - E_f)} + 1 \approx e^{\beta(E_{c\boldsymbol{k}} - E_f)}$, where $\beta = {}^{1}/_{k_B T}$. This approximation reduces the FD distribution to a Maxwell-Boltzmann distribution of the form

$$f_{FD}(E_{c\boldsymbol{k}}) \approx e^{-\beta(E_{c\boldsymbol{k}} - E_f)} \quad \textbf{(31)}$$

Next, the conduction band can be approximated as parabolic and therefore expressed as

$$E_{c\boldsymbol{k}} = E_c + \frac{\hbar^2 k^2}{2m_c^*}, \tag{32}$$

where E_c is the conduction band edge and m_c^* the effective mass of the electron in the conduction band. The effective mass term distinguishes the crystal momentum relationship seen here from the free-space electron.

The concentration of electrons in the conduction band is

$$n = \frac{2}{\Omega}\sum_{\boldsymbol{k}} f_{FD}(E_{c\boldsymbol{k}}), \tag{33}$$

where Ω is the volume of the system. The factor of two has been added to account for the spin-degeneracy. This summation can be converted to an integral as

$$\sum_{\boldsymbol{k}} \rightarrow \frac{\Omega}{(2\pi)^3}\int d^3k, \tag{34}$$

resulting in

$$n = \frac{1}{4\pi^3}\int d^3k \frac{1}{e^{\beta(E_{c\boldsymbol{k}}-E_f)}+1} \approx \frac{1}{4\pi^3}\int d^3k\, e^{-\beta\left(E_c+\frac{\hbar^2k^2}{2m_c^*}-E_f\right)}, \tag{35}$$

where the approximations of Eqs. (31)and (32) have been applied. Converting the integral from Cartesian to spherical coordinates and integrating over the solid angle, Eq. (35) reduces to

$$n = e^{-\beta(E_c-E_f)}\int N_c(E)e^{-\beta E}dE, \tag{36}$$

where $E = \frac{\hbar^2 k^2}{2m_c^*}$. $N_c(E) = \frac{1}{2\pi^2}\left(\frac{2m_c^*}{\hbar^2}\right)^{3/2} E^{1/2}$ is the density-of-states in energy for the conduction band. The integral in Eq. (36) is proportional to the Gamma Function, i.e. $\Gamma\left(\frac{3}{2}\right) = \sqrt{\pi}/2$. Thus,

$$n = \bar{N}_c e^{-\beta(E_c - E_f)} \tag{37}$$

where $\bar{N}_c = 2\left(\frac{m_c^* k_B T}{2\pi\hbar^2}\right)^{3/2}$ is the effective density-of-states for the conduction band.

The promotion of a valence electron to the conduction band leaves behind a hole in the valence band of an atom. This absence of a negative charge is equivalent to the presence of a positively charged quasi-particle defined as an *electron hole* or *hole*. The holes contribute to the net charge carrier concentration when modelling current flow and must therefore be considered when discussing charge densities. The energy band of the hole can also be modelled as parabolic, with

$$E_{v\boldsymbol{k}} = E_v - \frac{\hbar^2 k^2}{2m_v^*}, \tag{38}$$

where E_v represents the edge of the valence band and m_v* the effective mass of the hole. Following the same approximations as before, the hole concentration is

$$p = \bar{N}_v e^{-\beta(E_f - E_v)}, \tag{39}$$

where $\bar{N}_v = 2\left(\frac{m_v^* k_B T}{2\pi\hbar^2}\right)^{3/2}$ is the effective density-of-states.

Since holes are created every time a valence electron is promoted to the conduction band, the hole concentration must be equal to that of the conduction electron concentration in an intrinsic semiconductor. To determine an expression independent of the Fermi energy, the product of the two concentrations is

$$np = \bar{N}_c \bar{N}_v e^{-\beta E_g} = n_i^2, \tag{40}$$

where E_g is the bandgap energy and n_i the intrinsic charge carrier concentration. Eq. (40) is the *Law of Mass Action*. Using this expression, it is possible to determine the intrinsic charge carrier concentration of a material given the energy band's effective masses and the band gap energy.

The effective electron and hole mass for intrinsic GaAs is $0.066m_e$ and $0.5m_e$, respectively, and GaAs has a bandgap of 1.42 eV at room temperature (300K) [13]. Therefore, the intrinsic carrier concentration at room temperature is

$$n_i = \sqrt{\bar{N}_c \bar{N}_v} e^{-\beta E_g/2} = 2\left(\frac{k_B T}{2\pi\hbar^2}\right)^{3/2} (m_v^* m_c^*)^{3/4} e^{-\beta E_g/2} = 2.1 \times 10^6 \text{cm}^{-3} \tag{41}$$

Using this this result, it is possible to calculate the resistivity, ρ, of intrinsic GaAs at room temperature. Using the electron and hole mobilities of $\mu_e \approx 8500\ {}^{\text{cm}^2}/_{\text{Vs}}$ and $\mu_h \approx 400\ {}^{\text{cm}^2}/_{\text{Vs}}$ [13], respectively, $\rho = [en_i(\mu_e + \mu_h)]^{-1} = 3.34 \times 10^8\ \Omega$ cm. Pure GaAs is hard to achieve experimentally and epitaxial growth of GaAs typically introduces donor impurities that increase the current carrier concentration, leading to a measured resistivity $\sim 10^7\ \Omega$ cm. Epitaxial grown GaAs is therefore referred to as "semi-insulating."

The equality of electron and hole concentrations can be used to determine the Fermi energy. Since $n = p$, $\bar{N}_c e^{-\beta(E_c - E_f)} = \bar{N}_v e^{-\beta(E_f - E_v)}$. Solving for E_f,

$$E_{fi} = E_v + \frac{1}{2}E_g + \frac{3}{4}k_B T \log\left(\frac{m_v^*}{m_c^*}\right) \quad \textbf{(42)}$$

where the Fermi energy contains a subscript 'i' to mark it as the intrinsic Fermi energy and E_g is the band gap energy. At 0K, the Fermi energy lies in the middle of the band gap, while the increasing temperature moves the Fermi energy upwards towards the conduction band.

2.6.1.2 *Extrinsic semiconductors*

Impurities can be added to a semiconductor structure to increase the concentration of electrons and holes in the material. A schematic of this doping is shown in Figure 9, where an impurity ion of arsenic is added to a germanium crystal lattice. The doping ion is substituted into the crystal, replacing an ion in the lattice. If the doping element has a greater number of valence electrons than the intrinsic element it is substituting, it increases the electron concentration in the conduction band and is considered a *donor* ion. The resulting semiconductor is donor doped, or n-type. In contrast, an *acceptor* ion is a doping element that has less valence electrons than the substituted intrinsic element. The resulting semiconductor is acceptor-doped, or p-type. Arsenic has 2 valence electrons, while germanium has 3. The addition of the arsenic ion into the germanium lattice increases the hole density in the valence band and the material is therefore p-type.

The donor and acceptor density, N_D and N_A respectively, typically have sufficiently small

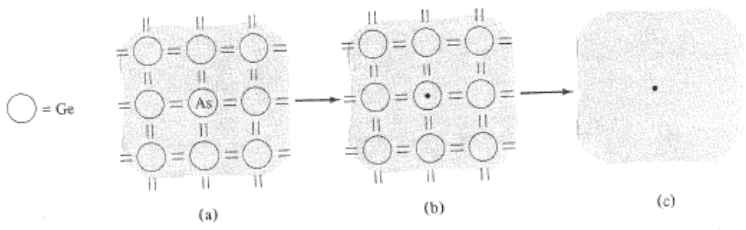

Figure 9: Schematic of doping a semiconductor. (a) substituting arsenic (valence 5) impurity for germanium (valence 4) in crystal lattice. (b) the arsenic impurity represented as a germanium atom plus an additinoal unit of positive charge. (c) arsenic impurity treated as positive charge in homogeneous medium. Scanned from Ref [12] p577.

binding energies such that at room temperature, they are fully ionized. The electric neutrality equation then becomes

$$p - n + N_A - N_D = 0 \quad \textbf{(43)}$$

For silicon-doped GaAs with N_D = 4 x 10^{17} and N_A = 0, combining the law of mass action with the electric neutrality equations yields a relationship between the carrier concentration and intrinsic density of $n = \frac{N_D}{2} + \left(n_i^2 + \left(\frac{N_D}{2}\right)^2\right)^{1/2}$. Earlier it was shown that the intrinsic carrier concentration was ~10^6 cm^{-3} at room temperature for GaAs. Thus, for the silicon-doped GaAs, $N_D >> n_i$ and the carrier concentration is approximately equal to the donor density, i.e. $n = N_D$. The hole density is $p=n_i^2/N_D$; for the doped GaAs, this predicts a hole concentration ~10^{-5} cm^{-3} and is therefore negligible.

Doping of a semiconductor modifies the Fermi energy. For an n-type semiconductor, the Fermi energy increases with increasing doping concentration. This is observed by taking the equation for the charge carrier concentration, $n = \bar{N}_c e^{-\beta(E_c - E_f)} \cong N_D$, and solving for E_f:

$$E_F = E_c + k_B T ln\left(N_D / \bar{N}_c\right) \quad \textbf{(44)}$$

2.7 Optical Properties

2.7.1.1 *Interband Absorption*

Semiconductors absorb light by undergoing transitions between allowed energy levels. These allowed energy levels are described by the energy bands discussed earlier. When a photon with energy greater than or equal to the band gap is absorbed, a valence electron is promoted to the conduction band, creating an electron-hole pair and increasing the charge density of the

material. If the energy of the conduction band is defined as E_2 and the energy of the valence band is defined as E_1, then by the Conservation of Energy, E_2-E_1 = hν, where hν is the photon energy.

The Conservation of Momentum requires that p_2-p_1=hν/c=h/λ or equivalently, k_2-k_1=2π/a, where the subscripts represent the conduction and valence bands previously defined. The photon momentum is negligibly small when compared to the momentas spanned by charge carriers, i.e. $\frac{h}{\lambda} \ll \frac{2\pi}{a}$. Accordingly, the momentum of the hole and electron, or the valence and conduction band, following photon absorption must be approximately equal, i.e. $k_2 \approx k_1$. These types of transitions are represented by vertical lines in the E-k band diagram.

The probability that a semiconductor will absorb a photon is based on the occupation probability, the transition probability and the optical joint density of states. The occupation probability for absorption is the probability that the conduction band state E_2 is empty and that the valence band state E_1 is filled prior to light exposure, calculated as

$$P_A(\nu) = [1 - f_c(E_2)] \cdot f_v(E_1). \quad \textbf{(45)}$$

The transition probability is arrived at through application of quantum mechanics, while the optical joint density of states relates the density of states with which a photon of a given energy interacts with. The result of this analysis is that the theoretical absorption coefficient in thermal equilibrium is given as approximately

$$\alpha(\nu) \approx \frac{\sqrt{2}c^2 m_r^{3/2}}{\tau_r} \frac{1}{(h\nu)^2} \sqrt{h\nu - E_g}, \quad \textbf{(46)}$$

where τ_R is the radiative electron-hole recombination lifetime and m_r the reduced mass of the hole and conduction electron [19]. The predicted absorption pattern is plotted in Figure 10 along with the experimental absorption pattern of various semiconductors in Figure 11.

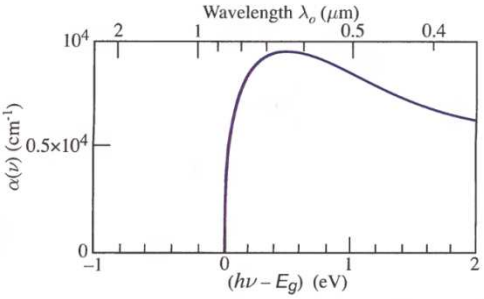

Figure 10: Absorption coefficient as predicted by Eq. (48). Scanned from Ref. [19] p662.

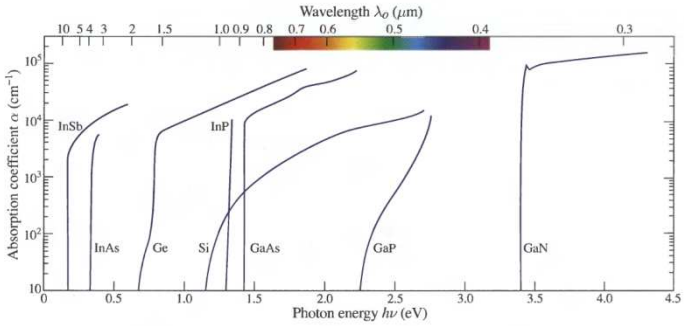

Figure 11: Measured absorption coefficients for various semiconductors. Scanned from Ref. [19] p662.

The absorption coefficient can be used to predict the absorption of light as it travels through the semiconductor. From Beer-Lambert's law, the intensity of light decreases as

$$\mathrm{I}(x) = \mathrm{I}_0 e^{-\alpha x}, \tag{47}$$

where I_0 is the incident intensity, α the absorption coefficient and x the distance the beam has travelled through the semiconductor. The absorption coefficient of intrinsic GaAs at 632.8 nm is 3.90 μm^{-1} [20]. Therefore, the ratio of absorbed light intensity after travelling 200 nm into the material is $(1\text{-}\mathrm{I}(x{=}200\mathrm{nm}))/\mathrm{I}_0 \times 100\% = 54.2\%$. If the incident intensity is 0.018 W/cm^2, this predicts an absorption of 9.7 mW/cm^2 after travelling 200nm. Assuming each photon absorption generates an electron-hole pair, this would result in a bound electron-hole pair density generation rate of 3.10 x 10^{16} electron-hole pairs/cm^2-sec.

2.7.1.2 *Radiative Recombination*

The free charge carriers generated following the absorption of a photon generally have a short lifetime and can recombine. As a result of the conservation of energy discussed earlier, this

recombination results in the generation of either a photon (radiative) or phonon (non-radiative). This time dependence is governed by the rate equation

$$\frac{d\Delta n}{dt} = -\frac{\Delta n}{\tau}, \tag{48}$$

where Δn is the photogenerated charge density and τ the carrier lifetime. The solution of this differential equation shows that the photogenerated carrier concentration decreases exponentially in time as

$$\Delta n(t) = \Delta n(0) e^{-t/\tau}, \tag{49}$$

where $\Delta n(0)$ is the initial photogenerated carrier concentration. If the recombination rate is defined as

$$R = -\frac{d\Delta n}{dt} = \frac{\Delta n}{\tau}, \tag{50}$$

then the total recombination rate is

$$R_T = R_r + R_{nr}, \tag{51}$$

where R_r and R_{nr} are the radiative and non-radiative recombination rates. The internal quantum efficiency is defined as the ratio of the radiative recombination rate to the total recombination rate, ie

$$\eta_i = \frac{R_r}{R_r + R_{nr}}. \tag{52}$$

The lifetime of free charge carriers is related to their concentration. The spontaneous recombination rate is equal to

$$R_{sr} = B_r np, \tag{53}$$

where B_r is a characteristic material parameter. The electron and hole charge densities can be expressed as $n = n_0 + \Delta n$ and $p = p_0 + \Delta p$, where the first term represents the intrinsic charge density and the second represents the excess free charge concentrations generated via photon absorption. Since the excess free charge is photogenerated, $\Delta n = \Delta p$. Thus

$$R_{sr} = B_r[\Delta n^2 + \Delta n(n_0 + p_0) + n_0 p_0], \tag{54}$$

The recombination rate at thermal equilibrium is ${R_{sr}}^{eq} = B_r n_0 p_0$ and therefore the excess charge recombination rate is $R_{sr} - {R_{sr}}^{eq}$. This, combined with Eq (50), yields an expression for the radiative recombination lifetime of the excess charge carriers of

$$\tau_R = \frac{1}{B_r[\Delta n + n_0 + p_0]} \tag{55}$$

This relationship creates two limits for the radiative lifetime. For $\Delta n \gg n_0 + p_0$, $\tau_R \sim {}^{1}/_{\Delta n}$ whereas for $\Delta n \ll n_0 + p_0$, $\tau_R \sim {}^{1}/_{(n_0 + p_0)}$. These two limits are shown in Figure 12.

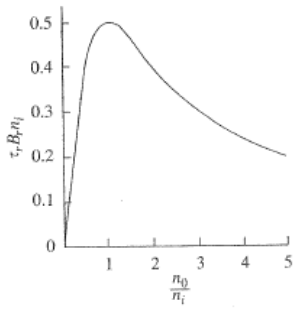

Figure 12: Recombination lifetime recombination lifetime of excess charge carriers predicted by (46). Scanned from Ref. [19] p259.

2.7.1.3 *P-N Junctions*

A p-n junction is a simple semiconductor device with a broad range of applications, including photovoltaics, light emitting diodes (LEDs) and use as a rectifying junction. The term p-n junction refers to the interface between two regions of semiconductors, one of which is p-type and the other which is n-type. The standard fabrication of a pn junction is accomplished by doping a single slab of semiconductor, with one section of the slab doped with donor impurities and the remaining section doped with acceptor impurities. A single intrinsic material is used to prevent lattice defects at the p and n-type junction. The real boundary between the two slabs has continuous charge density. However, for ease of analysis, the junction will be modelled as an abrupt change.

Consider a 2D system, initially separated, that consists of a p-type material with doping density N_A and n-type material with doping density N_D, that have weak enough bonds that they are all ionized at room temperature. From the previous discussion of extrinsic semiconductors, it is clear that the two materials will have different Fermi energies due to their differing charge densities. When the two slabs are brought into contact with one another, charges will diffuse from one material into the other, with electrons diffusing into the p-type material and holes diffusing into the n-type material, leaving behind oppositely charged, stationary ions near the

interface. The build-up of ions results in an electric field, **,** of increasing strength until an equilibrium is achieved between the current density generated by the electric field and the diffusion current density, ie

$$J_e = en\mu_e + \mathrm{e}D_e\nabla n = 0$$
$$J_h = en\mu_h - \mathrm{e}D_h\nabla p = 0 \qquad \textbf{(56)}$$

where D_e and D_h are the diffusion coefficients for the electrons and holes and μ_e and μ_h the electron and hole mobilities. The region of depleted space charge and electric field generating ions is called the depletion region.

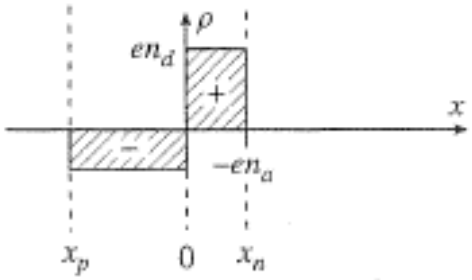

Figure 13: Charge distribution and geometry of PN junction. Scanned from Ref. [21] p313.

The *depletion approximation* assumes that, in their respective depletion regions, all of the dopants are fully ionized while outside the depletion region, the material maintains electrical neutrality. This leads to a space charge density of

$$\rho(x) = 0 \qquad for\ x \le x_p\ and\ x \ge x_n$$
$$\rho(x) = -eN_A \qquad for\ x_p \le x \le 0 \qquad \textbf{(57)}$$
$$\rho(x) = eN_D \qquad for\ 0 \le x \le x_n$$

with the geometry of the space charge region shown in Figure 13.

The charge in the depletion region generates a built-in electric field in the junction region. The electric field, by definition, is the negative gradient of an electrostatic potential, V(x). The potential generated at such a junction is often termed the *contact potential* or *diffusion potential*. To determine the magnitude of the potential, two approaches are possible, each yielding an equivalent result: either enforcing the equilibrium condition that the Fermi level is continuous throughout the material or the zero charge flux condition stated in Eq. (56). The former is presented here.

The equilibrium condition that the Fermi level is constant throughout the material can be related to the contact potential through the charge densities. The initial concentration of the *p* and *n* type region are $p = \bar{N}_v e^{-\beta(E_f - E_v)} \approx N_A$ and $n = \bar{N}_c e^{-\beta(E_c - E_f)} \approx N_D$. Solving each equation for the Fermi energy and setting the two equations equal results in

$$E_v - E_c = k_B T \ln\left(\frac{N_D N_A}{n_i^2}\right) \tag{58}$$

The valence and conduction band energies are related to the potentials V_n and V_p as $E_v = -eV_v$ and $E_c = -eV_c$. Thus, the diffusion potential is given as

$$V_d = V_n - V_p = \frac{k_B T}{e} \ln\left(\frac{N_D N_A}{n_i^2}\right) \tag{59}$$

The built in electric field, **,** can be calculated using Gauss' Law in one dimension, ie

$$\frac{d}{dx} = \frac{\rho(x)}{\varepsilon} \tag{60}$$

Since the electric field is zero outside of the space charge region, charge neutrality requires that $N_D x_n = N_A x_p$. On the left hand side of the junction,

$$\frac{d}{dx} = \frac{-eN_A}{\varepsilon} \tag{61}$$

Direct integration yields $(x) = \frac{-eN_A}{\varepsilon} x + C$. The constant C is found by the boundary condition

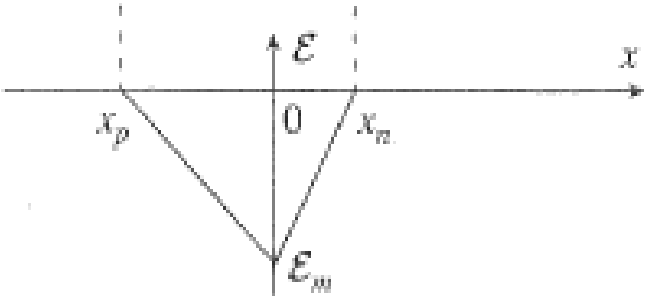

Figure 14: Electric field in PN junction. Scanned from Ref. [21] 314.

that $(x = x_p) = 0 \rightarrow C = \frac{eN_A}{\varepsilon} x_p$. The electric field on the right hand side can be found using similar calculations to yield

$$\begin{aligned} (x) &= -\frac{eN_A(x - x_p)}{\varepsilon} && for\ x_p \le x \le 0 \\ (x) &= \frac{eN_D(x - x_n)}{\varepsilon} && for\ 0 \le x \le x_n \end{aligned} \tag{62}$$

The electric field is plotted in Figure 14.

The built in electric field modifies the local energy bands within the depletion region. The electric potential can be calculated from Eq. (62) using

$$\frac{dV}{dx} = -(x). \tag{63}$$

Direct integration and application of the boundary conditions that $V(x=x_p)=V_p$ and $V(x=x_n)=V_n$ yields

$$V(x) = \frac{eN_A(x-x_p)^2}{2\varepsilon} + V_p \qquad for\ x_p \le x \le 0$$
$$V(x) = -\frac{eN_D(x-x_n)^2}{2\varepsilon} + V_n \qquad for\ 0 \le x \le x_n \tag{64}$$

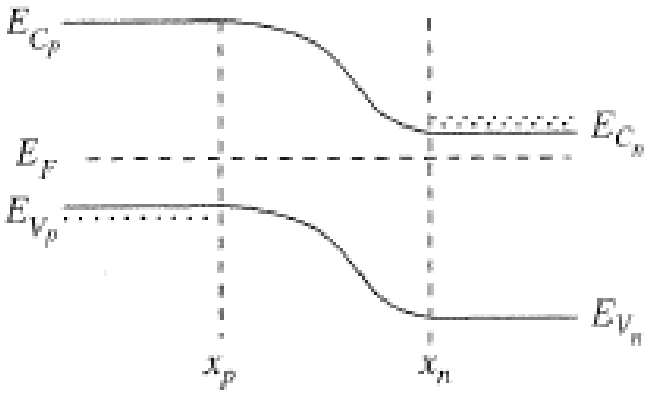

Figure 15: PN conduction and valence band edges. Scanned from Ref. [21] p315

Setting the valence band edge to zero in the p-type regime, the valence band value throughout space is

$$E_v(x) = -eV(x) \tag{65}$$

Since the band gap, E_g, is constant throughout the material, the conduction band energy can be defined as

$$E_c(x) = E_g - eV(x) \tag{66}$$

A plot of the conduction and valence band edges are shown in Figure 15.

A final consideration is the width of the space charge region. Setting the two expressions for voltage equal in Eq.(64) at the junction x=0,

$$\frac{eN_A{x_p}^2}{2\varepsilon} + V_p = -\frac{eN_D{x_n}^2}{2\varepsilon} + V_n. \quad \textbf{(67)}$$

Recalling that the diffusion potential is given as $V_d=V_n-V_p$,

$$V_d = \frac{eN_A{x_p}^2}{2\varepsilon}\left(1+\frac{N_A}{N_D}\right) = \frac{eN_D{x_n}^2}{2\varepsilon}\left(1+\frac{N_D}{N_A}\right). \quad \textbf{(68)}$$

Solving for x_p and x_n separately, the width of the space charge region is

$$W = x_p + x_n = \sqrt{\frac{2\varepsilon k_B T}{e^2}\left(\frac{n_a+n_d}{n_a n_d}\right)\log\left(\frac{n_a n_d}{n_i^2}\right)} \quad \textbf{(69)}$$

This width can be modulated by the application of an external bias. However, the energy band and barrier width response to applied voltage, as well as the current-voltage characteristics requires additional analysis, beyond the scope of this work.

3 Metal-Semiconductor Hybrid (MSH) Devices

Metal-semiconductor hybrid (MSH) devices have junctions between a semiconductor and a metal that make them useful for a wide range of applications. This section will introduce Schottky and Ohmic junctions, discuss junction field effect transistors (JFET) and metal-semiconductor field effect transistors (MESFET), and give a comprehensive overview of extraordinary phenomenon devices termed EXX devices.

3.1 Metal-Semiconductor Junctions

Metal-Semiconductor junctions can be divided into two categories: rectifying and non-rectifying. Rectifying contacts have an asymmetric current-voltage (IV) relationship, allowing a high flow of current under a forward bias but restricting current flow under reverse bias. In contrast, a non-rectifying, or Ohmic, contact has a linear IV relationship that has inversion symmetry under forward and reverse bias.

3.2 Schottky

A Schottky contact is a rectifying contact. It is characterized by a barrier that forms at the junction between a metal and semiconductor. When a semiconductor is brought into contact with a metal to form a Schottky contact, charge will flow from the semiconductor into the metal until the Fermi levels in both materials are equal. This is the same thermal equilibrium condition enforced in the previously discussed PN junction.

Since the charge density of a metal is much greater than that of a semiconductor, the Fermi energy of the metal does not change when the materials are brought into contact and the excess charge resides on the surface of the metal at the contact plane. Therefore, the semiconductor's Fermi level is reduced to match that of the metal. Figure 16 shows the work function for a metal and semiconductor, where the work function is defined as the energy

difference between the Fermi energy and vacuum. The work function for a metal is $W_m = q\Phi_m$and the semiconductor work function is $W_s = q\Phi_S = q(\chi_s + V_n)$, where Φ_m and Φ_S are the electrostatic potentials between the Fermi level and vacuum of the metal and semiconductor, respectively, and χ_s is the semiconductor electron affinity, defined as the energy difference between the bottom of the conduction band and vacuum, and $V_n = E_c - E_F$ in the semiconductor (see Figure 16). Thus, the Fermi level in the semiconductor is reduced by $V_c = q\Phi_m - q(\chi_S + V_n)$, where V_c is the contact potential. From Figure 16, the limiting value of the barrier height in an n-type material is shown to be

$$q\Phi_B = q(\Phi_m - \chi_s). \tag{70}$$

The above result is taken for the ideal case, when there are no surface charges present on the semiconductor. However, semiconductors such as GaAs have a high density of surface

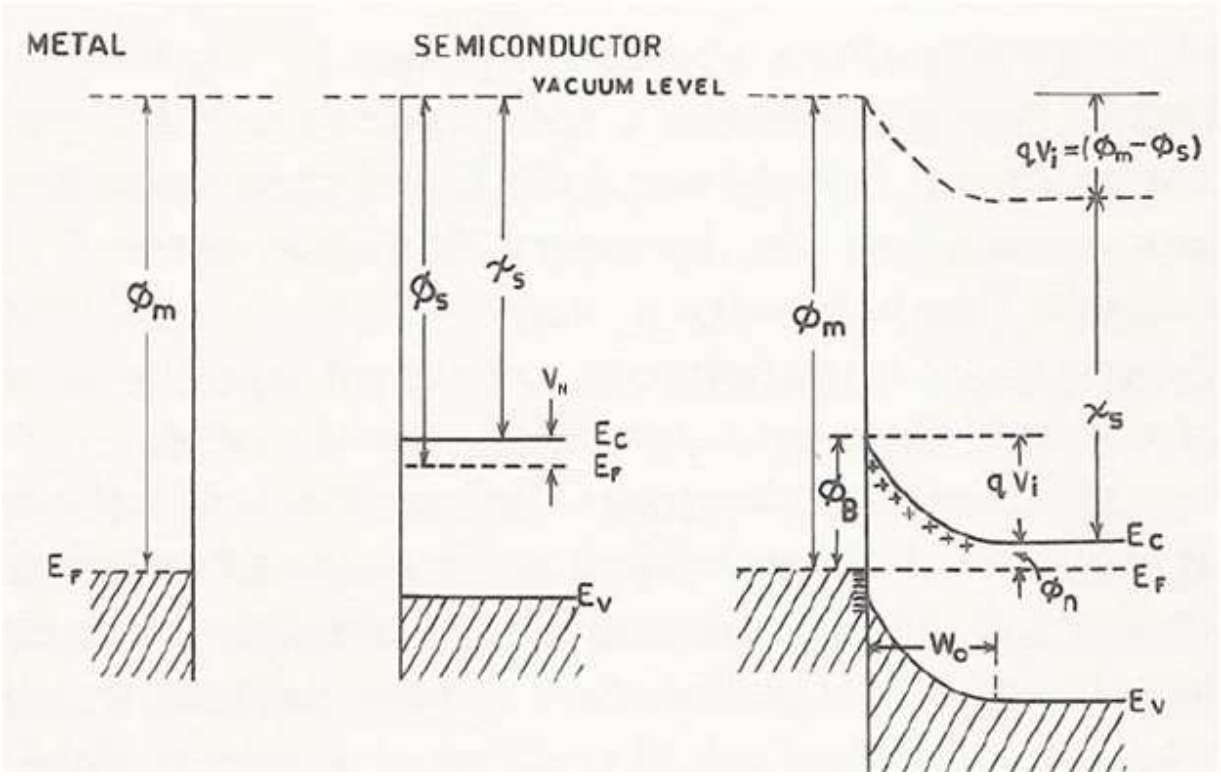

Figure 16: Energy band diagram of Schottky contact formation between a metal and an n-type semiconductor. Scanned from Ref [22], p.3

charges that must be taken into account when modelling the metal-semiconductor interface. If the surface states are at a high enough density, then the charge necessary to equalize the two Fermi levels is provided by the surface states, with little displacement to the Fermi level. Thus, for a semiconductor with a high density of surface states, the Fermi level is pinned and the barrier height is determined by the energy difference between the semiconductor's conduction

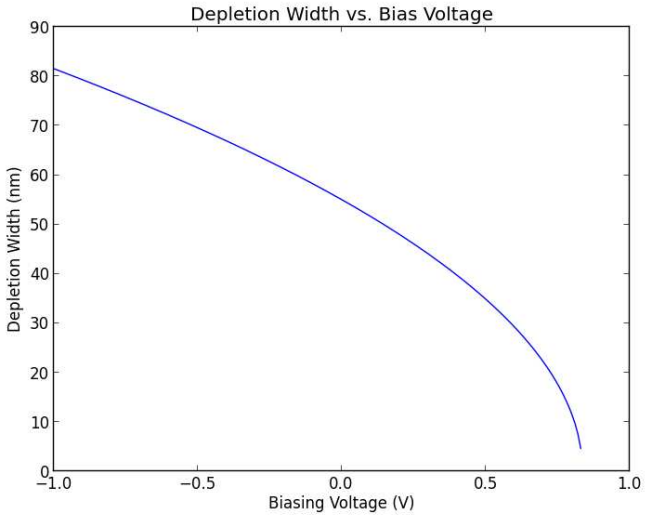

Figure 17: Depletion width modulated by biasing voltage.

band and the surface charge energy level, independent of the metal used.

Achieving equal Fermi levels between the two materials leads to the development of a depletion layer. To determine the thickness of the depletion layer, an analysis similar to that of the PN junction is performed, but with the depletion layer constrained to the semiconductor. In the metal and in the semiconductor layer outside of the depletion region, ρ=0 and $(x) = 0$, while within the depletion region in the semiconductor, ρ=eN_D. The result is that:

$$W = \sqrt{\frac{2\varepsilon_s}{qN_D}\left(V_{bi} - V - \frac{k_B T}{e}\right)} \quad \textbf{(71)}$$

$$(x) = \frac{qN_D}{\varepsilon_s}(W - x) \tag{72}$$

$$V(x) = \frac{qN_D}{\varepsilon_s}\left(Wx - {}^{1}/_{2}\, x^2\right) - \Phi_B \tag{73}$$

where ε_s is the electric permittivity, V_{bi} the built-in voltage, and V an applied bias to the metal and grounded through the semiconductor. The depletion width for an n-doped ($N_D = 4 \times 10^{17} cm^{-3}$) GaAs ($\varepsilon_s = 13.1\varepsilon_0$ [13]) with a Schottky barrier height Φ_B=0.836 eV is 55nm. The depletion width as a function of biasing voltage for this situation is shown in Figure 17.

Figure 18 shows the energy band diagram for a metal n-type semiconductor Schottky junction under reverse and forward bias.

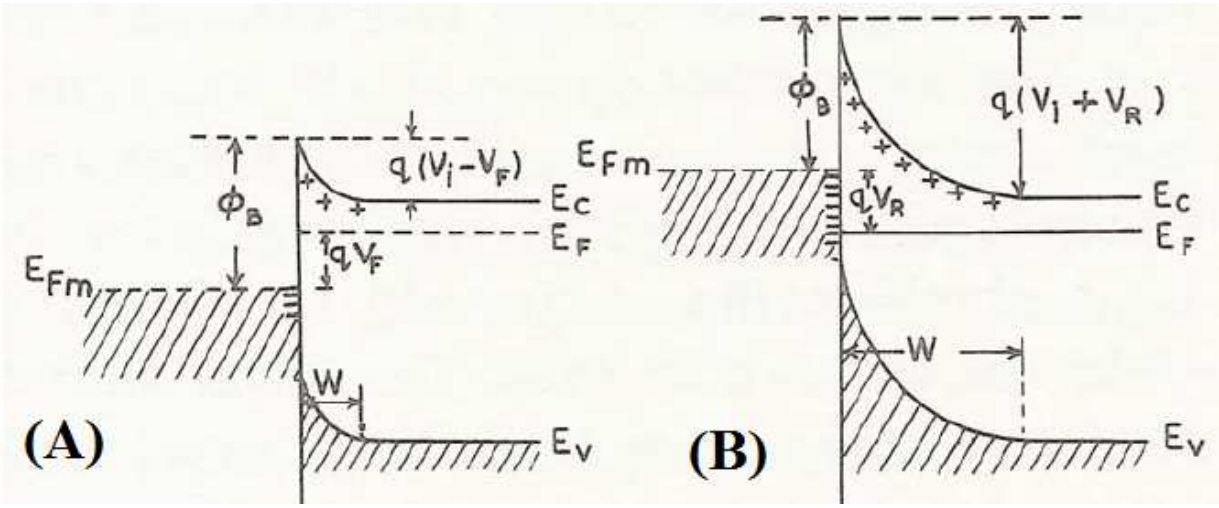

Figure 18: Schottky contact under (A) reverse and (B) forward bias. Scanned from Ref [22], p.3

In a Schottky contact, and generally for all semiconductor-metal contacts, the current transport is driven by the majority carriers. If the barrier height $q\Phi_B \gg k_B T$ and thermal equilibrium is reached at the interface and is not affected by the flow of current, the IV character of the Schottky contact may be modelled using thermionic emission theory. The full derivation

of the thermionic emission theory can be found in S.M. Sze's Physics of Semiconductor Devices, pages 255-258. The result under forward bias is that:

$$I = I_s\left(e^{qV/k_BT} - 1\right), \tag{74}$$

where $I_s = SA^*T^2e^{-q\Phi_B/k_BT}$ is the saturation current, where $A^* = \frac{4\pi q m^* k_B^2}{h^3}$ is the effective Richardson constant for thermionic emission and S the effective surface area of the diode. Figure 19 shows an experimental IV curve for a Schottky contact formed between n-type GaAs and Chromium.

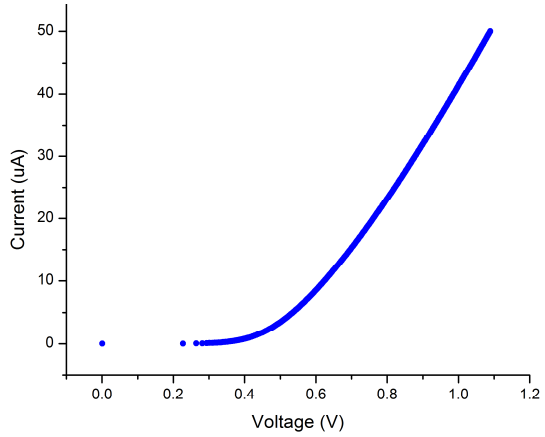

Figure 19: Experimental Schottky IV curve from Ref [23].

3.3 Ohmic

An Ohmic contact is a non-rectifying contact used extensively for its reliably linear IV relationship for a wide range of currents and voltages. The linear relationship arises from a negligibly thin barrier at the junction of the metal and semiconductor. An Ohmic contact is formed when $\Phi_m < \Phi_s$, i.e. the work function of the metal is less than the work function of the

semiconductor. When the two materials are brought into contact, negative charge flows from the metal into the semiconductor until the Fermi level is equal throughout the materials. Under both forward and reverse bias, negative charges are able to move freely across the interface without experiencing a barrier and the IV curve is therefore linear.

A final consideration is the specific contact resistance. The contact resistance is defined as $R_c = \left(\frac{\partial J}{\partial V}\right)^{-1}_{V=0}$ and is typically much smaller than the bulk resistance. For materials with doping $N_D \leq 10^{17} cm^{-3}$, the specific contact resistance is determined by thermionic-emission,

$$R_c = \frac{k_B}{qA^*T} e^{q\Phi_B/k_B T}, \tag{75}$$

where Φ_B is the otherwise negligibly small barrier formed between the metal and semiconductor [13].

3.4 JFET and MESFET

The field effect transistor (FET) is a transistor that has a conductive channel capable of being modulated by an electric field. The junction field effect transistor (JFET) is a three terminal MSH device that uses an applied voltage to modulate the two-point measured resistance. Figure 20 shows a schematic of a JFET, where an additional gate has been added to the bottom of the device to create a plane of symmetry that simplifies analysis. The JFET can be modelled as a two-dimensional device, with Ohmic contacts on opposing ends with one contact acting as the source and the opposing contact as the drain. The body of the device is either p- or n-type, with the gate contact being a material of the opposite carrier type, forming a PN junction with the body. A nearly identical device is the MESFET. MESFET operation is identical to a JFET, but instead of a PN-junction forming the gate, a Schottky contact is used.

The MESFET is preferred at times due to the ability to fabricate the gate under low temperature, as compared to p-n junctions, which are produced using high temperature processes. In terms of device performance, a MESFET has a lower resistance and lower IR drop along the channel, while the JFET is capable of various gate configurations that may be applied to improve high-frequency performance.

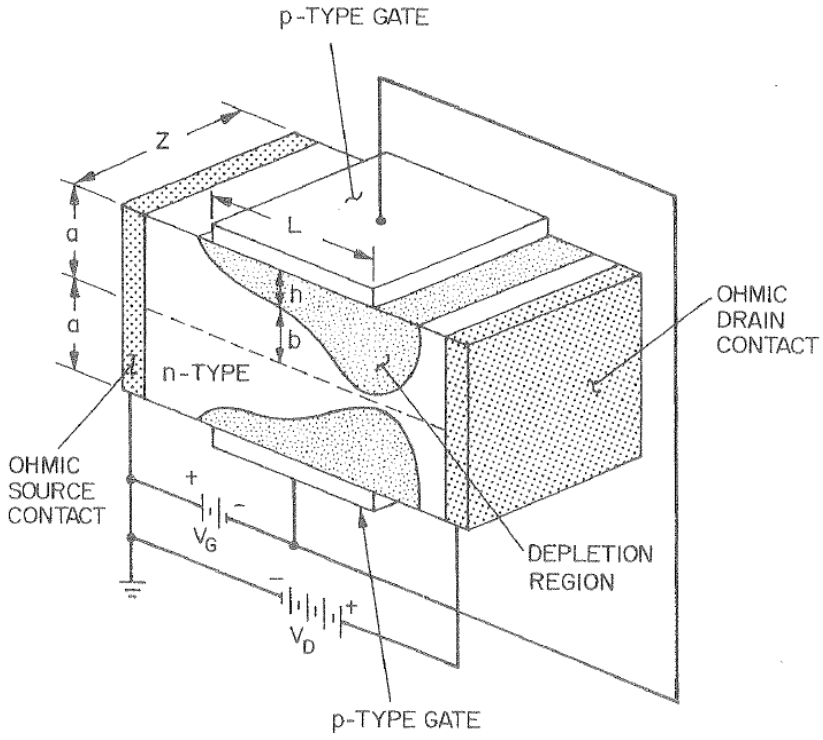

Figure 20: Schematic of JFET device. Scanned from Ref [13], p.314

The JFET device structure is characterized by the channel length *L* (also referred to as the gate length), channel width *Z*, channel depth *a*, depletion-layer width *h*, and a channel opening *b*, as shown in Figure 20. The traditional measurement scheme for an n-type body device is as follows: the source contact is set to ground, with the drain (V_D) and gate (V_G) voltages measured with respect to the grounded source. When the gate bias is $V_G \leq 0$, increasing the drain voltage

increases the channel current until, at large V_D, the current saturates to I_{Dsat}. Figure 21 shows a typical I-V plot for a JFET at various biases.

It is possible to derive an analytical expression for the IV characteristics of the JFET and MESFET by applying the following approximations: $L \gg a$ (i.e. the long channel

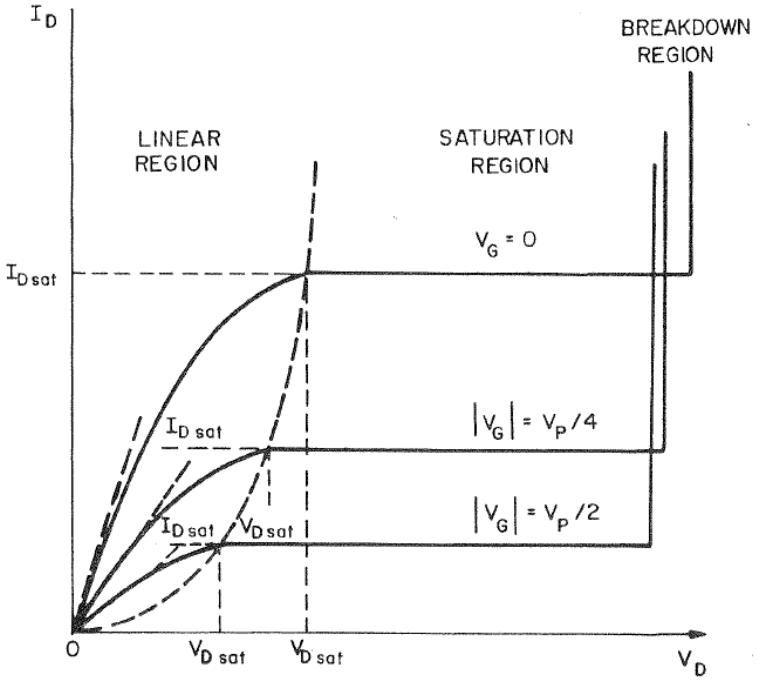

Figure 21: Typical I-V curve for JFET. Scanned from Ref [13], p. 315

approximation) where the channel changes gradually, the depletion layer is abrupt and the carrier mobility is constant [13]. These approximations make it possible to reduce the system to one-dimension (typically taken as *x*), with the second-dimension (typically taken as *y*) built into the model as a change in the depletion channel width as a function of *x*. Solving the one-dimensional Poisson equation in the *x*-direction, the depletion-layer width is found to be

$$h = \sqrt{\frac{2\varepsilon_s(V(x) + V_G + V_{bi})}{qN_D}}. \quad \textbf{(76)}$$

The depletion width at the source (x=0) and drain (x=L) end is

$$h(x=0)=\sqrt{\frac{2\varepsilon_s(V_G+V_{bi})}{qN_D}} \tag{77}$$

$$h(x=L)=\sqrt{\frac{2\varepsilon_s(V_D+V_G+V_{bi})}{qN_D}}. \tag{78}$$

Assuming a positive drain voltage, the maximum depletion width is equal to the channel depth, a. The corresponding voltage is the pinch-off voltage and is defined as

$$V_P=\frac{qN_Da^2}{2\varepsilon_s}. \tag{79}$$

Finally, the drain current can be shown to behave as

$$I_D=I_P\left\{3\,{V_D}/{V_P}-2\,\frac{\left[(V_D+V_G+V_{bi})^{3/2}-(V_G+V_{bi})^{3/2}\right]}{V_P^{3/2}}\right\}, \tag{80}$$

where $I_P={Z\mu q^2N_D^2a^3}/{6\varepsilon_sL}$ is the pinch-off current. The drain current maximum, I_{Dsat}, is maximum when $h(x=L)=a$, i.e. when the channel is pinched off. At pinch-off,

$$I_{Dsat}=I_P\left[1-3\left(\frac{V_G+V_{bi}}{V_P}\right)+2\left(\frac{V_G+V_{bi}}{V_P}\right)^{3/2}\right], \tag{81}$$

These results apply to devices that fall under the approximations given earlier. However, these approximations no longer accurately reflect the physics of the device as ${a}/{L}$ increases or the drain voltage becomes larger. These new conditions increase the influence of two-dimensional effects and require further consideration. The drift velocity vs electric field for

GaAs is shown in Figure 22. This complicated field dependent mobility has important implications for devices with regions of high electric field.

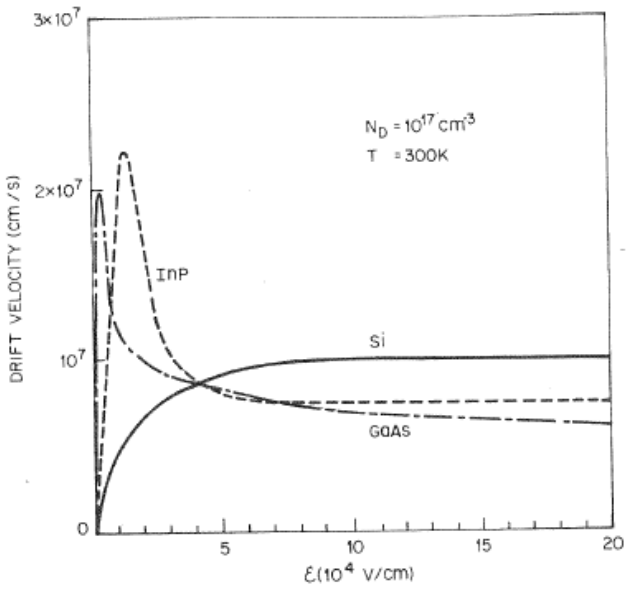

Figure 22: Drift velocity for GaAs, InP and Si as a function of electric field intensity. Scanned from Ref [13] p. 325.

The final statement concerning JFETs and MESFETs is one concerning the noise behavior of the devices. JFET and MESFET are low noise devices, since the charge transport phenomenon are driven by majority charge carriers. However, the extrinsic resistances in real devices lead to non-ideal noise performance. The equivalent circuit for noise analysis is shown in Figure 23. From this circuit, the optimum noise figure, F_0, for a GaAs MESEFET has been found to be

$$F_0 = 1 + \frac{fL}{4}\sqrt{g_m(R_S + R_G)}, \quad \textbf{(82)}$$

where f is frequency, L is the gate length, g_m is the current generator, R_S is the circuit series resistance and R_G is the gate metallization resistance. In order to optimize low noise performance, a shorter gate length and minimum values for series and gate metallization resistances are desired.

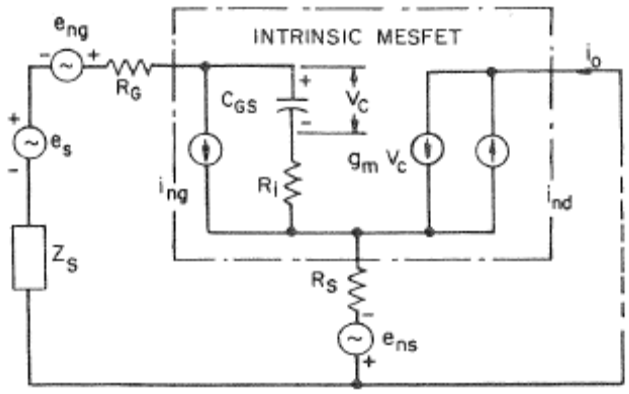

Figure 23: Equivalent MESFET circuit for noise analysis. Scanned from Ref. [13], p. 347.

3.5 Van der Pauw measurement

In 1958, L.J. van der Pauw published his venerated paper, "A method for measuring specific resistivity and hall effect of disks of arbritrary shape. [24]" The monograph has been widely cited and the method used extensively for determining a sample's resistivity, doping type, sheet carrier density and mobility of the majority carriers. The method's high utility is in its ability to accurately measure these properties for a sample of arbitrary shape so long as the following conditions are satisfied:

(a) The contacts are at the circumference of the sample
(b) The contacts are sufficiently small
(c) The sample is homogeneous in thickness
(d) The surface of the sample is singly connected, i.e., the sample does not have isolated holes [24]

Figure 24 shows the sample structure originally proposed by van der Pauw. The method employs four Ohmic contacts around the perimeter. If the contacts are labeled clockwise 1-4, as shown in Figure 24, the four point resistance of the sample is found by sourcing a positive DC

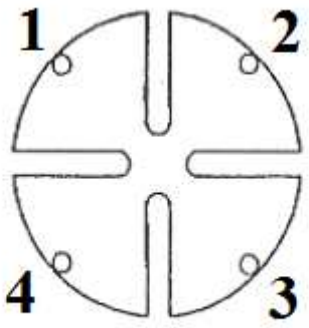

Figure 24: van der Pauw structure for four-point resistance measurements. Image from Ref [24].

current through contact 1 and grounded to contact 2 while measuring voltage using leads 3 and 4. The four-point resistance is calculated as

$$R_{12,34} = {}^{V_{34}}/_{I_{12}} \tag{83}$$

This measured resistance is the sheet resistance scaled to a geometric factor. The four-point, or Kelvin, resistance measurement is favored because it removes the contribution of contact resistance and the series resistance of the measurement system. Van der Pauw successfully showed the sheet resistance could be found by taking two rotated four-point resistance measurements and calculated the sheet resistance by solving

$$e^{-\pi R_{12,34}/R_S} + e^{-\pi R_{23,41}/R_S} = 1 \tag{84}$$

3.6 EXX Devices

As discussed in the Introduction, this dissertation focuses on investigating how the geometry of extraordinary Electroconductance (EEC) sensors influences their extraordinary phenomenon in order to optimize their performance. The following is an overview of the different EXX phenomenon to date.

3.7 Extraordinary Magnetoresistance (EMR)

The first extraordinary phenomenon discovered was extraordinary magnetoresistance (EMR) [4]. The phenomenon was initially realized in the four-point resistance measurements of InSb van der Pauw disks with an imbedded concentric cylindrical Au inhomogeneity (Figure 25a) [4] and later demonstrated in four-point resistance measurements of shunted InSb:Au van der Pauw plates (Figure 25c) [5].

The junction between the semiconductor and metal in both geometries is Ohmic. When operated under ambient conditions, the current travels through the path of least resistance, through the metal shunt, and the measured four-point resistance of the device is therefore closer in magnitude to that of the metal. A magnetic field applied perpendicular to the plane of the device increases the interface resistance between the semiconductor and metal, thereby constraining the current to the semiconductor and increasing the measured resistance. The EMR is defined as

$$EMR = \frac{R(H) - R_0}{R_0} \times 100\%, \quad \textbf{(85)}$$

where $R(H)$ is the device resistance under an applied magnetic field and R_0 is the resistance measured under no applied magnetic field.

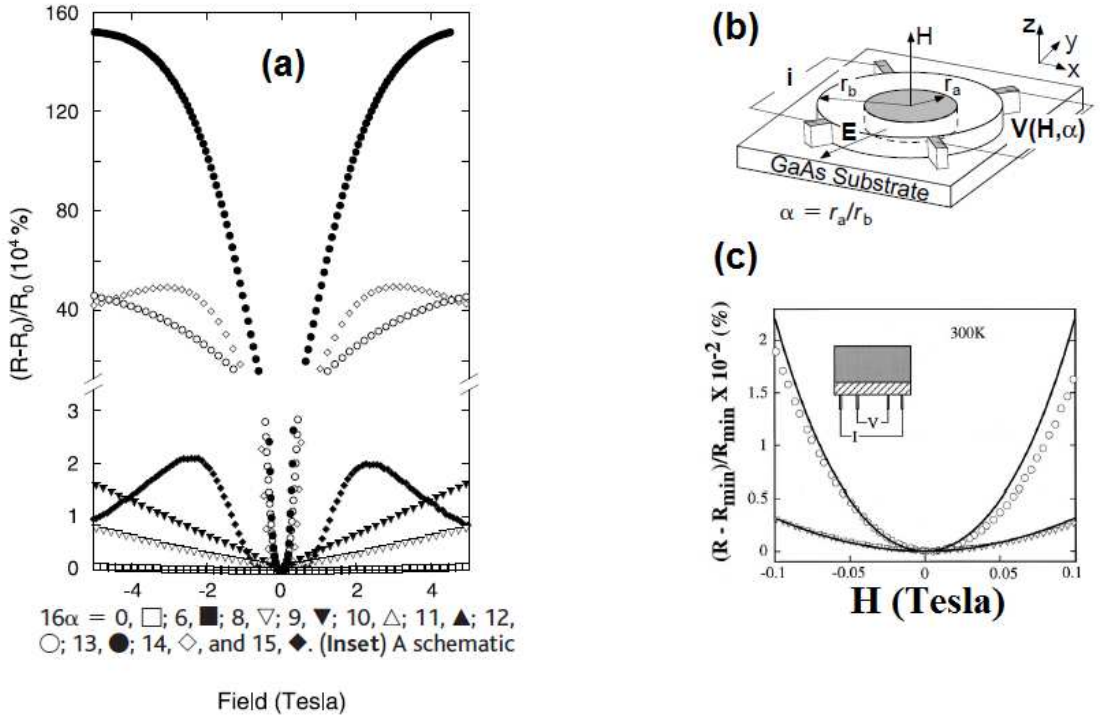

Figure 25: (a) EMR response of (b) van der Pauw disk and (c) van der Pauw bar EMR devices. Figures adapted from Ref [4], [5]

Figure 25 shows the EMR for both the van der Pauw disk and plate devices. The van der Pauw disk was observed to exhibit an EMR of 100%, 9100% and 750,000% at magnetic fields of 0.05, 0.25 and 4.0 T, respectively, while the van der Pauw bar showed an EMR of 100% under a field of 500 Oe, all at room temperature.

3.8 Extraordinary Pieozoconductance (EPC)

Extraordinary piezoconductance (EPC) phenomenon occurs in sensors that are sensitive to uniaxial tensile strain [6]. The device structure is identical to the previously discussed van der Pauw bar used in EMR devices. The application of a uniaxial tensile strain, ε, on the device reduces the metal-semiconductor interface resistance, thereby increasing the flow of current through the metal and decreasing the overall measured resistance. EPC is defined as

$$EPC = \frac{|R(\varepsilon) - R_0|}{R_0} \times 100\%, \tag{86}$$

where ε is the applied strain and R_0 the resistance of the device with zero strain, i.e. ε=0.

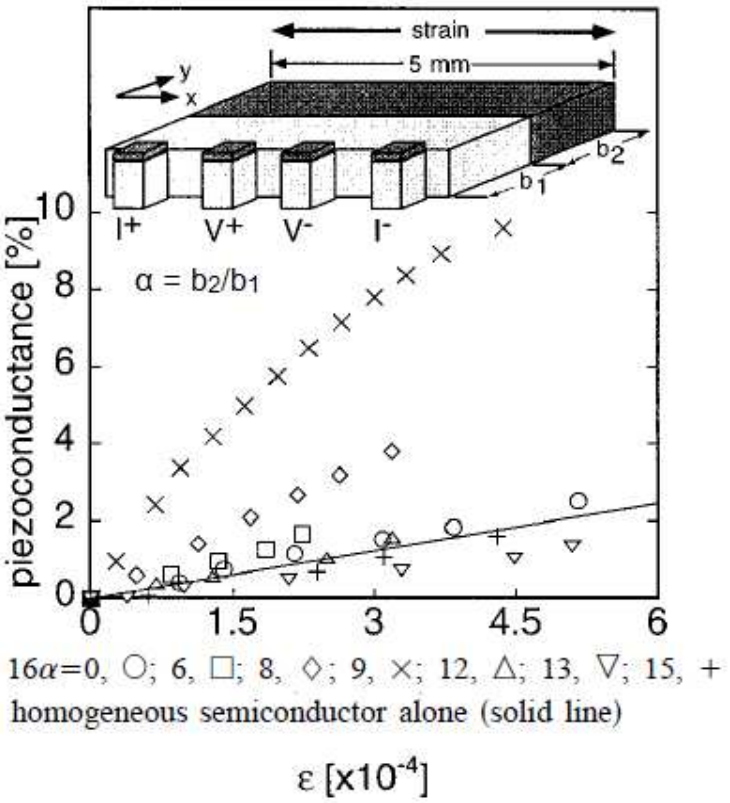

Figure 26: EPC vs. Strain for different device geometries. Figure from Ref [6].

Figure 26 shows the EPC response for several different structure ratios, as defined in the schematic inset. These results are compared to the response of a homogenous semiconductor, establishing the geometrically tunable responsivity of the device to applied strain. The EPC devices realized a more than five times greater responsivity to applied strain than the homogenous devices.

3.9 Extraordinary Optoconductance (EOC)

The extraordinary optoconductance (EOC) phenomenon occurs in sensors that have a spatially-dependent responsivity to local laser illumination [7], demonstrated for both InSb:In and GaAs:In van der Pauw plates. A laser beam with a spot size less than the device dimension is scanned across the device, photogenerating local electron-hole pairs and inducing a bias that is measured using the two inner leads.

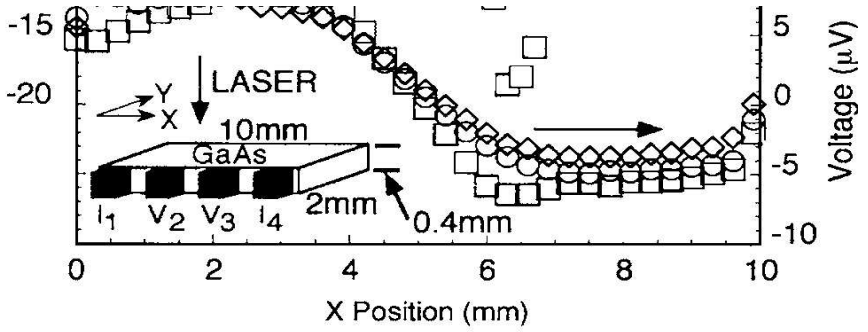

Y=0 mm, □; 0.5 mm, ○; and 1.0 mm, ◇

(a) an In-GaAs MSHs (b) a bare GaAs sample

Figure 27: Induced photovoltage on EOC Device and bare GaAs sample at T=15K using 20mW of 476.5 nm laser radiation focused on sample with Gaussian spot size of radius 10 μm. Figure adapted from Ref. [7]

The optical response of the device is attributable to the Dember effect, with the induced voltage magnitude and sign dependent on the laser spot location. The electrons have a higher mobility than the holes in GaAs and therefore diffuse away from the laser spot more quickly than

the holes. As a result, the locally illuminated area develops an excess of positive charge that causes a position dependent change in potential.

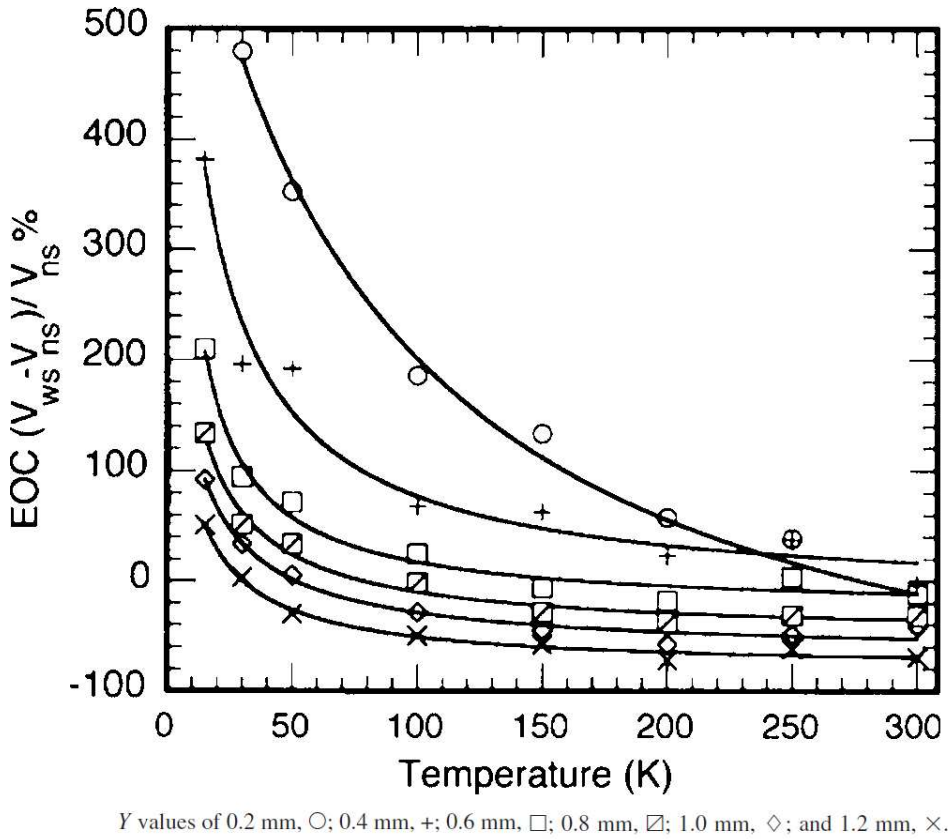

Y values of 0.2 mm, ○; 0.4 mm, +; 0.6 mm, □; 0.8 mm, ▨; 1.0 mm, ◇; and 1.2 mm, ×.

Figure 28: The temperature dependence of the EOC. The measurements were acquired with the illuminating laser beam at a fixed position of X=3.5 mm and Y values as defined. Figure adapted from Ref. [7].

Figure 27 shows the induced photovoltage in a GaAs:In EOC device and a bare GaAs sample as a function of beam position along the leads axis,x, for a fixed set of y-distances away from the leads. While the plot shows the absolute change in voltage, the EOC is defined as

$$EOC = \frac{[V_{23}(x)]_{\text{with shunt}} - [V_{23}(x)]_{\text{without shunt}}}{[V_{23}(x)]_{\text{without shunt}}} \times 100\%, \quad \textbf{(87)}$$

where the '23' subscript represents the voltage lead locations.

Since the EOC response relies on the mean free path of the photogenerated charge carriers, it is sensitive to temperature and can be fitted to

$$EOC(T) = \frac{a}{T+b} + c \tag{88}$$

Figure 28 shows the temperature dependence of the EOC response for GaAs:In devices fitted to Eq (88). As the temperature is decreased, the photogenerated carrier mobility is interpreted to increase, resulting in a larger EOC response. An EOC of 480% is realized at 30K, but is reduced to 15% at room tempeture (300K).

3.10 Inverse Extraordinary Optoconductance (I-EOC)

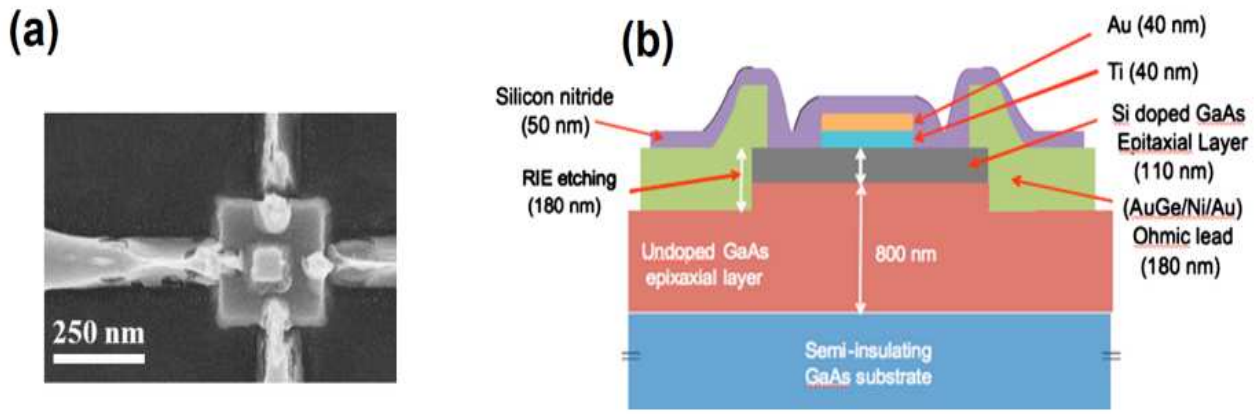

Figure 29: (a) SEM overview of IEOC sensor (b) Schematic Side view. Figures adapted from Ref. [9].

Inverse extraordinary optoconductance (I-EOC) phenomenon is realized in MSH optical nanosensors that exhibit room temperature positive photoresistance [9]. The device structure is a square mesa of doped semiconductor with a concentric square shunt, similar to the original EMR devices. The device resistance is found by measuring the four-point resistance while under uniform optical illumination. While the EOC phenomenon was achieved using an Ohmic

junction perpendicular to the current plane, the I-EOC phenomenon is realized using a Schottky junction parallel to the current plane. A schematic of the I-EOC structure is shown in Figure 29.

While micron-scale devices of the same device structure display a decrease in photoresistance under increasing light irradiation, scaling the device down to submicron length scales results in the emergence of I-EOC phenomenon, with an increasing photoresistance under increasing light irradiation. This phenomenon is related to the original EOC phenomenon since both are driven by the interplay between the mean free path of photogenerated charge carriers and the location of measurement leads. The response of the I-EOC devices to illumination can be explained by considering ballistic and diffusive transport. The mean free path, λ_P, of electrons in the doped GaAs epitaxial layer has been measured to be $18\ \text{nm} \leq \lambda_p \leq 35\ \text{nm}$ for $2\ \text{K} \leq T \leq 300\ \text{K}$ [25]. The separation between the Ohmic leads and shunt (L) in the 500 nm device varies from 20 to 40nm and 15 to 30 nm for the 250 nm device. Thus, $L \sim \lambda_P$ and $L < \lambda_P$, respectively and a significant fraction of the carriers travel ballistically through the device. Under illumination, the photoinduced carrier concentration results in additional scattering and the carrier transport transitioning from ballistic to diffusive, leading to an increase in the measured four-point resistance.

Figure 30 shows a plot of the micron and submicron scale device's four-point resistance as a function of light intensity. The I-EOC sensitivity is observed to increase with decreasing device size. Device performance can be evaluated by the relative photoresistance, defined as

$$\delta R(P) = \frac{R(P) - R_0}{R_0} \times 100\%, \tag{89}$$

where R_0 is the dark resistance and P the power illuminating the active region. The relative photoresistance of the 500nm and 250nm devices is 965% (1.0 nW) and 9462% (0.25 nW), respectively, while the relative photoresistance of the 5μm and 1μm is only 6% (2 nW) for both. Finally, the 250 nm device under 633 nm of illumination shows a specific detectivity of $D^* = 5.06 \times 10^{11}\text{cm}\sqrt{\text{Hz}}/\text{W}$ with a dynamic response of 40 dB [9].

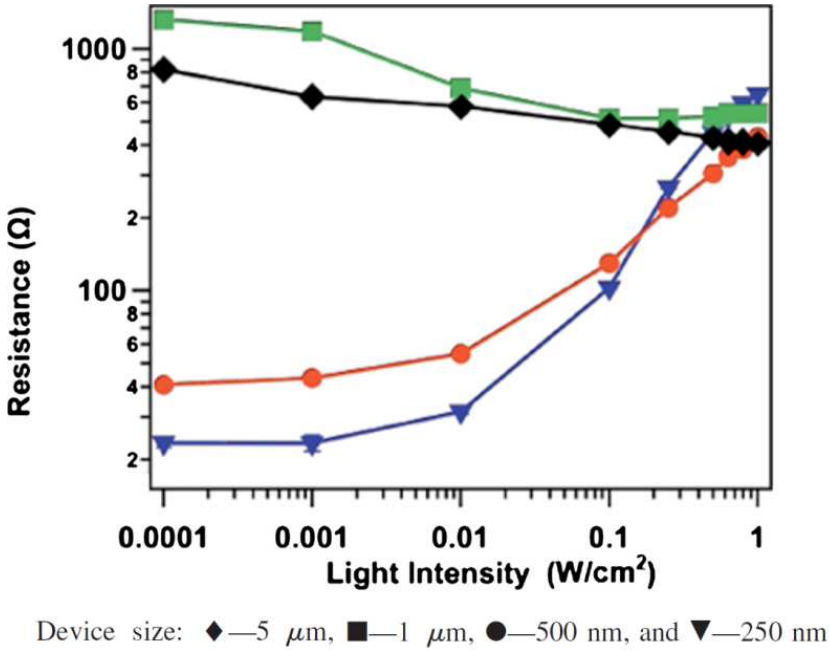

Figure 30: Photoresistance of MSH Devices under 632.8 nm laser illumination. Figure adapted from Ref. [9]

3.11 Extraordinary Electroconductance (EEC)

Extraordinary Electroconductance (EEC) phenomenon is realized in the MSH devices shown schematically in Figure 31 [10]. The device structure is a cylindrical n-type GaAs mesa with a concentric metal patterned in the center (referred to as the shunt) and forming a Schottky interface with the mesa. The four-point resistance of the device is measured via the four Ohmic leads around the perimeter of the mesa. The geometry of the shunt and mesa is expressed as the unitless parameter $\alpha = {}^{r_{shunt}}/_{r_{mesa}}$, where r is the respective radius. When a static electric field

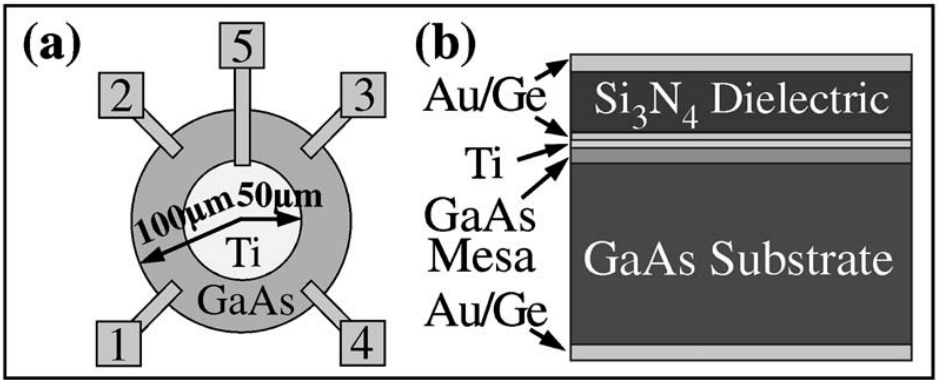

Figure 31: (a) Device schematic (b) Device side-view. Figure from Ref. [10]

is applied to the junction, directly or indirectly, the depletion width within the device is modulated and the current carrier properties are modified, leading to a measureable change in the four-point resistance.

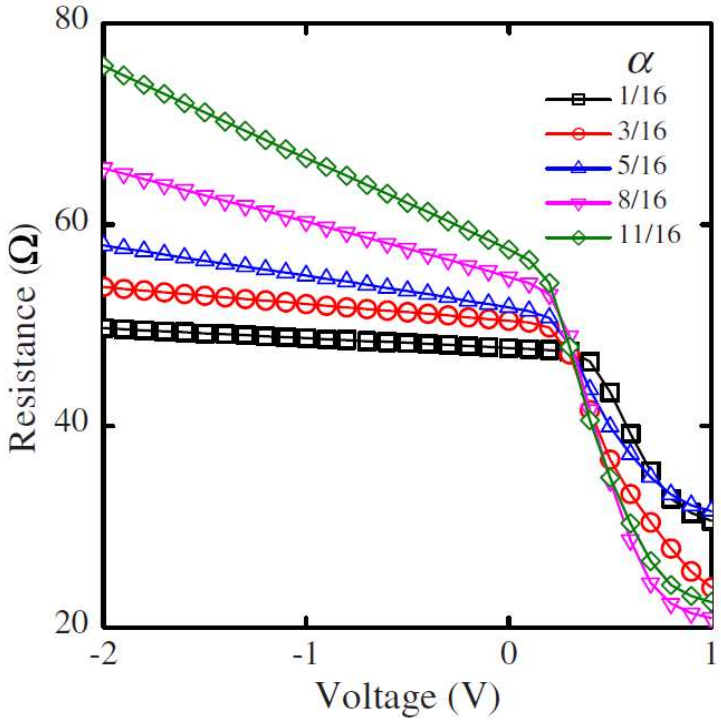

Figure 32: Four-lead resistance of EEC devices with r_M=60µm under direct bias. Figure from Ref. [10].

The EEC devices can be operated under direct or indirect biasing. Under direct biasing, a bias is applied to the shunt via lead 5, and the biasing ground tied to the grounding current lead. The four-point resistance is then measured as a function of applied bias. Under forward bias, diode current travels through the semiconductor and reduces the four point resistance. Reverse biasing a micron scale EEC device (i.e. $r_s > 60\mu m$) leads to an increase in the measured four point resistance that can be modeled as an increase in the depletion region. The four-point resistance of an EEC device under bias is shown in Figure 32.

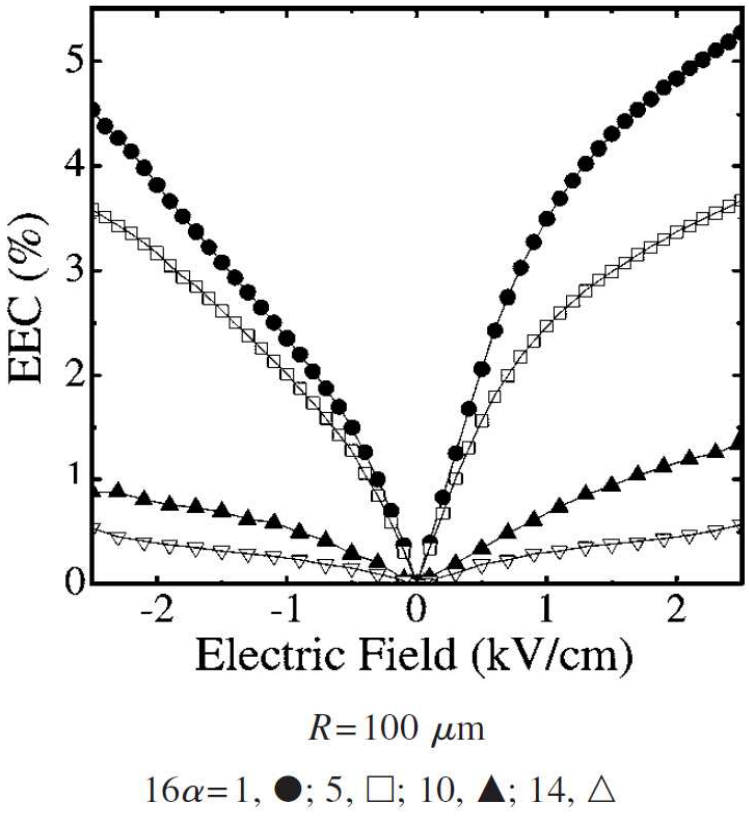

Figure 33: EEC vs Electric Field. Figure from Ref [10]

Indirect biasing refers to applying an external electric field normal to the interface and measuring the four-point resistance. This has been experimentally achieved by sandwiching the EEC device between a parallel plate capacitor and applying a bias between the top and bottom

plates to generate the static electric field. Qualitatively, the EEC response to indirect biasing mirrors that seen under direct bias, with resistance decreasing under a forward electric field and increasing under a reverse field. Figure 33 shows the EEC device response to an indirect bias for varying α and EEC is defined as

$$EEC = \left|\frac{G(E) - G_0}{G_0}\right| \times 100\%, \quad \textbf{(90)}$$

where G is the device conductance. An EEC device with mesa R=100μm and α=1/16 has a maximum 5.2% EEC effect, which corresponds to a resolution of 3.05 V/cm at a bias field of 2.5 kV/cm.

4 EEC Device Fabrication

The fabrication of the multilayer EEC devices requires several processing steps and employs both photo and electron beam (ebeam) lithography. They are fabricated using an epitaxial wafer grown by molecular beam epitaxy and purchased from IQE Inc. The active region of the device is a 200nm thick, Si-doped (N_D=4x10^{17} cm^{-3}) GaAs epitaxial layer (R_s =840.90 Ω/square) followed by an undoped 800nm thick epitaxially grown GaAs layer for electrical insulation with a semi-insulating GaAs substrate (thickness, *t*=350μm) at the bottom to lend structural robustness. The wafer is diced by a third party into 7.5mm square chips.

The EEC device fabrication steps can be divided into the following major processes: i) patterning of alignment marks via photolithography and thermal deposition; ii) patterning of the epitaxial mesa via ebeam lithography and reactive ion, etching (RIE); iii) formation of Ohmic leads via photolithography, thermal deposition and thermal annealing; iv) formation of Schottky contact via electron beam lithography and thermal deposition.

Following the fabrication of the EEC device, they are made electronically accessible by wirebonding the Ohmic pads around the perimeter of the chip to a ceramic leadless chip carrier. The chip carrier was then placed in a custom fabricated light-tight box for testing.

4.1 Patterning of Alignment Marks

Alignment marks were patterned on the diced epitaxial GaAs chips. The process of alignment mark patterning is shown schematically in Figure 34, with the referenced photolithography image reversal process shown in Figure 38. The alignment marks deposited on the chips were used for both photo and ebeam lithography alignment throughout the fabrication processes of the devices. Accordingly, gold (a high Z material) was used to ensure a high contrast between the semiconductor and alignment marks imaged in the scanning electron

microscope (SEM) during alignment throughout the electron beam lithography process. To prevent alignment mark lift-off throughout the multiple processing steps, a capping layer of NiCr was applied. An adhesions layer of chromium was deposited between the metal stack and GaAs to prevent lift off.

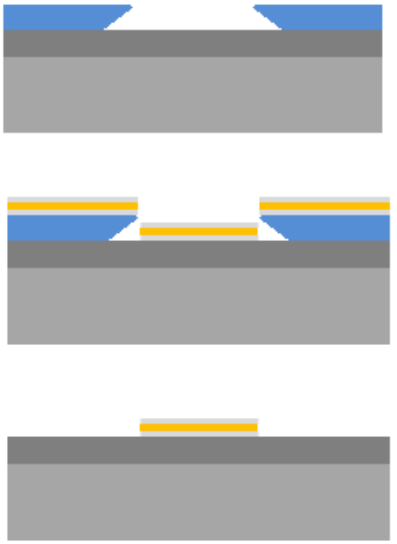

Photolithography – Image Reversal (Figure 38) of alignment pattern using AZ-5214 IR

Thermally evaporate Cr/Au/NiCr

Lift Off

Figure 34: Thermal Deposition

4.2 Patterning of Epitaxial Mesa

The epitaxial mesa was first patterned using ebeam lithography by exposing a resist layer

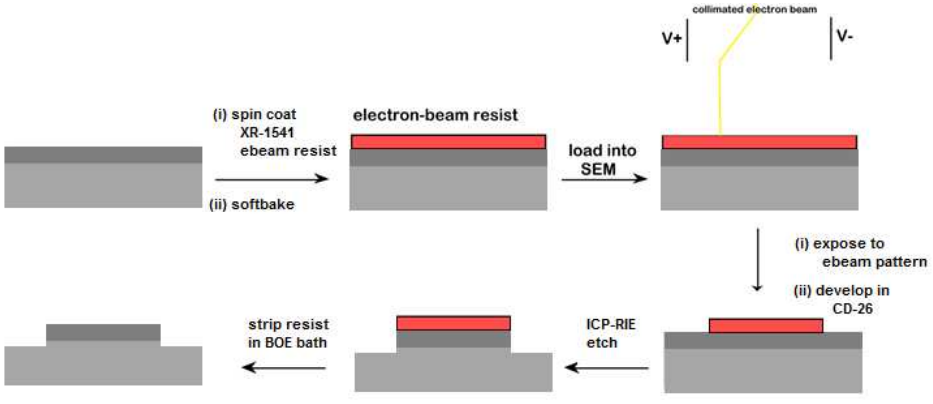

Figure 35: Mesa Patterning

of approximately 60nm thick coating of Dow Corning XR-1541 hydrogen silsesquioxane (HSQ) to an electron beam rastered in the desired mesa pattern. The resist coated GaAs chip was then etched in an Oxford Plasma 100 ICP-Reactive Ion etcher using published BCl_3 chemistry [26]. This process is shown schematically in Figure 35. To ensure proper etch depth, a dummy chip was partially covered with AZ-5214 resist and etched for 60s in the ICP-RIE. The dummy chip was then cleaned and the etch depth measured using an Alpha-Step D-100 Profilometer. Based on the measured etch depth, the etch rate was calculated and the etch time to achieve a 270nm etch depth was calculated. A second dummy chip was then prepared, etched for the prescribed etch time and measured to guarantee an etch depth of 270nm. Following confirmation of the etch time, the EEC device chip was etched. The final step in mesa patterning was removing the developed ebeam resist, HSQ. After HSQ is exposed to the electron beam energy, it becomes amorphous SiO_2, which is etched at a rate of 2nm/s by 6:1 buffered oxide etch (BOE) [27].

4.3 Patterning of Ohmic Leads

The Ohmic leads were formed using the established AuGe/Au/Ni process [28] with an 80s anneal at 450°C in a nitrogen rich environment. The photolithographic process followed was the same as that taken for the alignment mark but with different deposited metals. Prior to thermal deposition, the chips were soaked in BOE to remove native oxides, then transferred to the thermal evaporator within 10 minutes of removal from the BOE bath. So long as the native oxide layer is less than 10Å, it is transparent to electrons [13]. The formation of Ohmic leads was confirmed by the linear two-point measured IV curve of the contacts, shown in Figure 37.

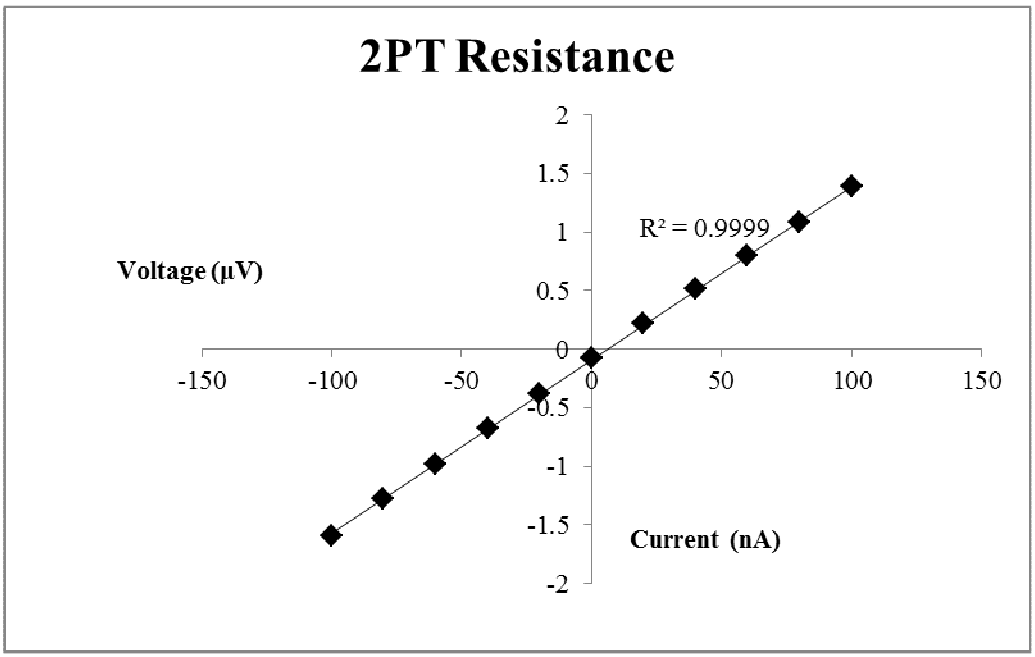

Figure 37: 2PT IV Curve of EEC Device using probe station. From Ref [23].

4.4 Patterning of Schottky Contact

The Schottky contact was the final step in EEC device fabrication. The Schottky pattern was formed using ebeam lithography and the metal deposited using thermal evaporation. The surface of the chip was cleaned following the process described for the Ohmic leads prior to

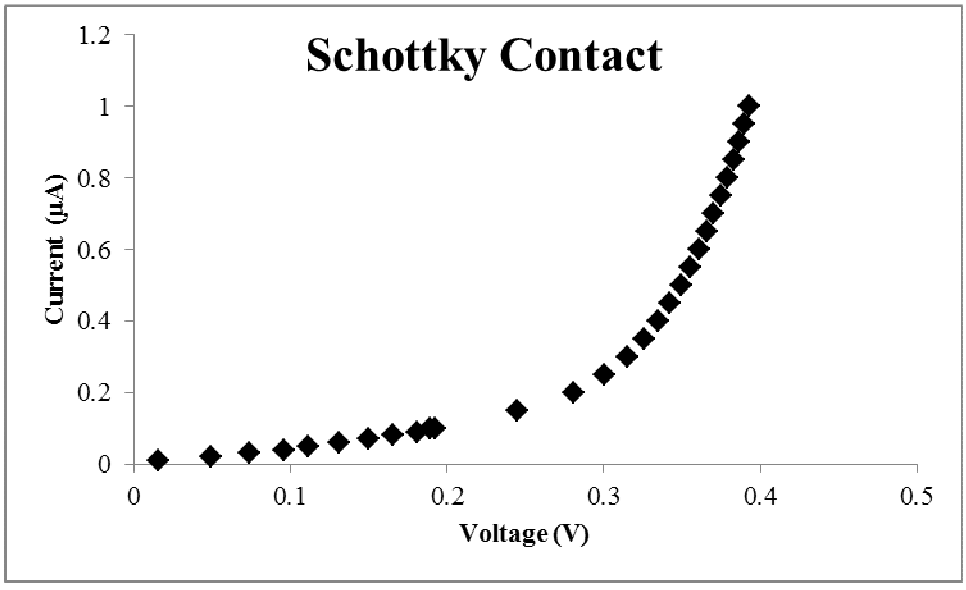

Figure 36: Schottky contact of EEC Device using probe station. From Ref [23]

thermal evaporation. Schottky character was confirmed via two-point IV measurements using a probe station, the result of one measurement shown in Figure 36.

Photolithography – Image Reversal

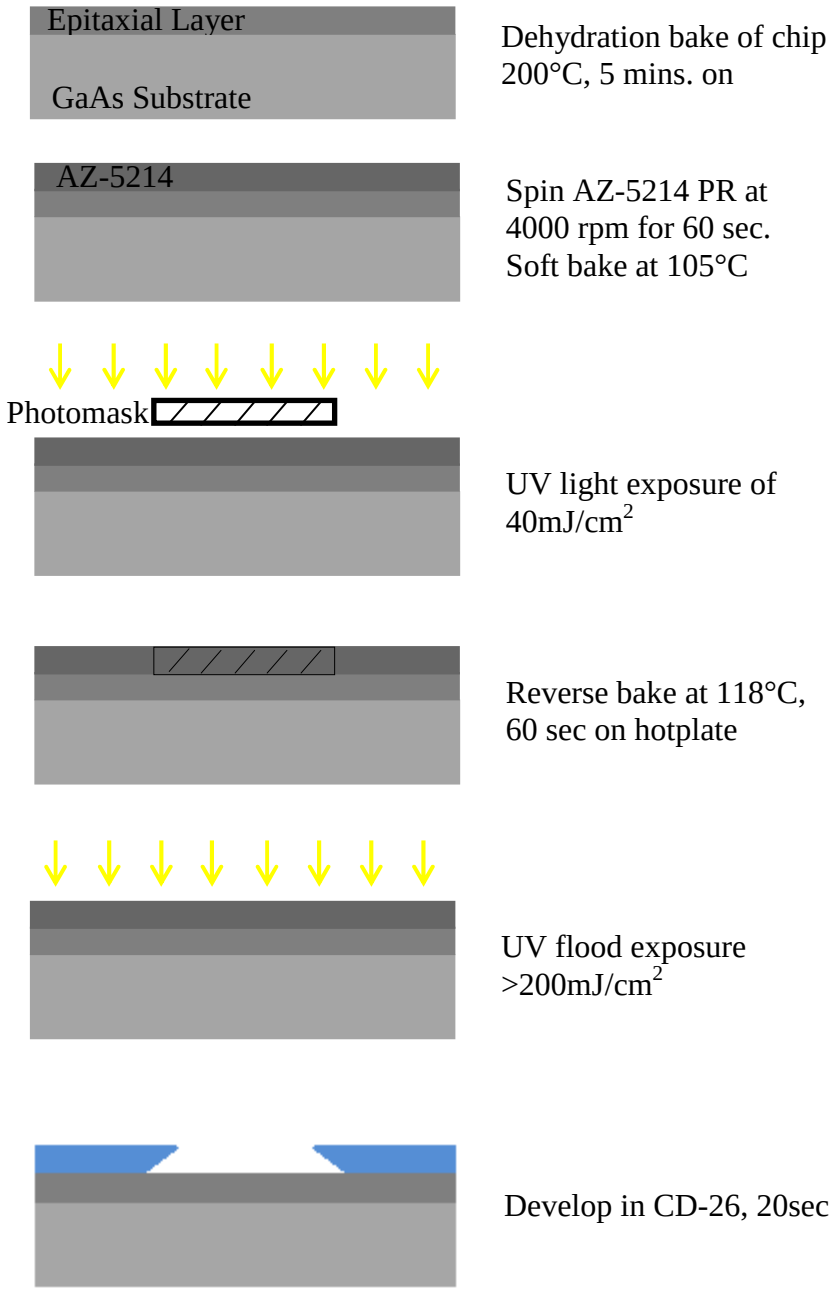

Figure 38: Photolithography Image Reversal

5 Photo Effects at the Schottky Interface in Extraordinary Optoconductance

L.C. Tran, F. M. Werner, A.K.M. Newaz and S. A. Solin

Department of Physics and Astronomy, Washington University in St. Louis, 1 Brookings Drive, St. Louis, MO 63130

5.1 Abstract

Non-uniform optical illuminations near the Schottky interface of Ti/GaAs metal-semiconductor hybrid (MSH) structures induces local photovoltages transverse and lateral to the interface. In these VLSI-compatible, room temperature optical sensors, the optical response of the MSH resistance is directly linked to the Schottky barrier behavior. In order to correlate the interface behavior with the overall heterostructure behavior, quantities such as transverse photovoltage, lateral photovoltage, and resistance are all recorded as a function of laser spot location. The interface's photovoltaic dependence on intensity is consistent with a MSH in which quantum efficiency is independent of optical intensity.

5.2 Introduction

Inverse extraordinary optoconductance (I-EOC) has recently been shown to be the basis for a class of highly sensitive, room temperature optical detectors with a minimum pixel diameter of 250 nm, a specific detectivity of $D^* = 5.06\times10^{11}$ cm$\sqrt{\text{Hz}}$/W and a dynamic response of 40 dB [9]. The I-EOC effect in which resistance is seen to increase with illumination intensity is observed in structures of dimension less than 1 μm; sensors of pixel diameter equal to 1 μm exhibit normal EOC, in which resistance decreases with intensity. While studying the impact of optically induced carrier excitations on the Schottky barrier at the GaAs/Ti interface in I-EOC and EOC sensors, it was noted that the position of the Gaussian laser illumination beam could induce a positive or negative voltage offset to the current-voltage characteristic curves across the

Schottky interface (Figure 39). Further study of the offset effect at the shunt and its impact on EOC measurements is carried out in this work.

5.3 Experimental Methods

The Si-doped, 100nm n-GaAs epilayer was grown by molecular beam epitaxy on an 800 μm thick insulating GaAs buffer layer (grey in Figure 40). This 100 nm thick active layer was patterned with photoresist and, etched in a chemical bath of citric acid and 30% hydrogen peroxide at a 20:1 volume ratio to form the mesa (yellow in Figure 40). After each round of photoresist patterning, to insure a removal of residual organic polymer contaminants in the patterned channels, the wafer underwent 30 seconds of O_2 plasma, etching to descum the substrate surface. After wire patterning, the native oxide was removed by soaking the wafer in

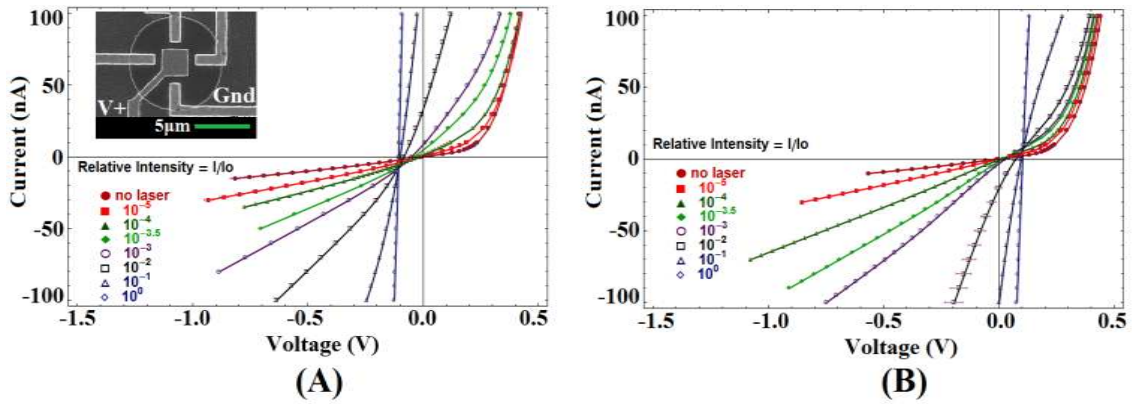

Figure 39: Current-Voltage characteristic across Schottky interface for a 5μm EOC sensor under varying laser intensities at a location of (A) negative photovoltage offset and (B) positive photovoltage offset. (Inset) a scanning electron microscope (SEM) image of EOC sensor with electrical connection labels of V+ and Ground for Schottky interface study shown in main figure.

1:1 volume ratio of HCl and deionized water. After stripping the native oxide, the wafer was loaded as quickly as possible into the vacuum chamber of a metal evaporator to minimize the exposure to atmospheric oxygen and regrowth of oxide. Ohmic contacts were formed by annealing the evaporated metal thin films of AuGe (88:12), Ni, and Au at thicknesses of 40/16/40 nm respectively (orange in Figure 40). The annealing process was under constant N_2

flow at 450 C for 1 minute. The shunt metal was a Ti and Au bilayer of 40/40 nm respectively and was not annealed to maintain an abrupt material interface (red in Figure 40). Heat treatment was also limited after this stage.

The sensors studied in this work consisted of a 120 μm-diameter semiconductor mesa

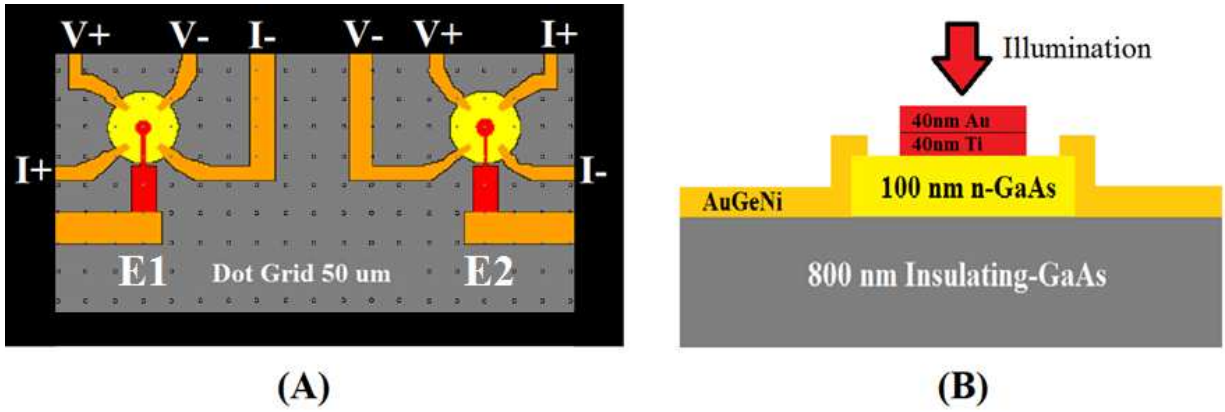

Figure 40: (A) Schematic of the epoxied sensors, the active (+) and passive (-) contact configuration, and identification of the epoxied sensors as "E1" and "E2"; red is Ti, yellow is n-GaAs, orange is Au/Ge/Ni, grey is insulating GaAs substrate, black is epoxy. For scale, note the dot grid spacing of 50 μm. The epoxied sensors E1 and E2 were nearly identical except for how they were connected to electrical sources and meters. (B) Cross section of EOC device illustrating shunt-metal side illumination. Dimensions not to scale.

with a concentric metal shunt of 40-50 μm diameter forming a Schottky interface on top of the mesa. The sensor four-point resistance was measured via four equidistant Ohmic leads around the perimeter of the device. The n-GaAs (Si-doped), 100nm thick epilayer had mobility μ = 3225 $cm^2V^{-1}S^{-1}$ and $N_D = 4x10^{17}$ cm^{-3} (yellow in Figure 40 (A-B)). The standard EOC sensor leaves the shunt metal isolated and floating in the center of the mesa. However, a tab and fifth lead were added to directly access the Schottky interface to monitor photo-effects. The shunt is accessed by a 200 μm long tab extending from the shunt to the Ohmic fifth lead. There is a Ti-GaAs interface beneath the tab as well as the shunt as shown in Figure 40 which introduces an asymmetry to the standard EOC structure.

As an optical block, one set of sensors was covered with opaque, black epoxy on the substrate and Ohmic leads except in the near vicinity of the sensors (black border in Figure

40(A)). The response of the shielded pixel to optical perturbation was then compared to a second identical pixel with no epoxy shielding, similar to the I-EOC and EOC sensors in which the offset behavior was first noted.

To study the Schottky interface a two-point measurement of open-circuit voltage (V_{oc} →I = 0 nA) was made between the shunt and one of the four Ohmic leads, (see the inset of Figure 39). The effective resistance of the EOC heterostructure (R_{4pt}) is determined using a four-point (van der Pauw) measurement at the four Ohmic contacts [24]. As shown in the labeling of Figure 40(A), a 1.3 Hz, 5 μA square wave is passed through pins I+ and I- from a Keithley 6221 Current Source and the voltage across pins V+ and V- was measured on a Keithley 2182A Nanovoltmeter. From the voltage at high and low polarity of the square wave, V_{high} and V_{low} respectively, two numbers were extracted: the effective resistance and the photo-induced voltage offset. The DC offset voltage calculated from the four point resistance measurement is referred to as "V_{off}" to distinguish it from the two point measurement across the shunt, V_{oc}. This is a distinction in name only. Since the same measured value of V_{off} could be collected separately from the four point configuration with the current source disconnected, it is accurate to think of V_{off} as an open circuit voltage of the Ohmic contacts.

$$R_{4pt} = \frac{V_{high} - V_{low}}{2\,I} \tag{91}$$

$$V_{off} = \frac{V_{high} + V_{low}}{2} \tag{92}$$

Using a computer controlled Agilent 34925 MUX card and Agilent switch mainframe, the R_{4pt}, V_{off}, and V_{oc} response is compared for a series of sensors while they were exposed to different local laser intensities from the Gaussian profile.

The light source used in this study was a 5 mW, 632.8 nm HeNe laser. The unfocused beam waist was 1.344±0.018 mm as measured by the razor edge method [29] and upon focusing the minimum beam waist at the sensor face was 16-30 μm. The laser was held stationary while the sample stage was moved by two crossed, computer controlled, linear actuators. The 2-D laser rastering maps in Figure 41 and Figure 42 record the position of the two actuators on the map axes and the measured R_{4pt}, V_{off}, and V_{oc} values as the coloration of the data.

5.4 Results

Using the unfocused beam as a light source, the V_{oc} of the non-epoxied sensor plotted in Figure 41(A) shows a distinct bi-lobed response and the V_{oc} of the epoxy-covered sensor E1 shown in Figure 41(B) shows a single-lobed feature. Shrinking the beam waist to 16-30 μm, a bi-lobed open circuit voltage is recovered in the epoxy covered sensor (see Figure 41(C)). Further,

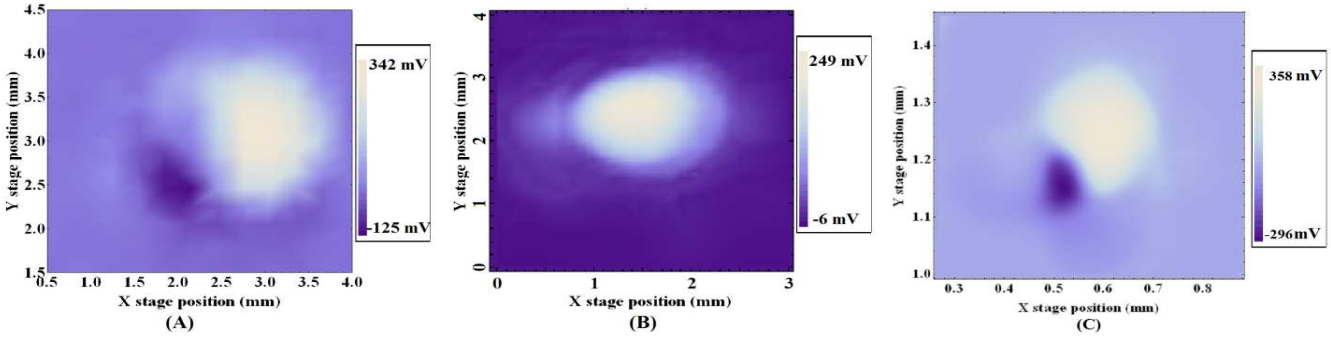

Figure 41: The sensor design is pixel E1 from Figure 40. The epoxied and non-epoxied sensors shown here were otherwise identical. (A) bi-lobed V_{oc} with no epoxy, unfocused beam (B) single lobed V_{oc} with epoxy, unfocused beam (C) bi-lobed V_{oc} with epoxy, focused beam

the epoxied sensor shows a response ~2 mm in diameter for the unfocused beam and ~0.2 mm in diameter for the focused beam.

Figure 42(A-B) show that the R_{4pt} response for sensors E1 and E2 have slight asymmetric regions that remain high valued and do not decrease in resistance with the increasing

beam intensity. The four-point resistance leads were configured in different orientations with respect to the Au/Ti tab (indicated as a red line overlaid on the data in Figure 42). In Figure 40, the current source leads are marked by (I+) for the contact actively altered between positive and negative current polarization during generation of the square wave and (I-) for the grounding contact which remains grounded for both polarizations of current. The contact labels for the nanovoltmeter are active/reference (V+) and ground (V-). The asymmetries in R_{4pt} in Figure 42 correlate to the location of the active contacts and the positive lobe of V_{off}.

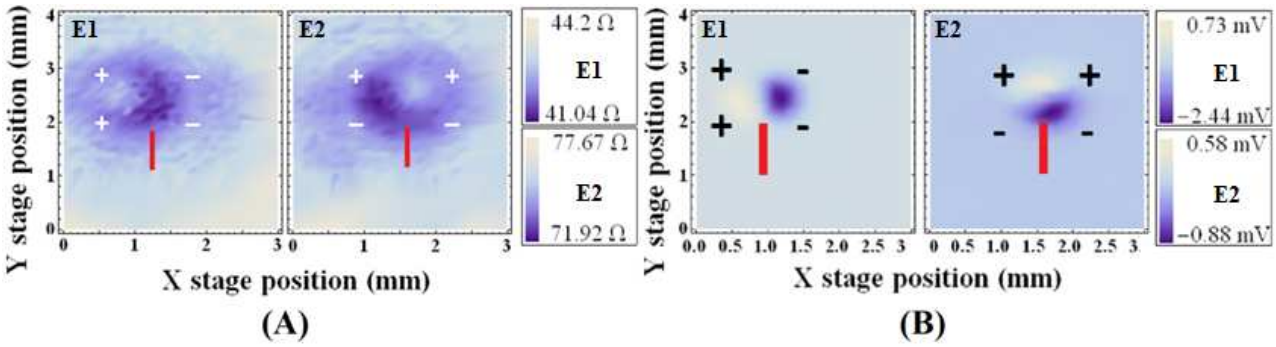

Figure 42: Red line indicates location of a shunt tab,+ indicates active leads, and – indicates ground for epoxied sensors E1 and E2 (A) Laser rastering map, unfocused beam: four terminal resistance response (B) Laser rastering map, unfocused beam: DC voltage offset of resistance measurement, V_{off}

5.5 Discussion

5.6 Lateral photovoltaic effect at Ohmic contacts

The lateral photovoltaic effect (LPE) was identified by Schottky in 1930 and expanded upon analytically by Wallmark (1957) [30]. For a good qualitative discussion, see also Henry, et al. (2002) [31]. The lateral photovoltaic effect arises when an inhomogeneous illumination is incident on a junction of two materials with different conductivities. In the case of a p-n junction, while the transverse photovoltage (across the junction) is the basis for power generation from a photocell, the lateral photovoltage (parallel to the junction plane) was proposed by Wallmark as the basis for a new position-dependent photo detector. For illumination localized between the voltage sensing contacts, Wallmark showed that the voltage should vary as

$$V \approx \rho i_l x, \qquad 1.$$

linearly with illumination location, x, substrate resistivity, ρ, and total lateral current density, i_l

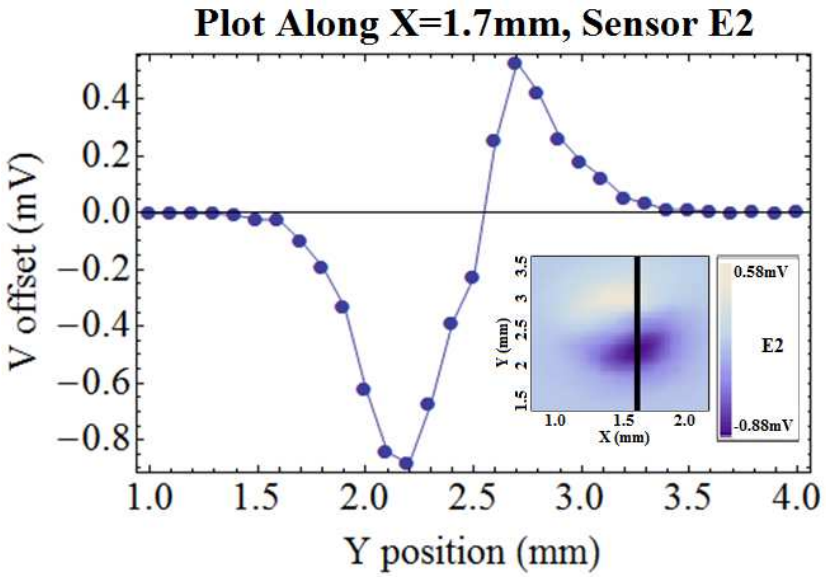

Figure 43: Line section of V_{off} data for EOC sensor B in Figure 42(b) along line X = 1.7 mm (see inset). The scale bar needs to be included for the image plot.

While previous generations of EOC detectors with an Ohmic GaAs-In interface [8] have been well modeled according to the Dember effect [32], the rectifying Schottky shunt and the strong internal fields induce charge separation and voltage variation that agrees well with Wallmark's LPE for a p-n junction. Figure 43 shows a line section of V_{off} data (across two of the Ohmic contacts) for epoxied detector E2 in Figure 42(B). In magnitude of response and form, the V_{off} results are quite similar to the LPE. Between Y = 2.2 and 2.7 mm the linear relationship to position of illumination is evident.

There are some differences in design – most obviously that the LPE detector is diffused p-n junction based, consisting of an In dot (which forms a p-region on recrystallization) alloyed to n-Ge. The In metal dot (comparable to our shunt) is on the bottom of the Ge substrate, on the opposite side from the illumination source. Electron-hole pairs are generated and separated along

the entire interface and built-in electric field region of the p-n junction. As was indicated in Figure 40(B), the illumination of the EOC sensors is on the side of the metal shunt that causes the rectifying junction to form, which is opposite the orientation of the LPE sensor. Although the 80nm of Ti and Au metal is thick enough to be opaque to 632 nm light and electron hole pairs can only be expected to be generated around the periphery of the metal mesa rather than along the entire two-dimensional interface that does not seem to have significantly affected the functional shape of the position dependence.

5.7 Lateral photovoltage at the Schottky contact

The V_{oc} behavior of the EOC sensors demonstrates both a transverse photovoltage and a lateral photovoltage, a non-uniform illumination effect. The characteristic transverse behavior is distinguished from any lateral effects by limiting a uniform illumination to the high internal field, Schottky junction region with application of epoxy as in Figure 41(B) and in Figure 44. Under uniform illumination intensity ($I_{opt} = P_{opt}/Area$), the expected behavior for a transverse photovoltage where the quantum efficiency (η) is not a function of intensity is $V_{oc} \propto (C + l\,n[I_{opt}])$ where C is independent of I_{opt} since $V_{oc} \propto ln[I_{sc}]$ and $I_{sc} \propto \eta P_{opt}$ where I_{sc} is the short circuit current. Figure 44 demonstrates that $V_{oc} \propto (C + l\,n[I_{opt}])$ for these sensors under near-uniform illumination. The laser was expanded to a beam waist of 1 mm and centered on the pixel, which implies that the intensity would decrease by only 4% at the epoxy border. The intensity was then modulated using neutral density filters. From the linear relationship with intensity in Figure 44, the shape of V_{oc} in Figure 41(B) can be attributed to a characteristic transverse photovoltage which is dependent on the integrated intensity of the Gaussian profile over the sensor face. In Figure 41(B) the pixel size was ~ 1/20 the beam diameter and

V_{oc} approximates the inverted parabola form of $V_{oc} \propto \left(C' - ((x - x_o)^2 + (y - y_o)^2)\right)$ for a point-sized Schottky interface in a Gaussian beam profile where $I_{opt} \propto I_o e^{-((x-x_o)^2+(y-y_o)^2)}$.

However, for the non-epoxied sensor in Figure 41(A) and epoxied sensor in Figure 41(C), the metal contacts are affected by the non-equilibrium charge concentration of the excess minority carriers at the laser spot. Thus, the V_{oc} responses show a transverse behavior overlaid with a lateral behavior. Since the mobility of electrons in GaAs is much higher than that of holes, the laser spot will tend to induce a local positive charge. The location of the negative lateral

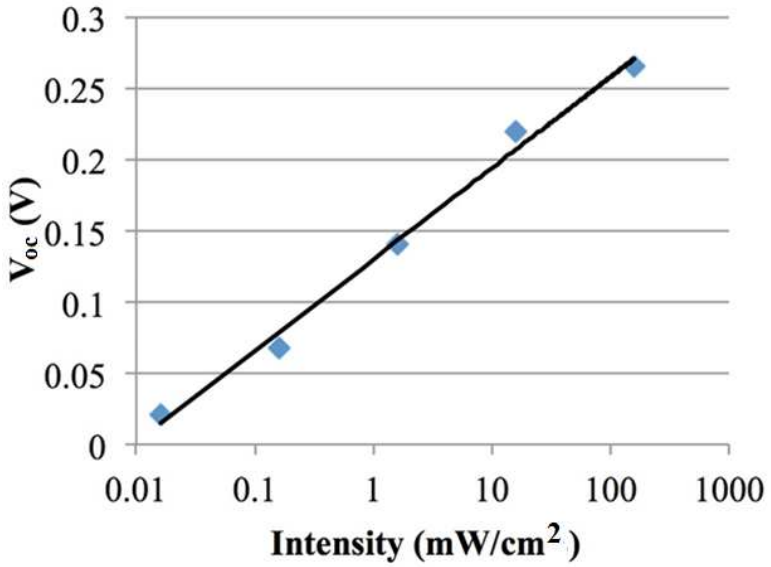

Figure 44: Voltage-Intensity relationship under near uniform illumination of epoxied sensor. The solid line is a least squares fit to the data yielding V_{OC} = 0.0278 ln(Intensity) + 0.1301 and R^2 = 0.9911

photovoltaic lobe in Figure 41(A) and (C) correlates with the location of the ground contact and the sign of the voltage variation is consistent with an excess of holes at the ground lead. When the illumination is predominantly near the shunt tab, the positive voltage lobe of the lateral photovoltage is subsumed in the positive voltage due to the transverse photovoltage. The V_{oc} of Figure 41(A) for X stage position greater than 2.7mm appears qualitatively very similar to the transverse behavior isolated in the experiment in Figure 41(B). For both sensors in Figure 41(A)

and (C), the transverse voltage behavior dominates when non-uniform illumination is on the opposite side of the shunt/tab contact from the ground contact. For both Ohmic and Schottky interfaces, the lateral photovoltage is only non-zero when illumination is non-uniform between the two metal contacts (see Figure 43). In summary, it is clear that both lateral and transverse photovoltaic effects can be present in the V_{oc} of tabbed EOC sensors under local, non-uniform illumination.

5.8 Concluding Remarks

The V_{oc} of the epoxied sensor's shunt interface should be the most similar to the interface behavior we could expect from a standard EOC sensor in which the shunt metal is isolated and electrically floating in the center of the mesa. However, we have also demonstrated that with a focused beam, local variations in minority carrier density can cause a negative V_{oc} in the sensor active area and ~100 μm of exposed contacts. It is not clear that the Schottky interface would exhibit lateral effects the same degree when the metal tab and shunt is replaced an isolated, symmetric shunt. To support this, the slight asymmetry in R_{4pt} associated with the positive lobe of the LPE has not been noted previously in standard EOC sensors without a tab. The influence of the tab on photo effects deserves further attention to understand exactly what in the orientation of the contacts or the shape of the tab and Ti-GaAs causes the asymmetry in R_{4pt} since this resistance represents the standard measurement made on an EOC sensor.

5.9 Acknowledgements

This work was supported by the National Science Foundation under Grant Number ECCS-0725538. S.A.S. is a co-founder of PixelEXX, a start-up company, and has a financial interest in the company whose mission is to market imaging arrays.

5.10 Addendum: Effect of Local Illumination on an EEC Device

The local responsivity to optical perturbation was found for an extraordinary electroconductance (EEC) device with mesa radius r_M = 160 μm and shunt radius r_S = 30 μm. Similar to the previously published EOC response [8], the photogenerated voltage in the EEC device was measured as a function of beam position, using a beam waist much smaller than device dimension to isolate the local responsivity. While EOC devices employ an Ohmic junction perpendicular to the current pathway, the EEC devices use a Schottky junction in parallel with the current pathway. The EEC device voltage measured while under local optical illumination was the open circuit voltage of the Schottky interface, contrasted with the EOC voltage measurement of the two inner Ohmic leads of a van der Pauw bar.

A HeNe laser beam with wavelength 632.8nm and power 5.25mW was focused using a 20X microscope objective. The beam waist along the beam line after passing through the microscope can be expressed as

$$w(z) = w_0 \sqrt{1 + {(z - z_1)^2}/{z_0{}^2}} \tag{93}$$

where w_0 is the minimum beam waist, z_1 the location of the minimum beam waist, $z_0=\pi w_0^2/\lambda$ the Rayleigh range, where λ is the wavelength of light, and z defines the distance along the beam path from the position of the minimum beam waist at z_1. To find the minimum beam waist and characterize the beam, the beam waist was measured in 50 micron increments along the laboratory's z-axis about the visually observed focal point after passing through the microscope objective.

The width of the beam can be found using the "razor blade method." The razor blade method uses a photosensor to measure the beam intensity as a sharp edged, opaque block (i.e. a razor blade) moves into the beamline and partially blocks the beam, as shown in Figure 45. Since the laser emits in TEM_{00} mode, the power of the beam follows a Gaussian distribution given by

$$I(x,y,z) = \frac{2P_0}{\pi w(z)^2} \exp\left(-2(x^2+y^2)\Big/ w(z)^2\right), \tag{94}$$

where P_0 is the power of the beam .

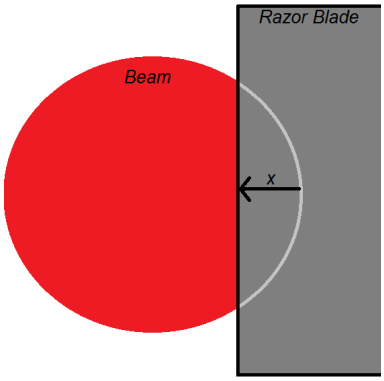

Figure 45: Razor Blade method

If part of the beam is covered by a razor blade, then the power impinging on the detector is given by the power of the beam minus the covered power, P_C, calculated as

$$P(x) = P_0 - P_C = \int_{-\infty}^{\infty}\int_{-\infty}^{\infty} I(x,y)dxdy - \int_{-\infty}^{\infty}\int_{-\infty}^{x} I(x,y)\,dxdy$$

$$= \int_{-\infty}^{\infty}\int_{x\prime}^{\infty} I(x,y)dxdy \qquad \textbf{(95)}$$

$$= \frac{P_0}{2}\left[1 - \text{erf}\left(x\sqrt{2}\Big/ w(z)\right)\right]$$

Examples of the fitted beam waist measurements are shown in Figure 46. Taking nine beam

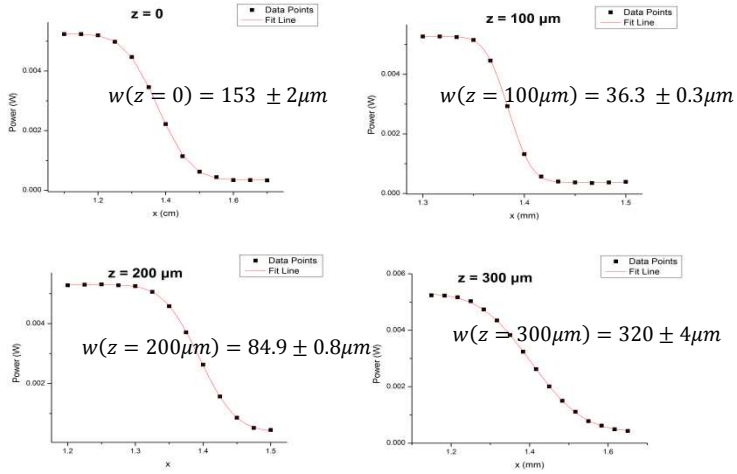

Figure 46: Calculating beam waist using the razor blade method

waist measurements at 50 µm increments along the z-axis, it is possible to fit the beam waist as a function of position using Eq. (93).

The plot of beam waist vs z position is shown in Figure 47. The 2-parameter fit yields a minimum beam waist w_0=1.69±0.008 µm. Using a plumb bob to determine height, a precision of ±20 µm along the z-direction was achieved, resulting in an estimated beam waist w~30±15µm.

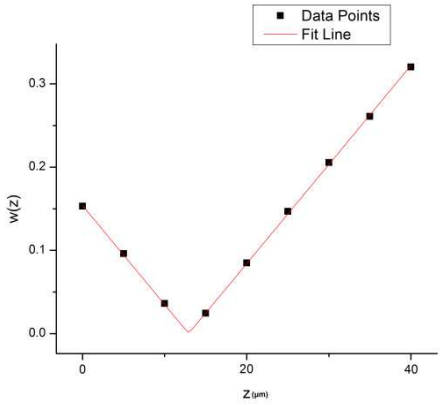

Figure 47: Beam waist vs z

The EEC device was placed at the distance mentioned above. Using electronically controlled stage motion controllers, a grid of 300μm X 300μm with step size spacing of 10μm was scanned, with the EEC device in the middle of said grid. At each (x,y) location, the open circuit voltage, V_{OC}, was measured. A schematic of the scanning condition is shown in Figure 48.

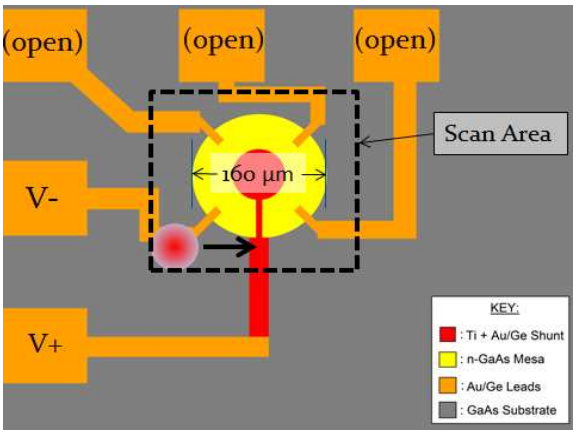

Figure 48: Scan condition

The open circuit voltage as a function of beam position is shown in Figure 49. When the beam is positioned in the vicinity of the shunt, the open circuit voltage is seen to grow more and more positive, while the beam position near the grounding lead generated a negative V_{oc}.

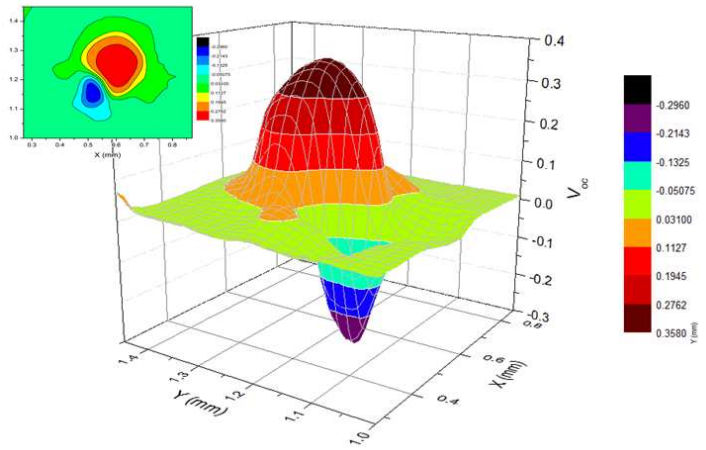

Figure 49: Open-circuit voltage as a function of beam position (inset: contour plot of V_{oc})

This behavior can be understood in light of a lateral photovoltaic effect occurring in the Schottky diode. Choosing a line that spans the maximum and minimum values of V_{oc} and plotting the open-circuit voltage as a function of displacement, one can observe the tell-tale sign of lateral photovoltaic effect. Figure 50 compares the result with the original paper on the photovoltaic effect by Wallmark, suggesting optical perturbation as attributable to the lateral photovoltaic effect.

While previous publications have established the EEC device as an electric field sensor [10] and light intensity sensor [9], this work presents further versatility for EEC devices as sensitive to beam position through use of the measured open circuit voltage. This work also supports previous results published concerning broad inhomogeneous illumination of EEC sensors [14].

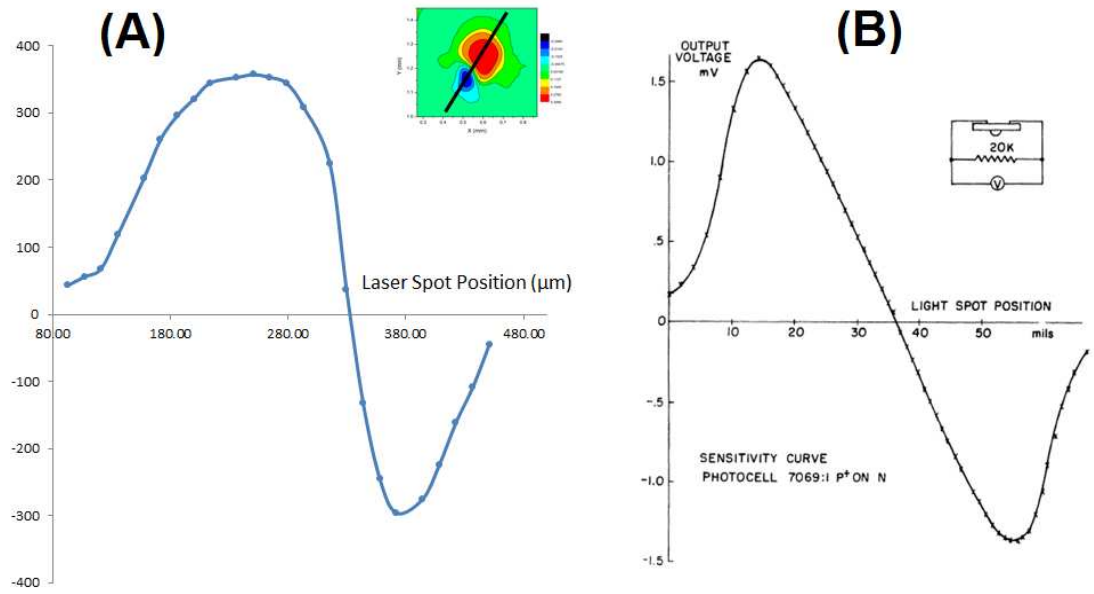

Figure 50: (A) Open circuit voltage as a function of beam position along line (inset: bisecting line path) (B)Previously published evidence of lateral photovoltaic effect in comparable device, Wallmark, Proc. IRE 45(4), 474-483 (1957)

6 Optimization of Shunt and Lead Location in Extraordinary Electroconductance (EEC) Sensors

6.1 Abstract

We report the enhanced light responsivity of extraordinary electroconductance (EEC) sensors via modification of the shunt geometry, as well as an observed bifurcation in sensor response to direct reverse bias and light irradiance based on measurement lead location. Significantly increased light responsivity was achieved by directly biasing the EEC shunt while exposing to light, resulting in an over 614% increase in resistance from 11mW/cm^2 irradiance of HeNe laser light and a maximum specific detectivity of $D^* = 3.67 \times 10^{11}$ cm$\sqrt{\text{Hz}}$/W.

6.2 Introduction

The electrical transport properties of any solid state sensor are determined by the intrinsic physical and extrinsic geometric properties of the device. While many device optimization schemes focus on enhancing the physical contributions, such as carrier mobility, impurities, doping, etc., Solin, et al. [5], have established a class of sensor that employs a geometrically enhanced response. These sensors collectively exhibit phenomena which have been given the designation EXX, where E = extraordinary and, to date, XX = magnetoresistance (EMR) [5], piezoconductance (EPC) [6], optoconductance (EOC) [7], inverse-optoconductance (i-EOC) [9] and electroconductance (EEC) [10].

The results reported here explore the geometric optimization of room-temperature EEC device responsivity to applied bias and light exposure by exploring contact geometry and location. The EEC device structure resembles that of a MESFET, but the measurement technique and operation distinguish the EEC device significantly; the EEC device employs a four-point resistance measurement as opposed to a two-point source-drain measurement and is

operated under both forward and reverse bias. Under direct forward bias, the device distinguishes itself from a traditional FET by allowing current to be injected from the gate, hereafter referred to as shunt, into the GaAs.

Previous work has shown that EEC device responsivity is dependent on shunt size [10]. In this work, we present a comparison of two different shunt geometries, a stripe shunt and a traditional square shunt with tab, both with equivalent effective shunt area. Shunt geometry was chosen to emphasize the difference in current pathways, with the square shunt acting as a corner connected island and the stripe shunt as a bisecting channel. The stripe shunt device realizes a 2.32 times greater photoresponsivity under 17.7mW/cm^2 of HeNe laser irradiance as compared to the square shunt, measured under the previously published lead geometry, establishing enhanced responsivity through geometric optimization of the shunt design.

Previous work has also shown that nonuniform illumination of EEC devices induces local photovoltages, both lateral and transverse to the Schottky interface and influenced by lead location [14]. This result motivated an investigation into the geometric influence of lead orientation in the responsivity of EEC devices to direct biasing and uniform optical illumination. The result was an observed polarity of EEC sensor response, dependent on lead orientation and magnified for different shunt geometries. The device response under direct forward bias was qualitatively insensitive to lead arrangement but under direct reverse biasing, the four-point resistance was seen to bifurcate based on lead geometry; under one lead arrangement dropping to a negligible value while under a rotated lead arrangement, tending towards infinite resistance. This lead arrangement driven polarized response was also observed in the sensor response to light exposure, with one lead arrangement leading to a drop in resistance as a function of irradiance, while the rotated lead arrangement measured an increase in resistance as a function of

irradiance. This further establishes that the sensor response is geometrically driven, dependent on lead location and enhanced by shunt geometry.

6.3 Experimental Methods

The EEC devices were fabricated using an epitaxial wafer grown by molecular beam epitaxy and purchased from IQE Inc. The active region of the device is a 200nm thick, Si-doped (N_D=4x10^{17} cm^{-3}) GaAs epitaxial layer (R_s =840.90 Ω/square) followed by an undoped 800nm thick epitaxially grown GaAs layer for electrical insulation with a semi-insulating GaAs substrate (thickness t=350μm) at the bottom to lend structural robustness.

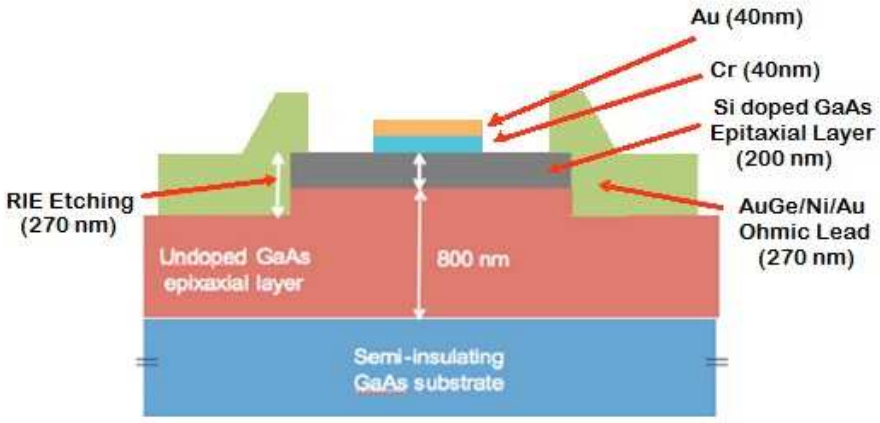

Figure 51: A Side View Schematic of EEC Device

The 200nm nGaAs layer was patterned using electron beam resist then, etched in an Oxford Plasma 100 ICP-Reactive Ion, etcher using published BCl_3 chemistry [26] to form a square nGaAs epitaxial mesa with an edgelength of 5μm. Following the formation of the mesa, Ohmic contacts were patterned using photoresist and formed using established AuGe/Ni/Au tri-stack procedures [28], including an 80 sec. anneal at 450°C in an N_2 rich environment. The final step in device fabrication was the electron beam resist patterning of the shunt followed by thermal deposition of a metal stack of Cr/Au with thicknesses 40nm/40nm, respectively. Figure 52 shows a side-view schematic of the EEC device stack.

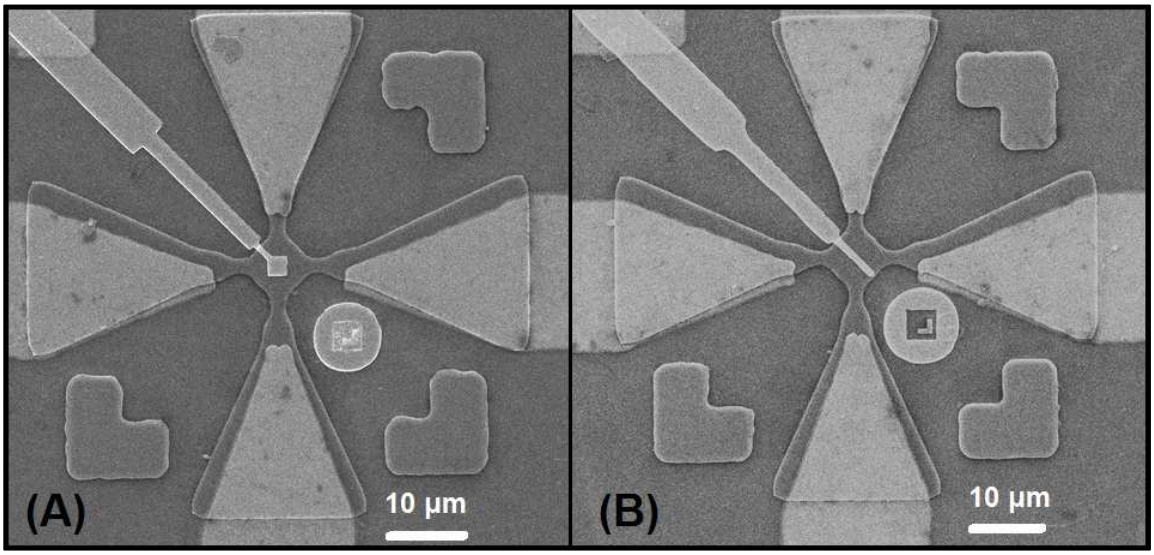

Figure 52: A SEM Image of (A) square shunt (B) stripe shunt EEC Devices

The final devices were square-shaped mesas with an epitaxial fan-out at the corners, forming Ohmic contacts on the four perimeter fans with a AuGe/Ni/Au stack. The fan-out design was favored as a means to increase contact surface area, thereby reducing contact resistance. The two shunts shapes each covered an effective area of 7.3 μm^2 on the nGaAs and all contacts were electronically accessible via contact pads along the perimeter of the chip. Figure 52(A)-(B) shows a SEM image of the square and stripe shunt EEC devices.

The device contacts were first characterized, confirming Ohmic character around the perimeter of the mesa as well as Schottky character between the shunt and mesa. This was followed by a series of experiments probing the influence of shunt geometry and lead orientation on the sensor responsivity, where the sensor responsivity is found by measuring the sensor's four-point resistance. The two four-point resistance measurement lead arrangements for the stripe shunt device are shown in Figure 53, where lead arrangement 1 (LA 1) shown in Figure 53(A) has the current sourcing and voltage sensing on either side of the plane of symmetry created by the shunt and lead arrangement 2 (LA 2) shown in Figure 53(B) has the voltage and

current leads split by the shunt. The square shunt lead arrangements are identical to those shown in Figure 53, with the connecting tab oriented to the top left.

6.4 Direct Biasing

The four-point resistance of the EEC devices for both shunt shapes and lead arrangements was measured while directly biasing the shunt in an electromagnetically isolated, light-tight box. The direct biasing was performed using a Keithley 230 Voltage Source to supply a voltage across the shunt and grounded through the current low lead. The four-point resistance of the EEC Device was measured while under direct bias, as shown in Figure 54, using a Keithley 2182a/6221 Nanovoltmeter/Current Source set in Delta Mode [33]. In Delta Mode, a square wave is current sourced and the peak and trough voltage sensed. The calculated resistance is then averaged as a means of removing thermal voltages and any other systematic

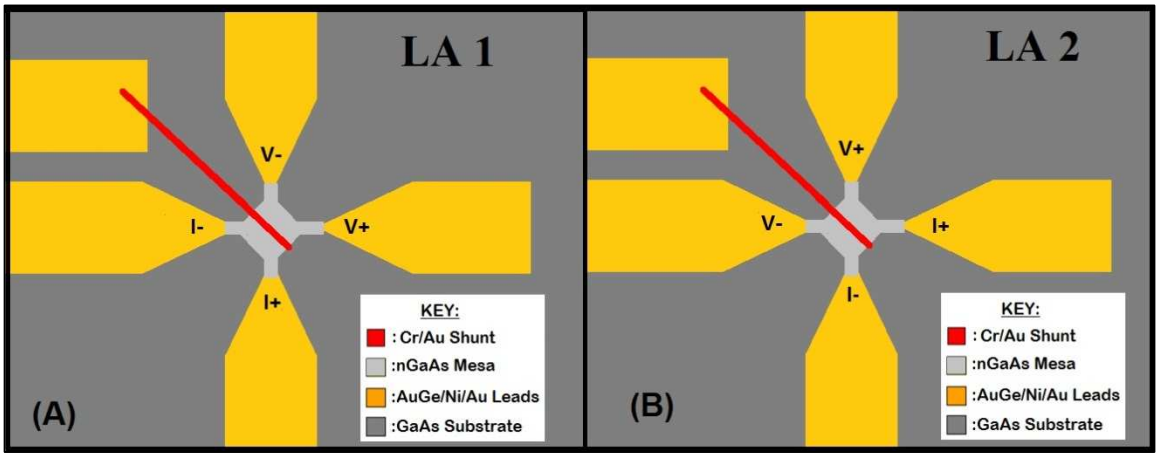

Figure 53: (A) Lead Arrangement 1, LA 1 (B) Lead Arrangement 2, LA 2.

offsets. The sourced current was +/- 50nA.

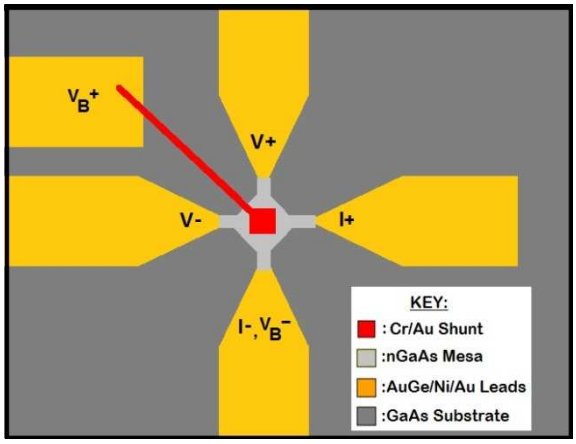

Figure 54: A schematic of four-point resistance measurement of EEC device under direct biasing for LA 2.

6.5 Photoresistance

The EEC devices were exposed to uniform optical illumination from a HeNe Laser (λ = 632.8nm) and the four-point resistance of both shunt shapes under both lead arrangements was measured as a function of beam irradiance. The beam waist of the laser was expanded to w=1mm using a 20X microscope objective to ensure uniform illumination between devices and the power of the beam quantitatively controlled using neutral density filters. The four-point resistance of each EEC device was measured as a function of beam irradiance using a Keithly 2182a/6221 Nanovoltmeter/Current Source set in Delta Mode, with the Delta Mode as previously described and a source current of +/- 100nA. The relative photoresistance, δR, was then calculated as the percent change in resistance as compared to the non-illuminated four point resistance, i.e.

$$\delta R(E_e) = \frac{R(E_e) - R(0)}{R(0)} \times 100\%, \tag{96}$$

where E_e is the irradiance, given in W/cm^2.

6.6 Relative Photoresistance under Direct Bias

The EEC devices were exposed to uniform optical illumination while under direct bias, the conditions for both as previously described. The four-point resistance was measured as a function of beam irradiance under various biases for the two shunt shapes under both lead configurations and the relative photoresistance calculated.

6.7 Results

6.8 Device Characterization

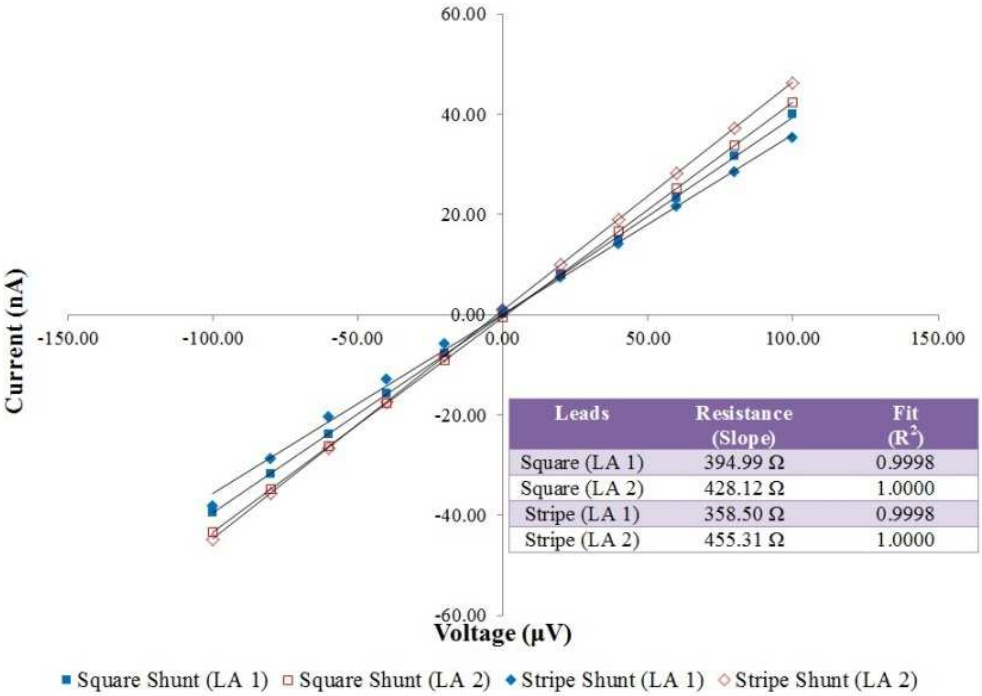

Leads	Resistance (Slope)	Fit (R^2)
Square (LA 1)	394.99 Ω	0.9998
Square (LA 2)	428.12 Ω	1.0000
Stripe (LA 1)	358.50 Ω	0.9998
Stripe (LA 2)	455.31 Ω	1.0000

Figure 55: The four-point IV curves both shunts under both lead arrangements, confirming Ohmic leads.

The EEC devices were characterized to confirm the formation of Ohmic and Schottky contacts. The IV curve of the four Ohmic contacts was measured and plotted for both types of shunts and under both lead arrangements, with a linear fit applied to all four sets of data. The results are shown in Figure 55. The correlation coefficients are in each case either equal to or

very close to unity, indicating that the contacts are highly Ohmic. The four-point resistance of the devices ranged between 358-456Ω, depending on shunt type and lead arrangement.

The charge carrier dynamics of the Schottky diode follow thermionic emission theory [13], with the predicted current-voltage relationship

$$I = I_s\left(e^{\frac{qV}{nk_BT}} - 1\right), \tag{97}$$

where I_s is the saturation current, q the electron charge, and n the ideality factor, defined as

$$n \equiv \frac{q}{k_BT}\frac{\partial V}{\partial(ln\ J)}, \tag{98}$$

where J is the current density. The IV characteristic of the Schottky diode was measured for both shunt types, with a current applied through the shunt and grounded through one of the

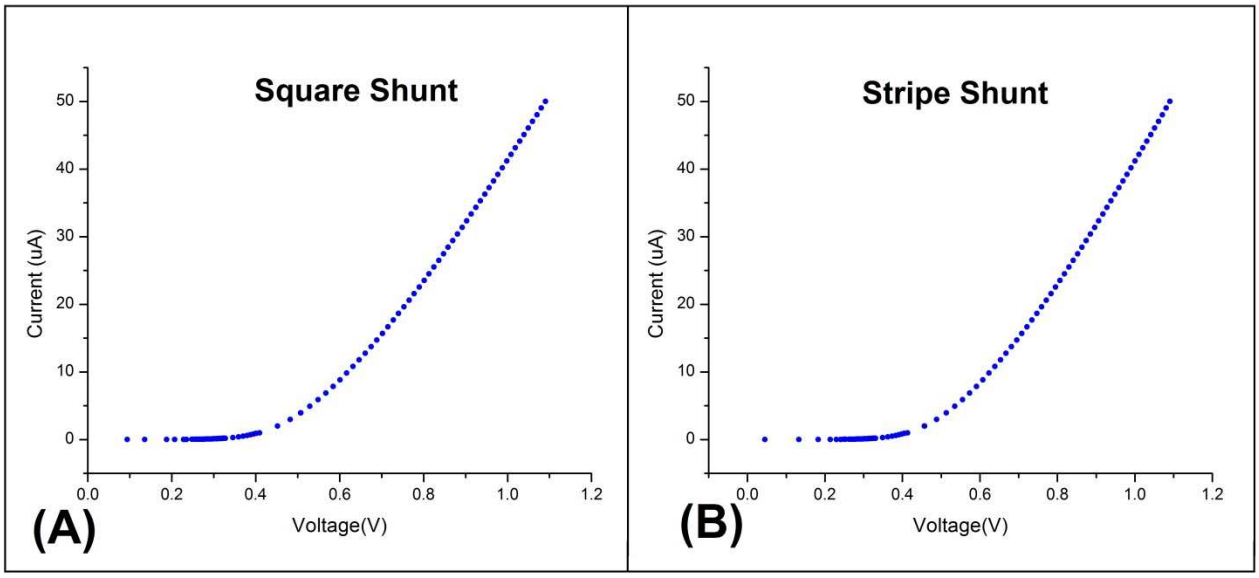

Figure 56: The Schottky IV curves for both shunt types

Ohmic leads on the device. Figure 56 shows the Schottky IV curves for both the square and stripe shunt devices.

Under low bias, the current can be modelled as having two available pathways: through either the Schottky diode or a leak channel between the shunt and current ground (Figure 57 (inset)). This leads to an IV relationship of

$$I = I_s\left(e^{\frac{qV}{nk_BT}} - 1\right) + {}^{V}/_{R_{shunt}}\ , \tag{99}$$

where R_{sh} is the resistance of the leak channel. A 3 parameter fit to Eq. (99) for the low bias data (Figure 57) finds that the leak current pathway has a resistance R_{SH}>30MΩ for both device types, indicating a negligible amount of leak current under bias. Additionally, the ideality factor was found to be n=1.41±0.03 and 1.44±0.03 for the square and stripe shunt devices, respectively. The deviation of the ideality factor from n=1 in a real Schottky interface can be attributed to

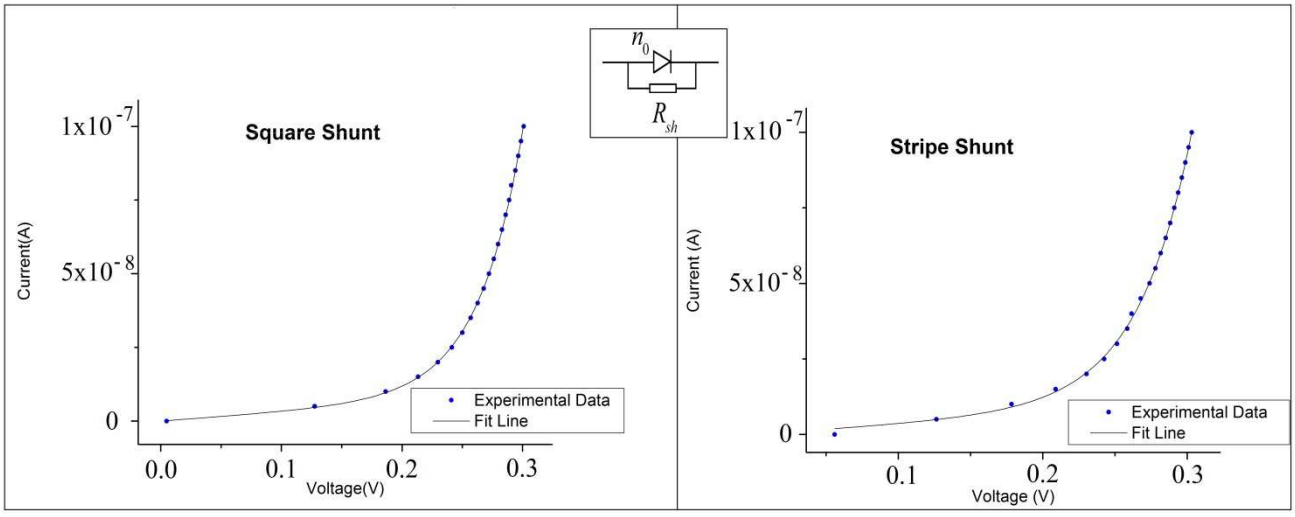

Figure 57: Low forward bias fit to Equation (4) of text. (inset) Low forward bias Schottky diode equivalent circuit.

many effects, such as electron trapping and recombination [34], barrier inhomogeneities [35], an

interfacial oxide layer [36], image force lowering [37], shunt resistance [38], and series resistance [39].

Under high forward bias, the circuit model for the current flow in the device can be approximated as a diode in series with a resistor (Figure 58(inset)), leading to an IV relationship of

$$I = I_s e^{\frac{q(V-IR_{se})}{n_o k_B T}}, \tag{100}$$

where R_{se} is the resistance of the full circuit, i.e. the sum of the measurement system resistance, contact resistance and the resistance of the nGaAs channel between the shunt and current ground

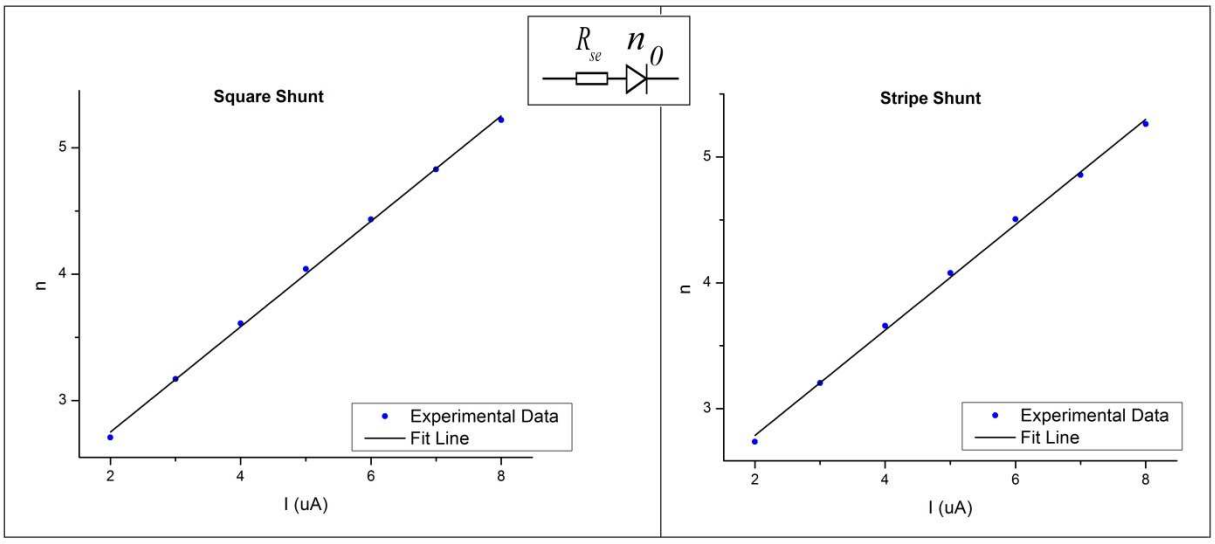

Figure 58: High forward bias ideality fit to Equation (6) of text. (inset) High forward bias Schottky diode equivalent circuit

that the current must travel through. Taking the natural logarithm of Eq. (100), differentiating by d/d ln(I) and inserting the result into Eq. (98), a linear relationship between the ideality factor and the current is formed as follows:

$$n = n_o + \left(\frac{qR_{se}}{k_B T}\right) I. \tag{101}$$

Fitting the high bias data to this linear expression (Figure 58(B)), a 2 parameter fit yields a series resistance for both devices of R_{se}= 10.9±0.2 kΩ and an ideality factor of 1.92±0.03 and 1.95±0.04 for the square and stripe shunt devices, respectively. The increased value for the

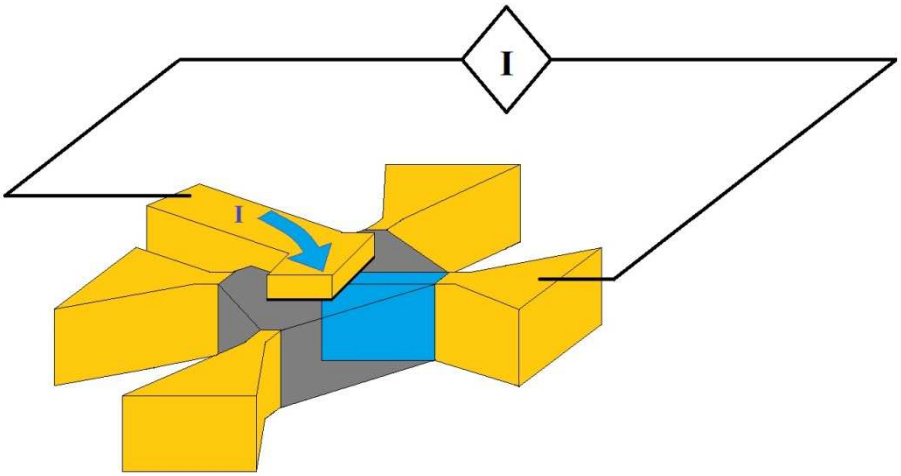

Figure 59: Modelling of current flow across the Schottky diode. The blue parallelepiped represents the current pathway through the GaAs.

ideality factor under high bias is caused by competition between the carrier drift-diffusion process and the Sah-Noyce-Schockley generation-recombination process [40]. The series resistance contribution from the resistive nGaAs channel from the shunt to the contact can be modeled as a bar-shaped channel with length, width and thickness of 10μm, 1μm and 200nm, respectively, shown schematically in Figure 59. Given the sheet resist of R_s = 835Ω/square for the epitaxial layer, this model yields a resistance of 8.4 kΩ. The resistance of the measurement system is ~1kΩ, yielding a net resistance of 9.4 kΩ, without consideration of contact resistance. This is close to the measured value, with the difference ascribable in part to the simplicity of the model.

Finally, using forward bias data, it is possible to extract the experimental barrier height [41]. The total voltage drop along the current path can be modelled as

$$V = RA_{eff}J + n\Phi_B + \frac{nk_BT}{q} ln\left(\frac{J}{A^{**}T^2}\right), \quad (102)$$

where R is the net resistance of the circuit, A_{eff} is the effective area of the Schottky interface, $n\Phi_B$ is the experimental barrier height and A** is the Richardson constant.

Defining the function

$$H(I) \equiv V - \frac{nk_BT}{q} ln\left(\frac{J}{A^{**}T^2}\right) = IR + n\Phi_B \quad (103)$$

and fitting the experimental data to the new function *H(I)* (Figure 60), a 2 parameter fit yields a barrier height of $n\Phi_B$ = 0.836eV and 0.848 eV for the square and stripe shunt device, respectively. This agrees well with the Schottky-barrier height value previously reported for Cr-GaAs [42]. Additionally, the series resistance from the slope of the fit was 10.94±0.01kΩ and

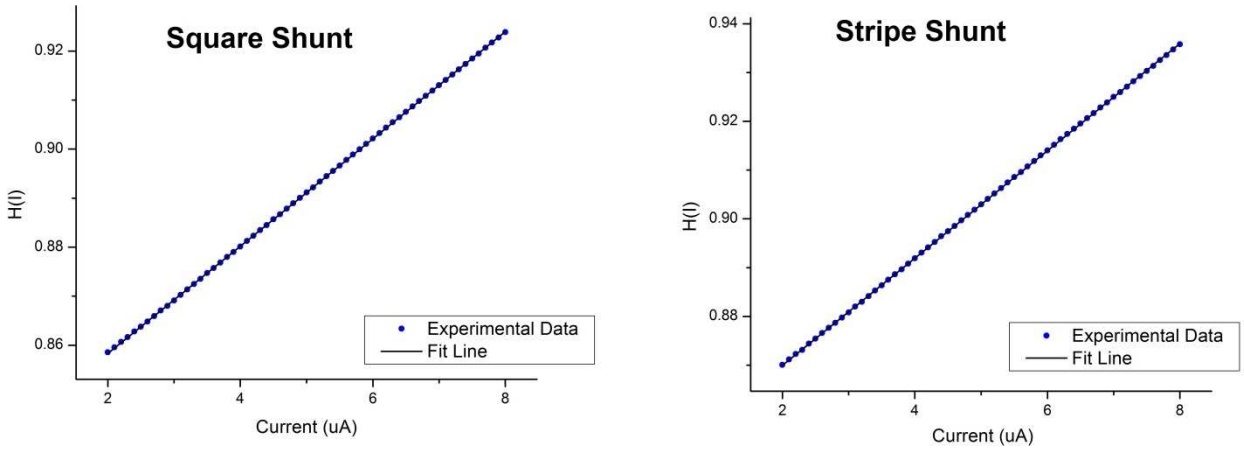

Figure 60: The barrier height fit to Equation (103) from text under high forward bias

11.00±0.01kΩ for the square and stripe shunt devices, respectively. This agrees well with the previously fit data using Equation (101) and supports the reliability of the barrier height fit value.

6.9 Direct Biasing

Figure 61 shows the four-point resistance of both the square and stripe shunt devices under direct bias as measured by LA 1 and LA 2. The four-point resistance of the devices as a function of direct forward bias is similar to that reported in previous papers for similar devices [10] [11], monotonically decreasing with increasing applied forward bias. The reverse low-bias response of the square shunt device using LA 1 is also similar to those reported in the previously cited papers [11]. This is expected, given the overlap in device design and measurement lead arrangement.

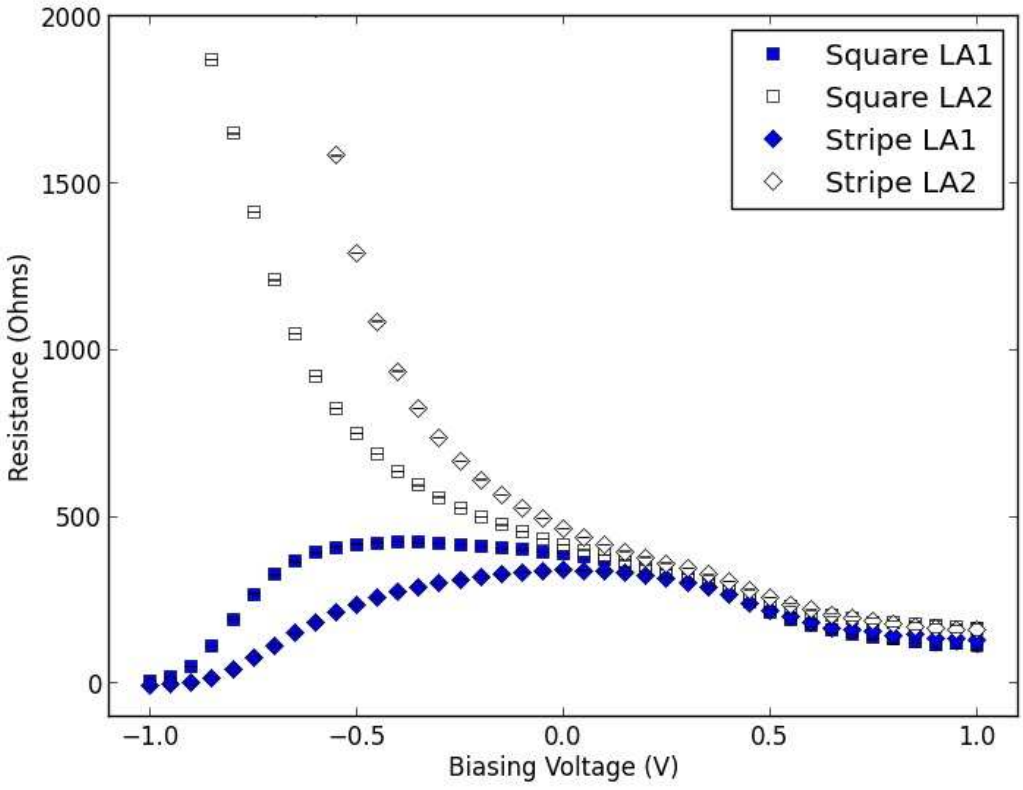

Figure 61: The four-point resistance of EEC devices under direct biasing

However, direct reverse biasing of the EEC devices produces a unique lead arrangement dependent response. Under high reverse bias (V < -0.5V), device resistance measured using LA 1 is shown to decrease with increasing reverse bias magnitude, until the measured resistance is of negligible magnitude. In stark contrast, the four-point resistance as measured under LA 2 is shown to increase for both shunt shapes under reverse bias, exhibiting a geometrically-driven response, dependent on shunt to lead orientation. This is the first time that a polarized response, driven by the geometric location of the four-point lead locations has been observed for any EXX device.

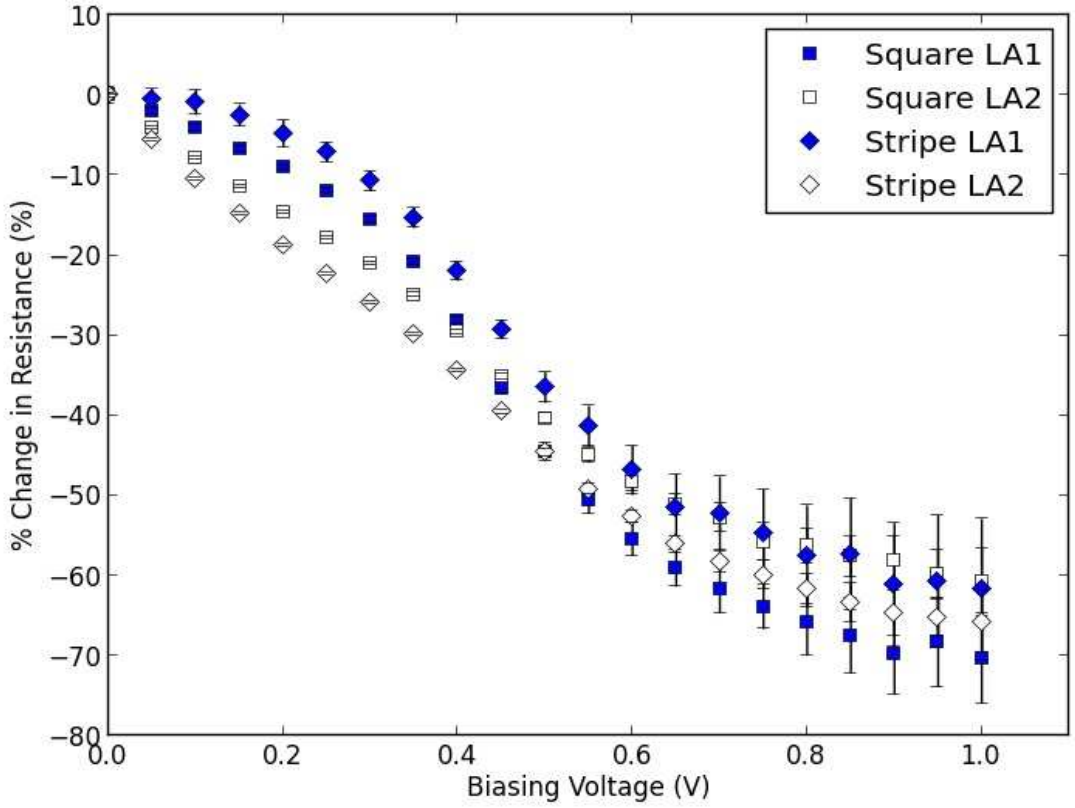

Figure 62: The % change in four-point resistance under direct forward biasing

Calculating the % Change in Resistance for each device and lead arrangement, it is possible to directly compare device performance across the various shunt shapes and lead arrangements. Figure 62 shows the % Change in Resistance of both shunts and lead arrangements under forward bias. Measured using LA 2, the stripe shunt device undergoes a larger % change in resistance for all forward biases as compared to the square shunt device. This trend is flipped for LA 1, with the square shunt device displaying a larger % change as compared to the stripe shunt device under forward bias. Comparing all four shunt and lead arrangements,

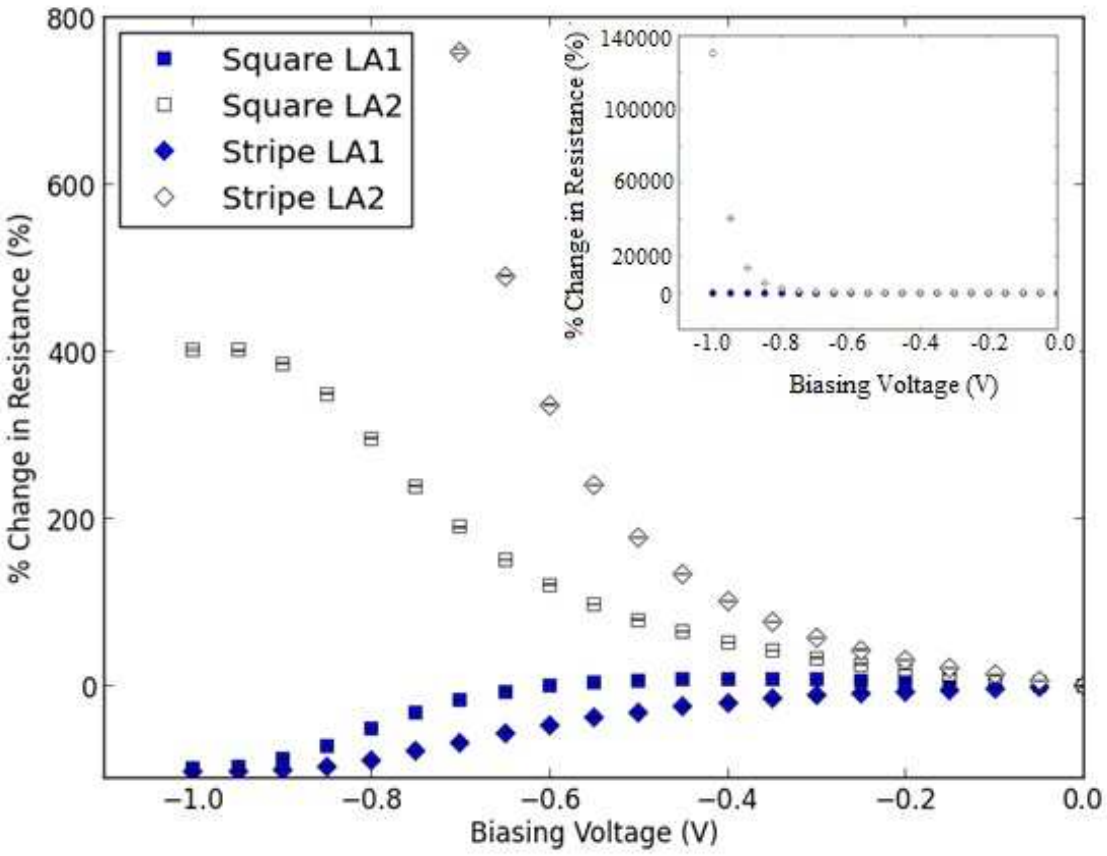

Figure 63: The % change in four-point resistance of EEC device under direct reverse biasing. (inset) Full scale highlighting magnitude of resistance change in stripe shunt under LA 2.

there exists a crossover region at V ~ 0.5 for dominant device performance. For voltages less than 0.5V, the stripe shunt device under LA 2 displays a larger percent change, while biasing

voltages great than 0.5V produce the largest percent change in the square shunt device under LA 1.

The % Change in Resistance under reverse bias (Figure 63) shows a dominant performance advantage of the stripe shunt device over the square, independent of lead arrangement. Under both lead arrangements, the stripe shunt device undergoes a larger % change in resistance than its square shaped counterpart. The sign of the percent change in resistance is lead arrangement dependent, with devices under LA 1 having a reduced resistance under high reverse bias while

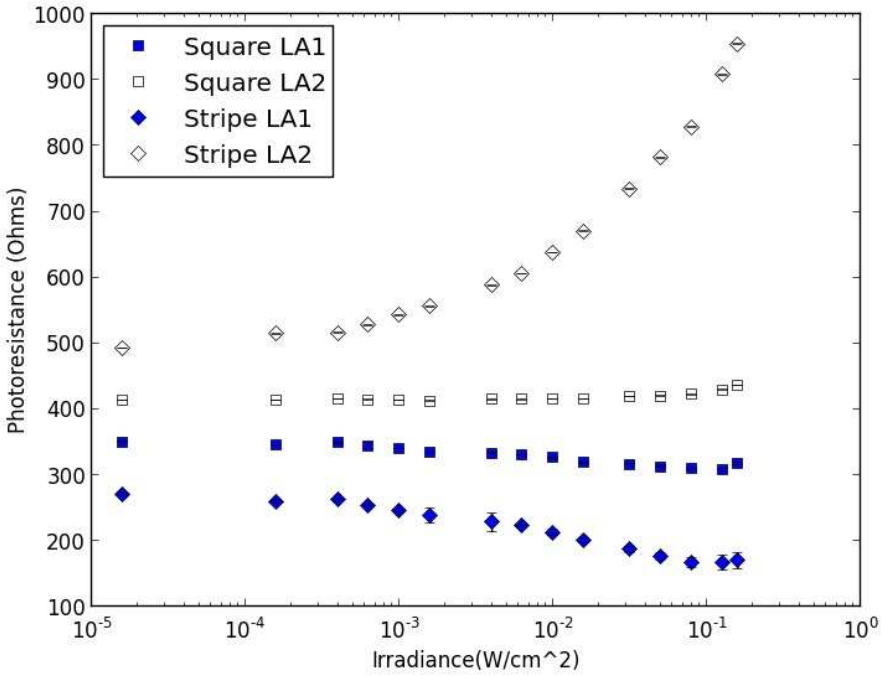

Figure 64: The photoresistance of EEC devices under irradiance of HeNe laser light ($\lambda = 632.8$nm)

devices under LA 2 have monotonically increasing resistance with increasing reverse bias.

6.10 Photoresistance

The four-point resistance of the EEC devices as a function of incident HeNe laser irradiance($\lambda = 632.8$nm) is shown in Figure 64. There is a clear lead arrangement dependent

driven response for the devices, similar to that seen under direct biasing. The four-point resistance under LA 1 for the square and stripe shunt devices is shown to decrease monotonically with increasing irradiance, confirming EEC photoresistance behavior published previously [9]. However, under rotation of the four-point resistance measurement lead arrangement (i.e. LA 2), the stripe shunt resistance is observed to monotonically increase with increasing irradiance. The four-point resistance of the square shunt device measured under LA 2 initially decreases, then increases with increasing irradiance. This polarized, lead arrangement dependent response of the device mirrors that seen in the direct reverse biasing case discussed earlier.

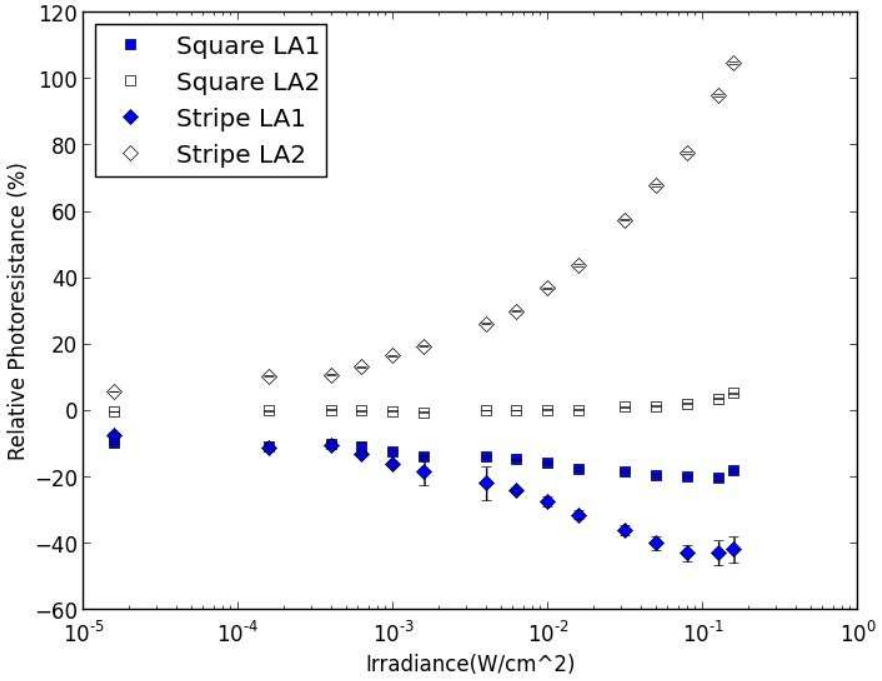

Figure 65: The relative Photoresistance of EEC devices under irradiance of HeNe laser light ($\lambda = 632.8$nm)

Calculating the relative photoresistance, δR, for each device and lead arrangement (Figure 65), the largest δR is realized under LA 2 for the stripe shunt device, which has a maximum δR that is over 1.5X larger than the δR found in LA 1 under identical light exposure

conditions. More generally, it is observed that for each lead arrangement, the stripe shunt device is shown to have a higher δR as compared to the square shunt device at equal irradiance of light exposure. This indicates that modification of the shunt shape can significantly enhance the responsivity of the sensor to light, in this case moving from a square shunt design to a stripe.

6.11 Photoresistance under Direct Bias

Direct biasing enabled a tunable responsivity of the EEC device to light exposure. The four point resistance as a function of irradiance while under direct bias for all shunt shapes and lead arrangements is shown in Figure 66 for biasing voltages ranging from -0.6 to 1.0V. Combining light exposure with direct biasing was also observed to have a deleterious effect on the signal to noise ratio (SNR) under LA 1, obfuscating any discernable trend in the data and will

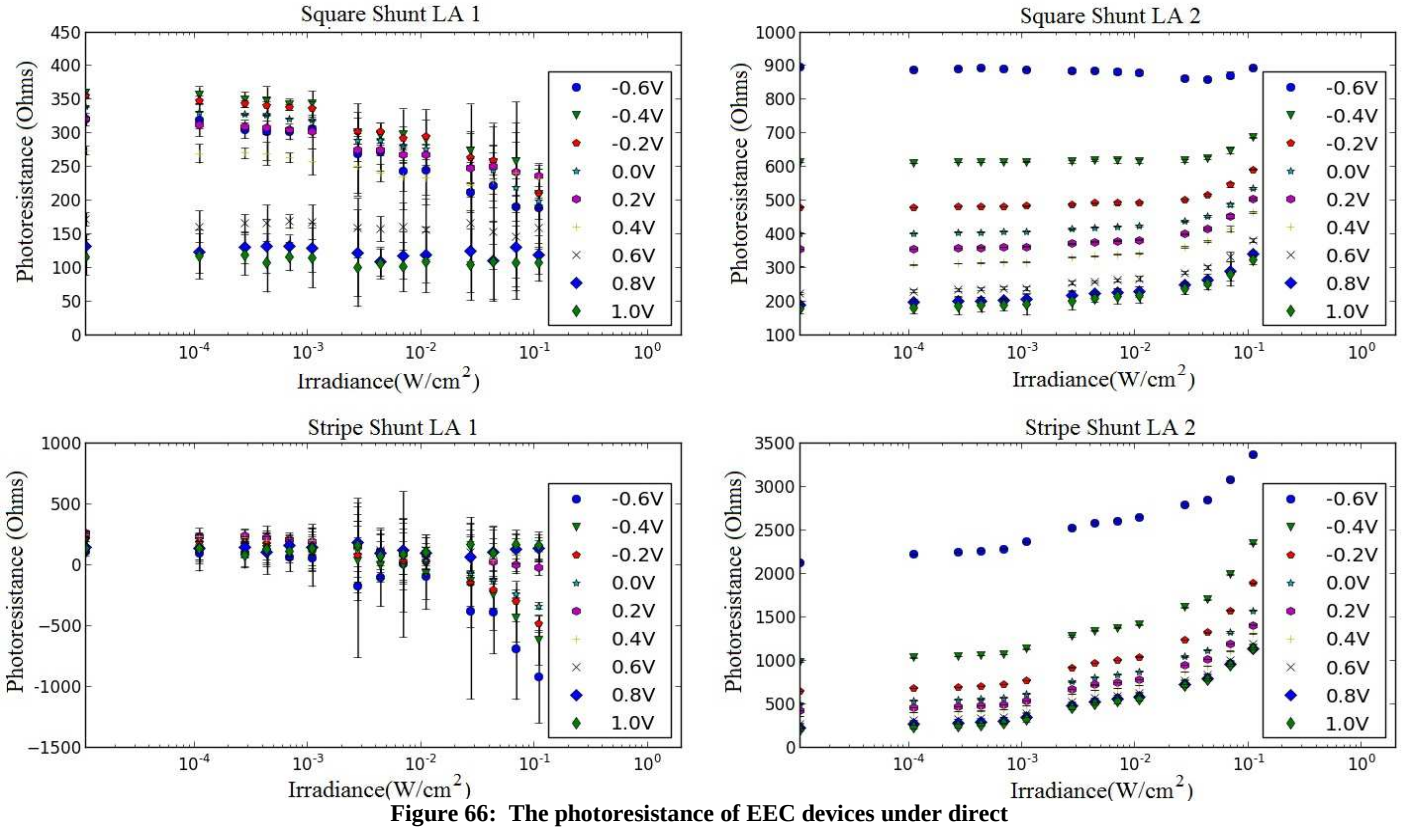

Figure 66: The photoresistance of EEC devices under direct bias.

therefore not be discussed in this section, though the origins of the noise will be discussed in detail under the "Discussion" section. The SNR is defined here as SNR = R/ΔR, where R is the average measured resistance and ΔR the root mean square error.

The resistance for all shunts and lead arrangements decreases uniformly as the biasing voltage is increased. The square shunt device resistance measured using LA 1 is shown to decrease with increasing irradiance, qualitatively consistent with the previously discussed photoresistance data. Measured using LA 2, the resistance of the square shunt device exhibits a crossover in behavior with increasing bias voltage. Under high reverse bias (V = -0.6V), increasing irradiance decreases the resistance of the device. At biases above -0.6V, the square shunt device shows increased resistance under increased irradiance. The stripe shunt device

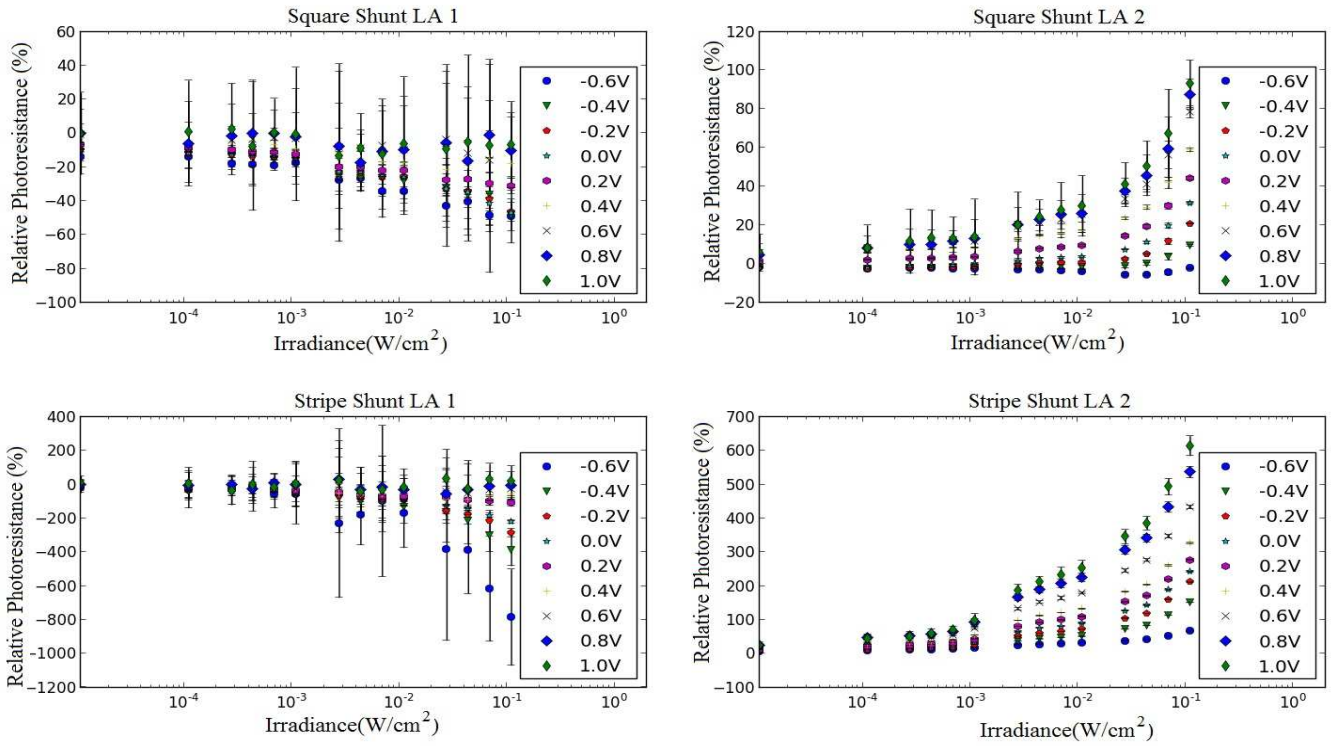

Figure 67: Relative photoresistance of EEC devices under direct bias.

measured using LA 2 displays an increase in resistance for all biases under increased irradiance.

The relative photoresistance for all shunt and lead arrangements is shown in Figure 67. Measured using LA 1, a reverse bias is seen to enhance the sensitivity of the square shunt EEC device to incident irradiance. In contrast, measured using LA 2, a forward bias enhances the sensitivity of both the stripe and square shunt devices, with the stripe shunt device having $\delta R > 600\%$ at maximum illumination. It is also worth noting that the standard deviation (or error) of the four-point resistance measurement increases with increasing forward bias, independent of irradiance.

6.12 Discussion

6.13 Direct Biasing

6.13.1.1 *Reverse Bias:*

The four-point resistance of the EEC devices under reverse bias is observed to bifurcate based on measurement lead arrangement. Since the EEC device favors a four-point resistance measurement, the lead arrangement is inherently two-dimensional, in contrast to the traditional FET that may be modelled as one-dimensional lead arrangement given the inherent linearity of the contacts. The symmetry plane of the EEC device leads to two different modes of operation. Measured under LA 2, the EEC device operation resembles that of a MESFET, with current sourcing and voltage sensing occurring across the depletion region. The EEC device operation under LA 1 has no FET analogue, since current is driven parallel to the biasing gate and voltage is sensed in parallel as well, but on the opposing side.

The four-point resistance of the square shunt device under LA 1 increases at low reverse bias, i.e. $-0.5 < V_B < 0$ before precipitously decreasing under biases $V_B < -0.5V$, while the stripe shunt device's four-point resistance under LA 1 shows a steady decline in resistance under

all reverse biasing voltages. The stripe shunt device geometry differs from that of the square shunt device in that the shunt extends across the entire device, effectively splitting the device, while the square shunt acts as a tab-connected island. The increase of resistance in the square shunt is due to the increase of the depletion region depth and the available pathway through the semiconductor being reduced, increasing the resistance as reported previously [11]. The decrease in resistance occurs when the extent of the depletion region in the device is great enough to isolate the voltage sensing leads from the current sourcing. The isolation of the two sides of the device creates an equipotential surface on the voltage sensing side of the device, making the sensed voltage insensitive to the sourced current.

As already noted, the four-point resistance of the EEC devices measured using LA 2 may be understood using MESFET analysis. The current is being forced across the depletion region and the voltage sensing arrangement is similar to the two-point resistance traditionally used in FETs, with the four-point resistance measurement removing any contact resistance. The increase in measured resistance is due to an increase in the depletion width with increasing reverse bias, approaching a pinch-off voltage. The resistance of the square shunt device is seen to level off under high reverse bias, as an alternative current pathway through the semiconductor exists that is not present in the stripe shunt device.

6.13.1.2 *Forward Bias:*

The four-point resistance of all devices decreases under forward bias due to the injection of current from the Schottky diode. The EEC device purposefully omits the oxide layer between semiconductor and shunt that is traditionally included in FETs. Omitting the oxide layers permits the flow of current from the Schottky diode through the body of the device. Evidence for the increased flow of current is observed in Figure 62, with the sharp drop in the measured four-

point resistance coinciding with the 'turn on' voltage of the diode, i.e. the voltage at which the diode current grows exponentially relative to the applied voltage.

LA 2 is more sensitive to low forward biases, i.e. $V_B < 0.5V$. This is due to a higher sensitivity to the depletion width, as the modulation of the depletion width is the dominant factor for voltages less than the turn on voltage of the diode. Under biases $V_B > 0.5V$, it is unclear what lead arrangement is most sensitive due to an increase in noise, sourced from the increased diode current discussed earlier.

6.14 Photoresistance

The four-point resistance of the EEC devices to modulated irradiance exhibits the same lead-arrangement based bifurcation seen in the previously discussed direct reverse bias results. The Schottky diode I-V characteristic curve has been shown to have an increasingly Ohmic character under increasing irradiation [9]. Under illumination, the depletion region under the shunt is gradually reduced to negligible thickness. The decreasing resistance of the current pathway through the shunt in the device has significant impact on the distribution of current within an EEC device and the four-point lead arrangement favored in EEC devices again lends two different modes of operation

Under LA 1, the photoresistance is observed to decrease with increasing irradiance. Assuming the GaAs mesa has an optical absorption coefficient of 3.90 μm^{-1} at 632.8nm [20], an upper bound for the decrease in resistance due to photoabsorption can be calculated by ignoring reflection and applying Beer-Lambert's Law, $I(x) = I_0 e^{-\alpha x}$, where $I(x)$ is the transmitted irradiance, I_0 the initial intensity and α the absorption coefficient. At the maximum irradiance of 0.018 W/cm^2, the total absorbed light irradiance after travelling 200 nm into the material is 9.7 mW/cm^2. Assuming each absorbed photon generates an electron-hole pair (i.e. a quantum

efficiency of η=1), the bound electron-hole pair density generation rate is 3.10×10^{16} electron-hole pairs/cm^2-sec. Assuming only majority charge carriers contribute to the photogenerated current, this increase in charge density accounts for a $\delta R \sim -7.19\%$ at maximum illumination. The observed magnitude of relative photoresistance at maximum illumination is much larger than this, with the striped shunt device showing a relative photoresistance of -42.0%. This fact, along with the observation that the striped shunt device shows a greater drop in resistance under illumination than the square shunt device, indicates that the relative photoresistance is enhanced by the shunt.

The influence of the shunt on the relative photoresistance is even more evident under LA 2. The photoresistance as measured under LA 2 is observed to increase with increasing light irradiance. This increase in resistance is due to the resistive pathway to the shunt becoming negligible, leading to a redistribution of the electric field within the device leading to a larger measured voltage drop. While the emergence of a low resistance current pathway through the shunt reduces the resistance under LA 1, the effect increases the measured resistance under LA 2.

6.15 Photoresistance under Bias

Combining direct biasing with light exposure, it was possible to tune the EEC device's responsivity to light. The EEC device response bifurcated, with LA 1 showing an increased responsivity to light under direct reverse bias while LA 2 showed an increased responsivity under forward bias.

Using LA 2, a forward bias of 1V and irradiance of 0.11 W/cm^2 induced a relative photoresistance of 612% for the stripe shunt device, as compared to 93% for the square shunt device. This further emphasizes the higher responsivity of the stripe shunt device compared to

the square shunt device, observed previously in photoresistance measurements and direct reverse biasing. While the change in resistance due to increased irradiation was weakly dependent on applied bias, the greater relative photoresistance for higher biases was realized due to higher biases resulting in a lower initial resistance and therefore a higher percent change even for the same net change in photoresistance. The optimization in photo-responsivity is analogous to that reported for tuning the device sensitivity to an externally applied electric field [11].

Using LA 1, direct reverse biasing appears to enhance device responsivity. However, these results are obfuscated by the high noise in the devices under LA 1.

6.16 Noise

The EEC devices suffered from anomalously high noise when measuring photoresistance

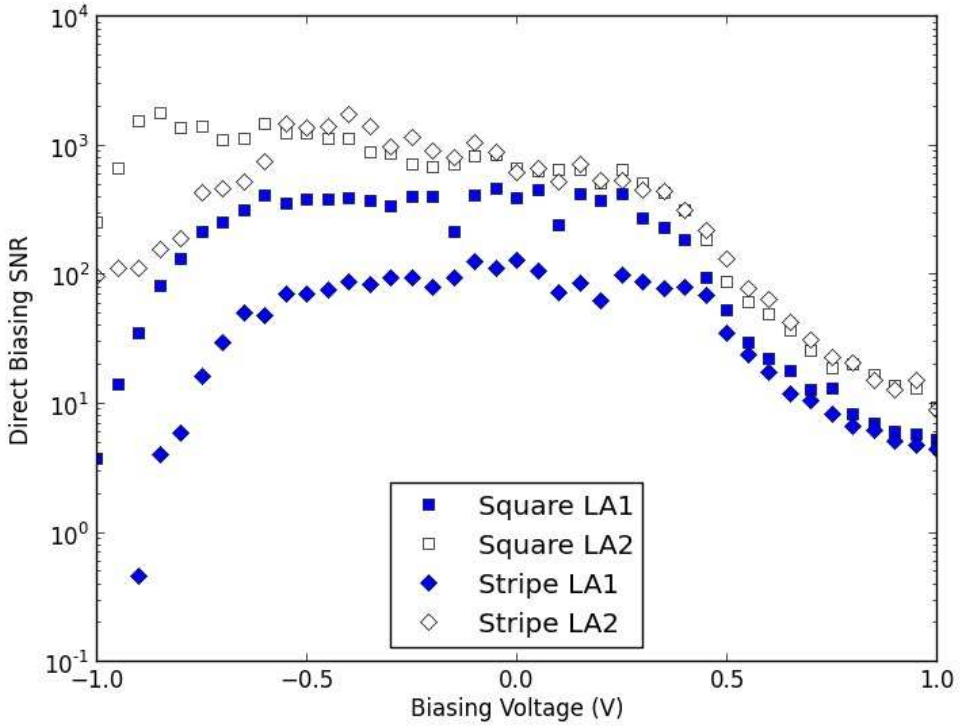

Figure 68: The EEC Signal to Noise Ratio (SNR) as a function of the direct bias voltage.

under direct bias using LA 1. In order to understand the possible origins of this noise, the noise patterns of the devices while under direct bias and the noise patterns of the devices while exposed to light were analyzed.

The SNR, $R/\Delta R$, for devices measured under LA 1 show a precipitous drop for reverse biasing at $V_B < -0.5$. This is attributable to the resistance dropping to a negligible value for both devices, leading to a very low signal value with unchanging noise levels. However, all devices are seen to suffer from an increase in noise under forward biases $V > 0.5$ (Figure 68). As discussed earlier, this is the "turn-on" voltage for the diode; for voltages $V > 0.5$, the conductive channel is flooded with current from the diode to the grounding current lead. The increase in noise paralleling the increase in current flow from the diode indicates that the noise is due to the Schottky interface.

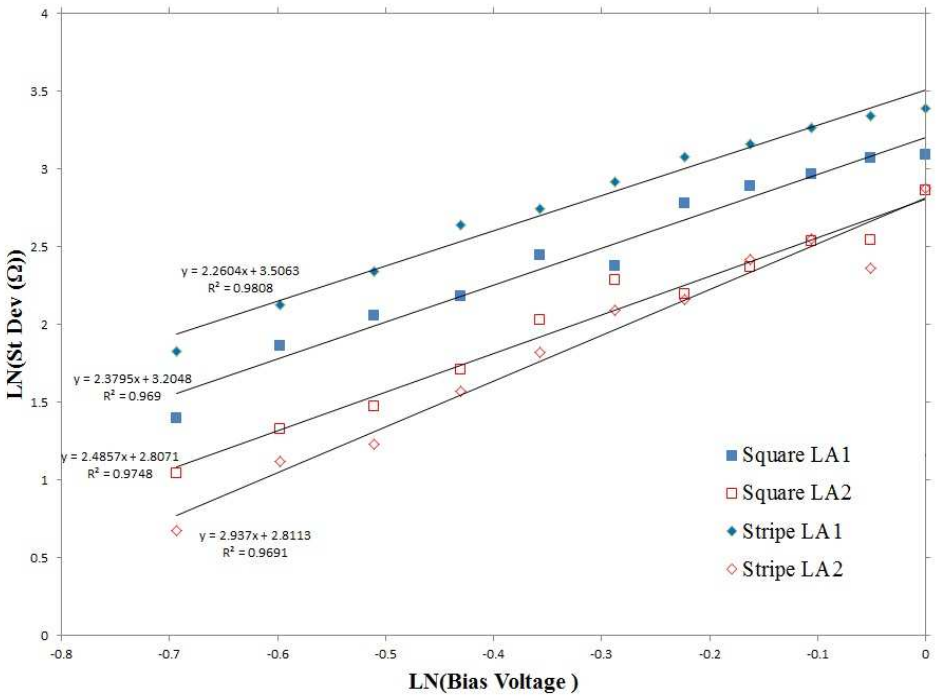

Figure 69: A Log Log plot of the Direct Forward Bias Noise

Although an analog low-frequency filter was applied during the acquisition of the four-point resistance data, the measurement method still allowed for leakage of low-frequency noise into the measurement data. Low frequency diode noise follows a current power law and is caused by generation-recombination of charge carriers [43], bulk traps, interface states, series resistance and non-uniform energy distribution [44]. The log-log plot of the standard deviation of the four-point resistance data under high forward biases (V > 0.5) shown in Figure 69 shows a clear power law relationship between the noise and forward bias, which is related to the short-circuit current in the diode and establishes that the noise is sourced from the diode current.

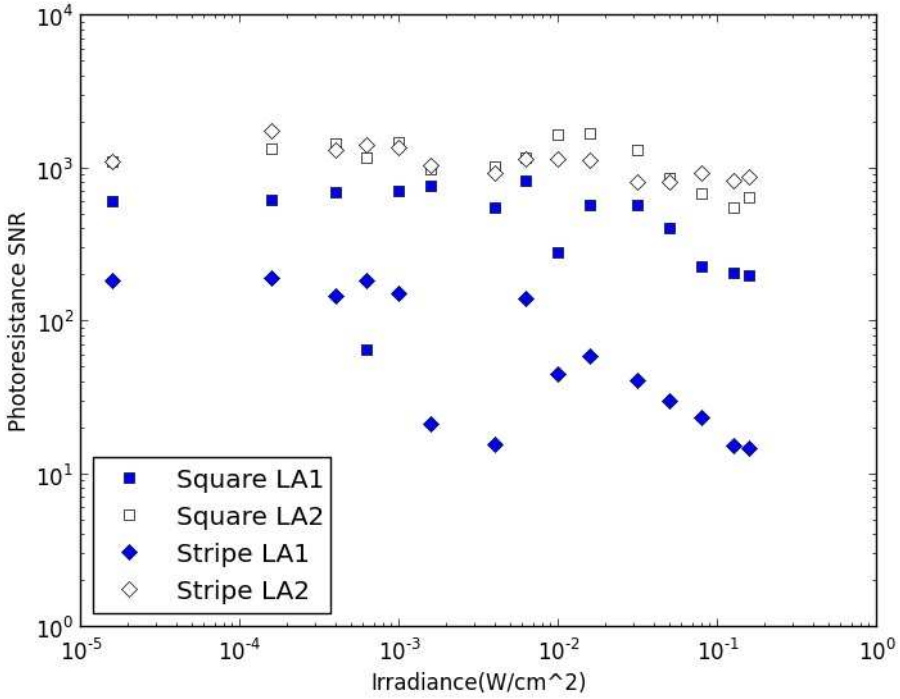

Figure 70: The dependence of the Photoresistance SNR on Irradiance

The SNR of devices exposed to light perturbation does not show a universal trend of SNR vs Irradiance (Figure 70) under LA 2. However, LA 1 is observed to have decreasing SNR with increased light irradiance. The decrease in SNR with increasing illumination may be due to

an increase of electron-hole recombination within the device, thereby producing greater generation-recombination noise, which LA 1 is more sensitive to given its parallel orientation to the shunt.

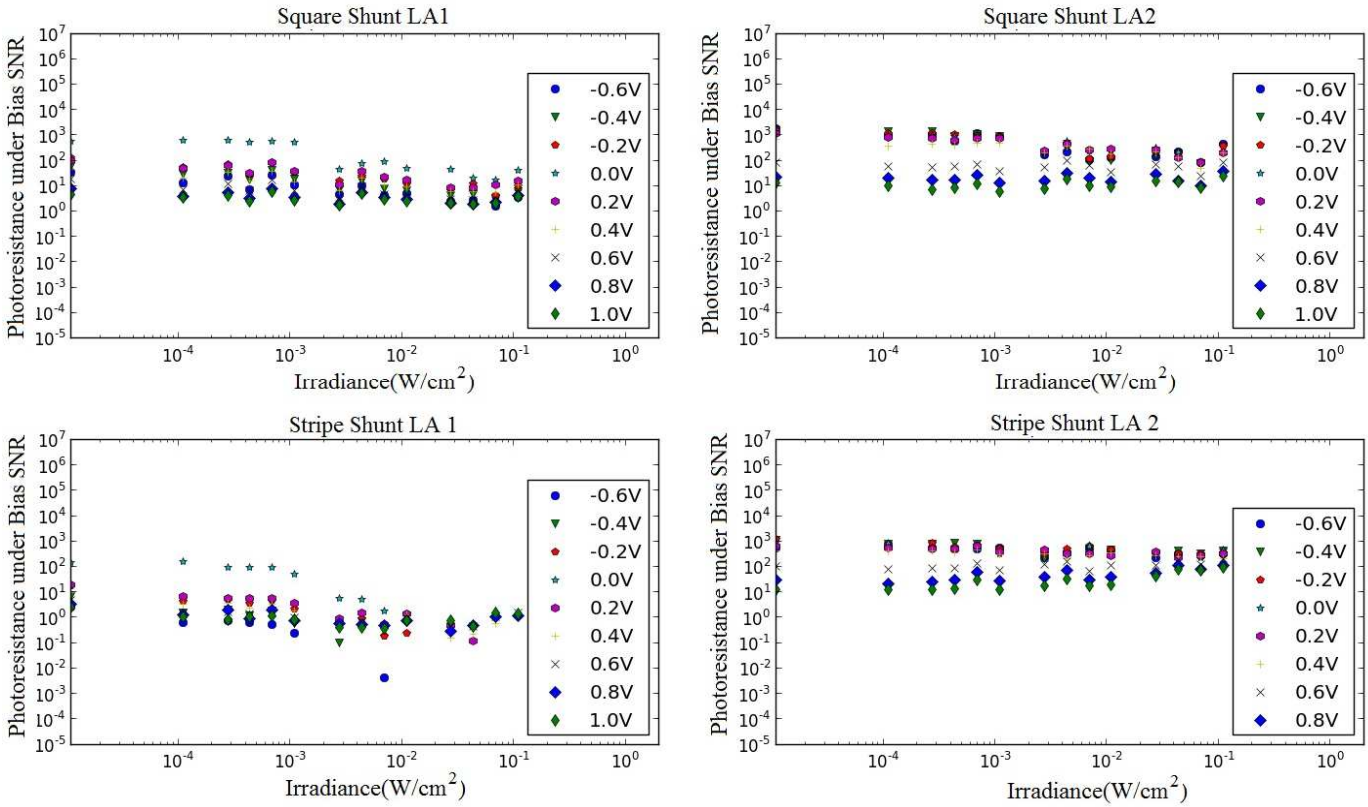

Figure 71: The photoresistance under Bias SNR

The plot of Photoresistance under Bias SNR is shown in Figure 71. Under LA 1, any applied bias leads to a reduced SNR for both shunt types. The previous discussion of noise points to increased current from the diode and generation-recombination in the channel as the source of high noise. Figure 66 shows that the measured resistance under direct reverse bias of the stripe shunt device under LA 1 was negative. These two results, high noise under bias and direct reverse bias resulting in negative resistance, point to the possible formation of high current

filaments inside of the device leading to a tortuous current path and a negative differential resistance [45].

Under LA 2, an increase in applied forward bias leads to a reduced SNR for both shunt shapes. This is understood through the earlier study of direct forward biasing noise and is attributable to the increase in noise from the diode. Since the voltage drop is measured across the conductive channel, is does not suffer from the increase of generation-recombination noise.

6.17 Concluding Remarks

We have demonstrated the geometric enhancement of EEC sensor responsivity to direct biasing and incident light irradiation by modification of the shunt and lead configuration. The use of a stripe shunt results in a greater relative photoresistance under irradiance as compared to a corner tab square shunt, establishing greater sensor responsivity based on shunt geometry.

The geometric location of the current sourcing and voltage sensing leads resulted in a bifurcation of sensor response to reverse bias and light illumination, seen most strongly with the striped shunt. The results establish the inherently three-dimensional character of the device and a previously unobserved increase in resistance in macroscopic devices with increasing light irradiance, with the relative photoresistance for the striped shunt under the split lead arrangement (LA 2) outperforming all other devices and lead arrangements.

It was found that biasing the shunt while illuminating the device enabled tunable photo-responsivity. The bias voltage that enhanced the sensor responsivity was lead arrangement dependent, with one lead arrangement favoring a direct reverse bias for enhancement and the other a direct forward bias. The presence of high noise and, for the stripe shunt device, negative resistance in the lead arrangement that favored a reverse bias obfuscated the LA 1 results and

indicated increased generation-recombination noise accompanied by the formation of high current filaments leading to a tortuous current pathway.

The device sensitivity to light exposure while under bias using LA 2 can be expressed using the specific detectivity, $D^* = {R_V\sqrt{A_D}}/{V_n}$, where R_V is the device responsivity, A_D the active area of detection and V_n the root-mean-square noise voltage per unit bandwidth [46]. The responsivity is defined as $R_V = {\Delta V}/{\Delta P}$, where ΔV is the voltage change observed under an incident power of ΔP on the active region of the device. Assuming the Johnson noise limit under LA 2, V_n can be replaced by the thermal noise voltage $V_n = \sqrt{4k_B TR}$, where k_B is Boltzmann's constant and R the device resistance [47].

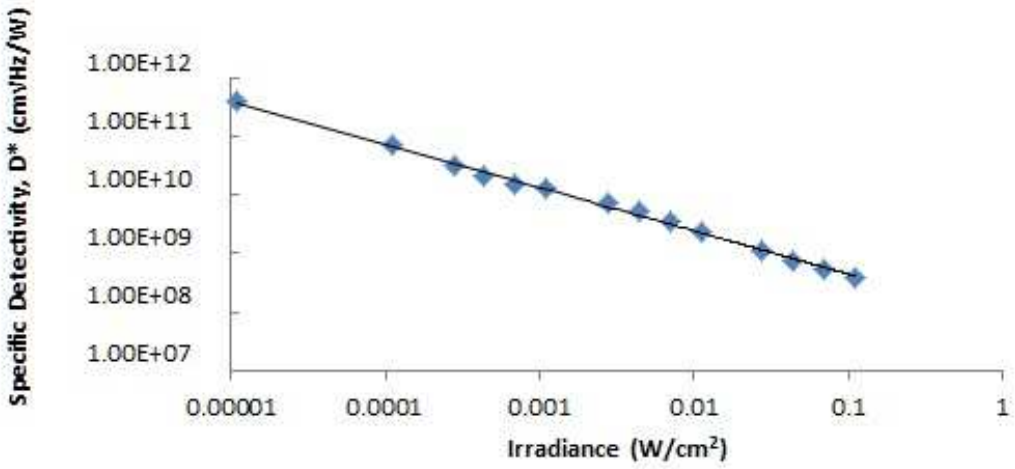

Figure 72: The Specific Detectivity of a Striped Shunt device as a function of irradiance under a bias voltage of V_B=0.8V. This behavior is representative of all applied biases. The fit line is $D^* = 8 \times 10^7 \cdot E_e^{-0.739}$ with R^2=0.9974, where D* is the detectivity and E_e the irradiation.

The stripe shunt using LA 2 was found to have a specific detectivity $D^* \sim 10^8 - 10^{11}$ cm$\sqrt{\text{Hz}}$/W depending on irradiance levels and observed to follow a power law $D^* = AV^{-\propto}$ as indicated in Figure 72. The maximum specific detectivity of $D^* = 3.95 \times 10^{11}$ cm$\sqrt{\text{Hz}}$/W

achieved under a bias of V_B=0.8V and the minimum measured irradiance of 11.1μW/cm^2. The square shunt using LA 2 was found to have a maximum specific detectivy of $D^* = 1.07 \times 10^{11}$ cm$\sqrt{\text{Hz}}$/W achieved under a bias of V_B=0.6V and the minimum measured irradiance of 11.1μW/cm^2. This is competitive with previously published D* values of other individually addressable photodetectors [48] [49].

7 Closing Statements on EEC Devices

We have presented the EEC device response to nonuniform illumination, the geometric influence of shunt shape on device responsivity and established the ability to tune the device responsivity to light intensity by applying a bias across the shunt, leading to a maximum measured relative photoresistance of >600%. The EEC device response has been shown to depend on the relative shunt and measurement lead arrangement.

The lateral photovoltaic effect [30] has been used to explain the EEC device response to nonuniform illumination. Using a traditional four-point resistance measurement, a square wave was current-sourced while simultaneously measuring voltage as a TEM_{00} laser beam was scanned across the surface of the device. One result of these measurements was an observed laser position-dependence in the offset voltage. Investigating further, a laser beam with beam waist < device dimension was scanned across the device, confirming that local photogenerated electron-hole pairs resulted in a lateral photovoltaic effect. This result opens the possibility of operating the EEC devices under a new mode, i.e. an open circuit measurement to establish position sensitive light detection using a single EEC device.

A geometric enhancement of device responsivity was achieved by modifying the traditional square shunt with tab to a symmetric striped shunt. This modification to the shunt shape realized an increased sensitivity to light exposure when measured using the traditional lead arrangement. Further, the onset of a breakdown voltage occurred earlier under direct reverse bias for the striped shunt as compared to the square. The onset of a breakdown voltage was observed by the reduction in device resistance to negligible magnitude. Under forward bias, the influence of shunt shape was mitigated at voltages greater than the diode “turn-on” voltage due to the saturation of the current channel with diode current.

Finally, a dependence on lead arrangement was observed in the device responsivity, leading to a bifurcation in device response dependent on measurement lead arrangement. For direct biasing, bifurcation is observed under direct reverse biasing. While the traditional lead arrangement ultimately led to a measured negligible device resistance, the rotated lead arrangement measured a dramatic increase in resistance under reverse bias. This bifurcation was also observed in the measured photoresistance of the devices. Applying a bias to the shunt while exposing the devices to light led to a tunable responsivity, with the striped shunt achieving a >600% increase in resistance under an applied bias while exposed to light.

More research remains to be done. It would be advantageous to measure the influence of shunt shape and lead arrangement on the device responsivity to indirect biasing, i.e. the EEC dependence of shunt geometry. While a qualitative explanation of the physics driving the bifurcated response has been made in this dissertation, a full analytical solution using finite element analysis (FEA) is required for adequate understanding. Ultimately, the goal is to use these EEC devices for the study of biologically relevant processes in cells and other materials. These enhancements of device sensitivity are aligned with that goal and lead towards an affordable point of care testing device comprised of EEC sensors capable of multiplexing complex biological signals that can aid in conclusive diagnoses.

PART II

Influence of Magnetic Disorder on Spin Glass Formation

1 Introduction to Spin Glasses

1.1 Background and Motivation

The study of magnetic systems is a fundamental, albeit challenging, topic in condensed matter physics. Magnetism as an intrinsic property of a material originates in the magnetic moments of that material, typically dominated by the electronic contribution. Intrinsic magnetic properties in a material are a result of the quantum nature of the subatomic particles and the many-body interactions within the material.

Magnetic spin glasses are a metastable magnetic phase. Similar to the structural disorder observed in metallic glasses, magnetic spin glasses contain no long range magnetic order and therefore no net magnetization. This disorder is quenched, or frozen, in space below the characteristic freezing temperature, T_F, of the system. This quenched disorder makes the spin glass theoretically challenging and has led to it being considered a model example of a complex system [50]. While the study of magnetic spin glasses has the potential to directly improve high density information storage [51], the field has a broad impact on other areas of science as well, including computer science [52], neural networks [53], protein folding [54] and more [55] [56].

The motivation of the research presented in this thesis is an investigation into the influence of tunable magnetic disorder in the formation of a spin glass, as well as the effect of the interplane interactions on the magnetic ordering of the system.

1.2 Outline of Part II

Following this introduction, Part II of this thesis is organized as follows: Section 2 will cover the origins of atomic magnetism, broadly covering electronic spin and orbit contributions to the total magnetic moment and the magnetic exchanges present in interacting electron systems that lead to spontaneous magnetic ordering. Section 3 will introduce the different types of

magnetic structure that develop in the absence of an applied magnetic field below a critical temperature, including a discussion of magnetic frustration and spin glasses. Section 4 will present research on the magnetic properties of layered antiferromagnetic quasi-triangular lattice materials with tunable magnetic disorder and reducible dimensionality, ultimately showing that, even in the absence of purposefully imposed magnetic disorder, spin glass states may still occur.

2 Origins of Atomic Magnetism

As stated in the Introduction, the origins of atomic magnetism are rooted in the quantum nature of the subatomic particles that comprise the system. The classical Hamiltonian for a system of charged particles under the influence of a magnetic field is

$$\mathcal{H} = \frac{1}{2m}\sum_{i=1}^{N}\left(\vec{p}_i - \frac{q}{c}\vec{A}\right)^2 + V, \tag{104}$$

where m, p_i and q are the mass, momentum and charge of the particle, respectively, $\vec{A}$ is the magnetic vector potential of the applied magnetic field, defined as $\vec{\nabla} \times \vec{A} = \vec{H}$ and V the background electrostatic potential. The magnetization of the system under consideration is defined as

$$M = \frac{\partial F}{\partial H}, \tag{105}$$

where F is the Helmholtz free energy, defined as $F = -k_B T \ln(z)$. The partition function, z, for this classical system of N particles is

$$\begin{aligned} z &= \sum_n e^{-E_n/k_B T} \\ &= \frac{1}{\hbar^{3N} N!}\int_{-\infty}^{\infty} d^{3N}x \int_{-\infty}^{\infty} d^{3N}p \ \exp\left(-k_B T \sum_{i=1}^{N} \frac{\left(\vec{p}_i - \frac{q}{c}\vec{A}\right)^2}{2m} + V\right) \end{aligned} \tag{106}$$

Since the limits of the integrals are $\pm\infty$, the partition function is insensitive to the $\frac{q}{c}\vec{A}$ offset in the exponential and the magnetic influence is effectively absorbed into the endpoints. Thus, the free energy has no dependence on the magnetic field and $M=0$. Thus, magnetism cannot be explained classically.

2.1 Electronic Spin and Orbit

2.2 Magnetic Moment

In most cases, the magnetic character of a material will be determined by the electrons within the structure. Therefore, the discussion of the atomic origins of magnetism will be constrained to consider those contributions from the electrons in the system. In order to understand a system of electrons, first consider the case of a single electron bound by a positively charged nucleus with charge +Z.

If the system is classical and the electron is modelled as a localized negative point charge, with charge *-e*, orbiting the positive nucleus at some distance *r* with a velocity *v*, then the system will have a magnetic moment of

$$\vec{\mu} = IS\hat{n} = -\frac{1}{2}evr\hat{n}, \tag{107}$$

where *I* is the current generated by the orbiting electron, S the surface area and $\hat{n}$ the surface vector normal to the plane of orbit. The magnetic moment can be expressed in terms of the angular momentum of the electron, defined as $L = \vec{r} \times \vec{p} = rmv$, where *m* is the mass of the electron as follows:

$$\vec{\mu} = -\frac{e}{2m}\vec{L} \tag{108}$$

Thus, the magnetic moment of a bound electron is proportional to its angular momentum. This result remains valid, up to a scaling constant, even as the analysis is extended into quantum mechanics.

Extending this result into quantum mechanics, the time-independent Schrödinger equation for an electron bound by a nucleus with charge +Z is

$$\left(-\frac{\hbar^2}{2m}\nabla^2 + V(\boldsymbol{r})\right)\psi(\boldsymbol{r}) = E\psi(\boldsymbol{r}), \tag{109}$$

where $V(\boldsymbol{r}) = -k\frac{eZ}{r}$, where k is the Coulomb constant. The bound state solution to is separable and takes the form $\psi(r,\theta,\varphi) = R_{nl}(r)Y_l^{m_l}(\theta,\varphi)$, where $R_{nl}(r)$ is the radial distribution and $Y_l^{m_l}(\theta,\varphi)$ is the angular distribution. The subscripts *n*, *l*, m_l represent the principle, angular momentum and magnetic quantum numbers, respectively, and uniquely define the bound state. The quantum numbers are integers that obey the following:

$$n = 1,2,3,\ldots$$

$$l = 0,1,2,\ldots,n-1 \tag{110}$$

$$m_l = -l,-l+1,\ldots,0,\ldots,l-1,l$$

The operators $L^2 = -\hbar^2\left[\frac{1}{sin\theta}\frac{\partial}{\partial\theta}\left(sin\theta\frac{\partial}{\partial\theta}\right) + \frac{1}{sin^2\theta}\frac{\partial^2}{\partial^2\theta}\right]$ and $L_z = \frac{\hbar}{i}\frac{\partial}{\partial\varphi}$ commute with the Hamiltonian and have associated eigenvalues

$$L^2\psi(r,\theta,\varphi) = \hbar^2 l(l+1)\psi(r,\theta,\varphi),$$
$$L_Z\psi(r,\theta,\varphi) = \hbar m_l\psi(r,\theta,\varphi) \tag{111}$$

The operator L^2 is the square of total angular momentum. Thus, the magnitude of the angular momentum for the state is

$$|\boldsymbol{L}| = \hbar\sqrt{l(l+1)} \tag{112}$$

and, applying Eq. (108), the orbital magnetic moment is

$$\mu_l = -\frac{e}{2m}\hbar\sqrt{l(l+1)} = -\mu_B\sqrt{l(l+1)}, \quad \textbf{(113)}$$

where μ_B is the Bohr magneton, defined as $\mu_B = \frac{e\hbar}{2m}$.

The operator L_Z represents the projection of the angular momentum onto the z-axis. In the absence of a magnetic field, the z-axis is arbitrarily chosen. However, the application of a magnetic field determines the system's z-axis and m_l represents different energy levels.

As discussed earlier, the electron also has an intrinsic spin that contributes to the net magnetic moment. The spin of the electron is understood to be an intrinsic property of the electron and not a manifestation of some physical spinning of the electron. The spin angular momentum follows a similar functional form as the orbital angular moment, with

$$|\boldsymbol{S}| = \hbar\sqrt{s(s+1)}, \quad \textbf{(114)}$$

where s is the spin quantum number. For electrons, s = 1/2. The spin projection on the z-axis can assume either a positive or negative value of s, leading to the introduction of a fourth quantum number, $m_s = \pm 1/2$. The spin magnetic moment that results from the spin angular momentum, with respect to the z-axis, is defined as

$$\mu_s = -g_s\frac{e}{2m}\hbar m_s = -g_s m_s \mu_B, \quad \textbf{(115)}$$

where g_s is the electron spin g-factor, with a measured value of 2.002(…) [57].

The spin and orbit angular momenta of the system determine the total angular momentum **J=L+S**, while J_z is the projection of the angular momentum on the z-axis. The total angular momentum and projection of the angular momentum on the z-axis assume the following values:

$$J = |L - S|, |L - S| + 1, \dots, L + S - 1, L + S$$
$$M_J = -J, -J + 1, \dots, 0, \dots, J - 1, J, \quad \textbf{(116)}$$

where J is the total angular momentum and M_J is the eigenvalue of J_z. Thus, the projection of the magnetic moment on the z-axis is given by

$$\mu_{m_j} = -g m_J \mu_B, \quad \textbf{(117)}$$

where g is the Lande g-factor, defined as $g = \left[1 + \frac{j(j+1) - l(l+1) + 3/4}{2j(j+1)}\right]$ [58].

2.3 Pauli Exclusion Principle and Hund's Rules

Since electrons are fermions, they obey the Pauli Exclusion Principle that no two electrons are permitted to occupy the same state. Thus, for a many-electron state, the electron states must be occupied obeying the Pauli Exclusion Principle while simultaneously achieving a minimum energy for the ground state of the system. These two requirements have significant impact on the magnetic character of the system, since the magnetic character is determined by the net angular momentum of the system, which in turn is dependent on the occupation of various spin and orbital levels in the system.

The requirement that the electrons occupy unique energy levels while simultaneously minimizing the energy of the system are satisfied by following Hund's Rules, a set of rules used to predict the ground state of a multi-electron atom. The three rules may be stated as follows:

1. The state of lowest energy will have the highest total spin angular momentum, S.
2. The state of lowest energy will have the highest total orbital angular moment, L.

3. The state of lowest energy for a system with no more than half-filled subshell (for a given *n, l*) is given by $J = |L - S|$. In the case of a more than half-filled subshell, the lowest energy for a system will have $J = L + S$.

The ground state of the valence electrons in Cu^{2+} and Zn^{2+} is given by Table 1. The predicted orbital band filling of these two ions was chosen since the body of this work focuses on materials whose magnetic properties are based on these two ions.

Table 1: Ground state configuration of valence electrons in Zn^{2+} and Cu^{2+} predicted by Hund's rules

	l_z=-2	l_z=-1	l_z=0	l_z=1	l_z=2	S	L	J
Zn^{2+}	↑↓	↑↓	↑↓	↑↓	↑↓	0	0	0
Cu^{2+}	↑	↑↓	↑↓	↑↓	↑↓	1/2	2	5/2

The Zn^{2+} ion has a full subshell and therefore no net angular momentum. This results in a non-magnetic ground state. In contrast, Cu^{2+} has a partially filled band with a predicted total angular momentum of J=5/2. This value of J does not agree with experiments, with the measured value closer to 1/2. This discrepancy is due to a quenching of the orbital angular momentum from a strong crystal field in the material that is capable of lifting the degeneracy of the total orbital momentum L-multiplet, which is unaccounted for in Hund's Law [59]. While this quenching typically removes all angular momentum, an angular momentum slightly higher than 1/2 persists in Cu^{2+} ions as a result of spin-orbit interactions.

2.4 Interacting Electrons

The magnetic character of some systems can be accurately explained by treating the electrons as non-interacting and applying Hund's Rules, specifically to those materials that have

localized electrons, i.e. insulators. However, the interaction of electrons with the ions and other electrons in the system has important consequences that lead to the magnetic ordering in certain materials. The following discussion will focus on the following interactions: exchange, super-exchange, indirect exchange, also known as the Dzyaloshinskii-Moriya Interaction(DMI), and Ruderman-Kittel-Kasuya-Yosida(RKKY) interactions.

2.5 Direct Exchange Interactions

The direct exchange interaction between electrons in a material is from Coulombic interactions and the parity under exchange. To illustrate, consider the system of two Hydrogen atoms being brought together. The full electronic eigenstate is defined as

$$\psi = \varphi(r_1, r_2) \cdot \chi(\sigma_1, \sigma_2) \tag{118}$$

such that

$$\psi(r_1, \sigma_1; r_2, \sigma_2) = -\psi(r_2, \sigma_1; r_1, \sigma_2), \tag{119}$$

where φ represents the spatial wave function and χ the spin state. The spin state can assume the following states:

$$\underline{\text{Singlet State } (S = 0)}: \ \frac{1}{\sqrt{2}}(|\uparrow\downarrow\rangle - |\downarrow\uparrow\rangle) \tag{120}$$

$$\underline{\text{Triplet State } (S = 1)}: \ \left\{\frac{1}{\sqrt{2}}(|\uparrow\downarrow\rangle + |\downarrow\uparrow\rangle), |\uparrow\uparrow\rangle, \ |\downarrow\downarrow\rangle\right\}, \tag{121}$$

where the singlet state is odd and the triplet state is even under exchange.

The Hamiltonian for this system is

$$\mathcal{H} = \sum_{i=1}^{2} \mathcal{H}_i^{\infty} + \Delta\mathcal{H} \tag{122}$$

where $\mathcal{H}_i^{\infty}$ is the Hamiltonian when the two hydrogen atoms are infinitely separated and

$$\Delta\mathcal{H} = \frac{e^2}{|\vec{r}_2 - \vec{r}_1|} - \frac{e^2}{|\vec{r}_1 - \vec{R}_2|} - \frac{e^2}{|\vec{r}_2 - \vec{R}_1|}, \tag{123}$$

where the first term represents the electron-electron interaction and the second and third terms represent the electron-ion interaction as the two atoms are brought near one another.

The solution to the Hamiltonian is found by proposing an ansatz that is a linear combination of the radial solution to the hydrogen atom and minimizing the expectation energy using a variational approach. The result is two states, defined as

$$\varphi_{\pm} = \frac{1}{\sqrt{2}}[\varphi_1(r_1)\varphi_2(r_2) \pm \varphi_2(r_1)\varphi_1(r_2)], \tag{124}$$

with $E_+ < E_-$. Since the energy of the φ_+ state is less than that of the φ_- state, it is the favored ground state and the spatial distribution is therefore symmetric. In order to satisfy the requirement stated in Eq. (119), this forces the spin state to have odd symmetry, leading to a singlet state. The singlet state prefers an antiparallel alignment of spins, leading to antiferromagnetic order. If the φ_- state were the favored ground state, the triplet spin state would be required, favoring parallel spins and leading to ferromagnetic ordering.

The two states are therefore $\psi_+ = \frac{1}{\sqrt{2}}(|\uparrow\downarrow\rangle - |\downarrow\uparrow\rangle)\varphi_+$ with S=0 and $\psi_- = \frac{1}{\sqrt{2}}(|\uparrow\downarrow\rangle + |\downarrow\uparrow\rangle)\varphi_-$ with S=1. The expectation value of $\vec{s}_1 \cdot \vec{s}_2$ is $\langle S = 0|\vec{s}_1 \cdot \vec{s}_2|S = 0\rangle = -3/4$ and $\langle S = 1|\vec{s}_1 \cdot \vec{s}_2|S = 1\rangle = 1/4$, respectively. We can simplify the Hamiltonian in Eq. (123) by

defining an exchange interaction, $J(\vec{s}_1 \cdot \vec{s}_2)$, and letting $J = \Delta E$, define an equivalent spin Hamiltonian as

$$\mathcal{H}_{spin} = -J(\vec{s}_1 \cdot \vec{s}_2) \quad \textbf{(125)}$$

If J>0, a state with parallel, or ferromagnetic, spins is favored, while J<0 favors a state with antiparrellel, or antiferromagnetic spins. It is important to note that, while the exchange can be represented as spins, the value of J in this example was determined by the Coulombic interaction and is not magnetically driven.

More generally, the spin Hamiltonian for a system of spins is defined as

$$\mathcal{H}_{Heisenberg} = -\sum J_{ij}(\vec{s}_i \cdot \vec{s}_j), \quad \textbf{(126)}$$

where only the nearest neighbor spin interactions are considered. This spin Hamiltonian is the Heisenberg Hamiltonian [12] and is used extensively in modelling magnetic systems.

2.6 Superexchange Interactions

Superexchange interactions are distinguished from the previously discussed direct exchange interactions in that they are exchanges between next-nearest neighbors, with a non-magnetic ion mediating the exchange. The superexchange interaction was first proposed by Hendrik Kramers in 1934 in order to account for the magnetic behavior observed in MnO crystals [60]. Using MnO as an example, the Mn^{2+} ions in the system have half-filled energy bands and, by Hund's rule, the valence electrons all have parallel spins. By contrast, the O^{2-} ions have fully occupied valence bands. In order to lower their energy, the O^{2-} valence electrons spread into the two neighboring Mn^{2+} ions. If the two Mn^{2+} ions have their spins parallel to one another, then by the Pauli Exclusion Principle, the O^{2-} valence electron is forbidden from

spreading. Therefore, the energetically favorable arrangement of spins is that the next-nearest Mn^{2+} electrons have antiparallel spins, leading to an antiferromagnetic ordering. If the next-nearest neighbors are connected by 90° degrees to the intermediate nonmagnetic ion, the exchange becomes ferromagnetic.

The set of semi-empirical rules that govern the superexchange interaction is referred to as the Goodenough-Kanamori rules, namely that the superexchange interaction is sensitive to bond angle among the three ions. For magnetic ions connected to the intermediate, nonmagnetic ion by 180° degree, the exchange is strongly antiferromagnetic. However, for 90° angles, the exchange is strongly ferromagnetic.

2.7 Indirect Exchange/Dzyaloshinskii-Moriya Interaction (DMI)

Indirect exchange, also known as DMI, is an anisotropic exchange interaction that arises from a mixture of superexchange and spin orbit coupling. The interaction takes the form of the Hamiltonian

$$\mathcal{H}_{DMI} = -\boldsymbol{D_{ij}} \cdot \left(\vec{\boldsymbol{S}}_{\boldsymbol{i}} \times \vec{\boldsymbol{S}}_{\boldsymbol{j}}\right) \quad \textbf{(127)}$$

where $\boldsymbol{D}_{ij}$ is a tensor that depends on the matrix elements of the electrons' orbital angular momenta. The effect of DMI is a canting of nearly antiparallel spins. This canting results in a small, non-negligible net magnetic moment for the system [61].

2.8 Ruderman-Kittel-Kasuya-Yosida (RKKY) Interaction

The RKKY interaction is an indirect exchange interaction between two locals spins, mediated by the spin polarization of conduction electrons. The sign of the interaction fluctuates from negative to positive throughout space, with the exchange interaction taking the form

$$J(\boldsymbol{R}) = J_0 \frac{\cos(2k_F R + \varphi_0)}{(k_F R)^3}, \boldsymbol{R} \to \infty, \quad \textbf{(128)}$$

where J_0 and φ_0 are constants and k_F the Fermi-wave number of the host material [62]. This modulation of exchange interaction is used in some models to account for giant magnetoresistance [63]. In the context of the work presented here, the RKKY interaction leads to a specific class of spin glasses, referred to as RKKY glasses. The modulated interaction and random location of spins in a classical spin glass material leads to spins favoring parallel, or ferromagnetic, alignment, relative to one interaction and antiparallel, or antiferromagnetic, alignment relative to another interaction, leading to a condition where the bonds cannot be simultaneously satisfied. This condition, known as frustration, can lead to a spin glass phase, where the spins are randomly aligned and frozen throughout the material below a critical temperature.

3 Types of Magnetic Structure

Magnetic interactions lead to the onset of magnetic ordering (or frozen disorder) below a transition temperature. While there are many material responses to an imposed applied magnetic field, including paramagnetism and diamagnetism, this section will discuss three types of magnetic structure that develop in the absence of an applied magnetic field: ferromagnetic, antiferromagnetic (and ferrimagnetic) and spin glass, shown schematically in Figure 73.

The onset of magnetic ordering, or the emergence of collective magnetic behavior, may be observed via the magnetic susceptibility. The magnetic susceptibility is defined as the ratio of a material's magnetization, M, as a response to an imposed magnetic field, expressed as

$$\chi = {}^{M}/_{H} \tag{129}$$

3.1 Ferromagnetism and Antiferromagnetism

The critical temperature, T_c, that marks the onset of spontaneous magnetization in a material is referred to as the *Curie temperature* in ferromagnets and the *Néel temperature* in antiferromagnets (AFs). The observed magnetization just below T_c is well described by the power law

$$M \sim (T - T_c)^{\beta}, \tag{130}$$

where β is typically between 0.33 and 0.37 [12].

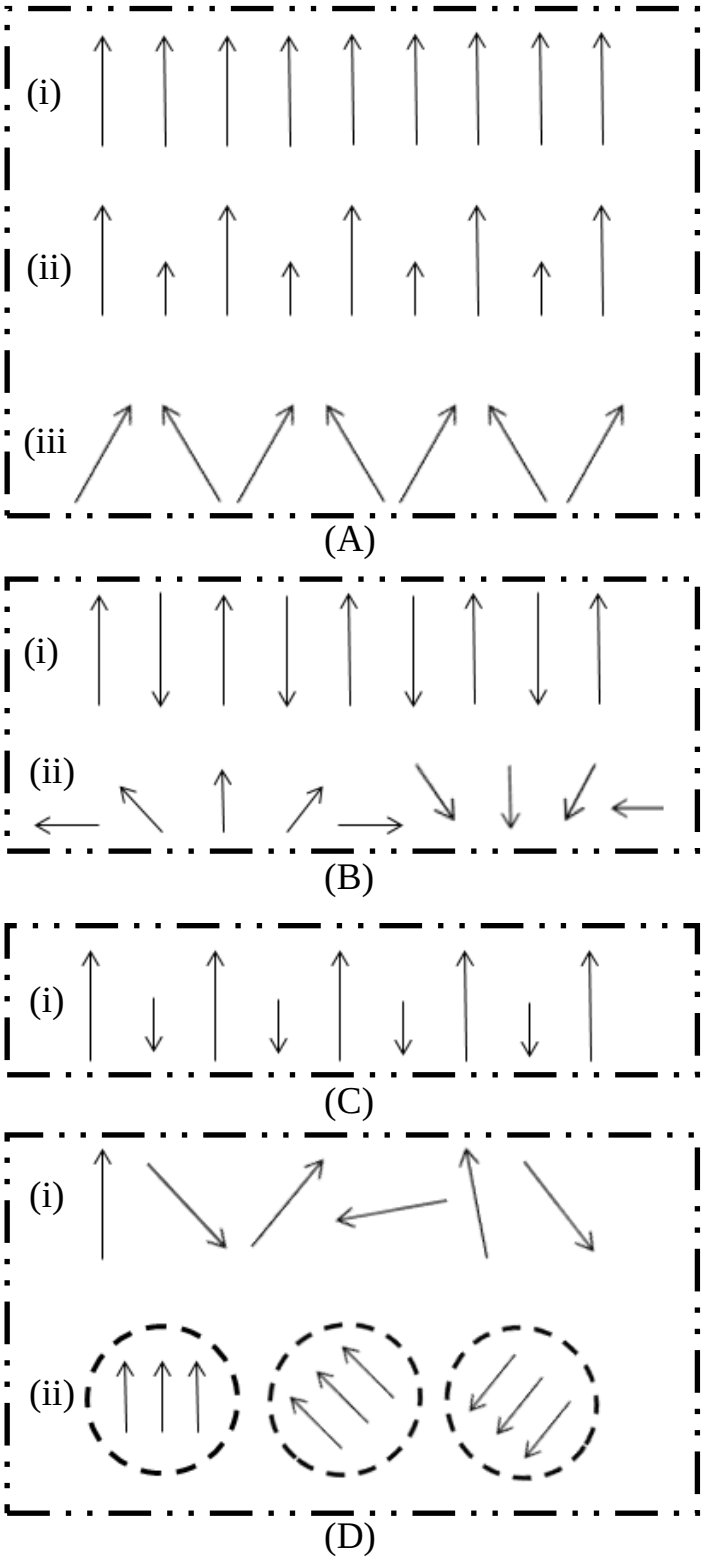

Figure 73: Examples of magnetic structures. (A)(i)-(iii) Ferromagnetic, (B)(i)-(ii) Antiferromagnetic, (C)(i) Ferrimagnetic and (D)(i) Spin Glass and (ii) Cluster Spin Glass. Adapted from Ref [12]

Above the critical temperature, the material is observed to follow the Curie-Weiss law,

with the susceptibility behaving as

$$\chi = \frac{C}{T - \theta_{cw}}, \tag{131}$$

where C is the Curie constant $C = {\mu_B^2 g^2 [S(S+1)]}/{3k_B}$ and θ_{cw} the Curie-Weiss temperature.

The Curie-Weiss temperature can be used to identify the ordering type, with $\theta_{cw} > 0$ signaling ferromagnetic ordering and $\theta_{cw} < 0$ signaling antiferromagnetic ordering for a system exhibiting ideal Curie behavior.

In a ferromagnetic material at temperatures $T<T_C$, the system achieves an energy minimum, i.e. ground state, by aligning the magnetic moments of the electrons parallel to one another, independent of an applied magnetic field. A schematic showing various ferromagnetic ordering arrangements are shown in Figure 73(A)(i-iii). The alignment of spins leads to a measurable net magnetization within the material. In contrast, for an AF material at temperatures $T<T_c$, the system achieves a state of minimum energy by aligning the magnetic moments of the electrons antiparallel to one another. This ordering, shown schematically in Figure 73(B)(i), leads to no net magnetization within the material. A third ordering, ferrimagnetism (shown in Figure 73(C)(i)) occurs when the spins align antiparallel but are of unequal magnitude, leading to a net magnetization within the material.

The onset of magnetic ordering is further observed as a singularity in the measurable heat capacity of the material. The onset of ordering measurably reduces the entropy of the system and the specific heat is observed to behave as

$$c(T) \sim (T - T_c)^{-\alpha}, \tag{132}$$

where α is typically on the order of 0.1 or less [12].

3.2 Spin Glasses

A spin glass is a stochastic, complex magnetic system, characterized by randomly-oriented spins frozen in space below some critical freezing temperature, T_f. Traditionally, spin glasses are believed to form when the magnetic moments within the system are incapable of satisfying all bonds, known as magnetic frustration, and there exists magnetic disorder, driving the system into non-ergodic behavior.

3.3 Magnetic Frustration

Magnetic frustration occurs when a system is unable to simultaneously satisfy all

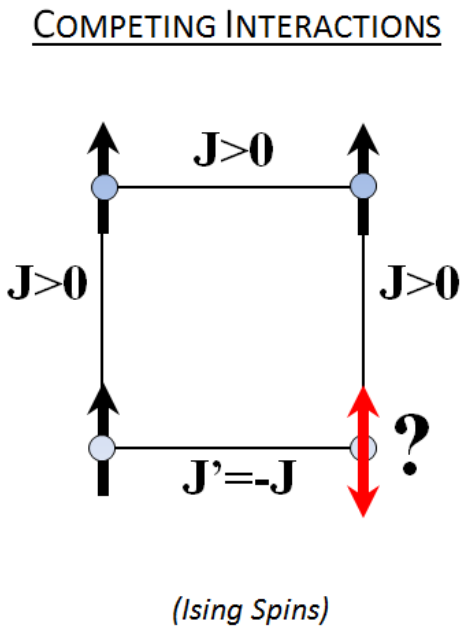

Figure 74: Frustration as a result of competing interactions on the magnetic crystal lattice

magnetic interaction in the system, leading to a degenerate ground state. Frustration can occur through either competing interactions or by antiferromagnetic interaction on a triangular

magnetic crystal lattice geometry. The case for competing interactions is shown in Figure 74. Assuming classical spins that may only assume a value of ±1, also known as Ising spins, three legs of the square are ferromagnetic exchanges between the magnetic moments, while the fourth leg is antiferromagnetic leading to a frustrated bond on the bottom right magnetic moment and a degenerate ground state.

An example of geometric frustration is shown in Figure 75 for Ising spins, where the magnetic exchange between all lattice sites is antiferromagnetic. Since the magnetic moments

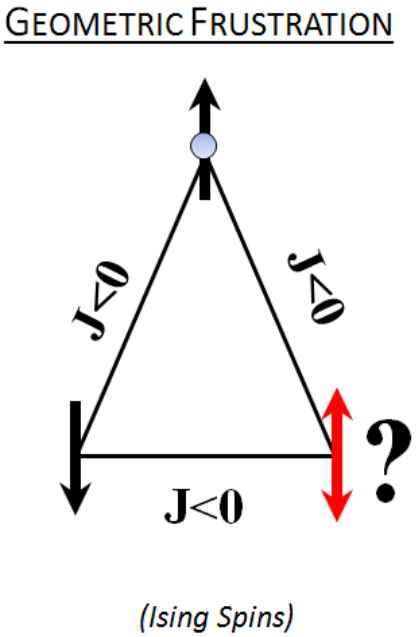

Figure 75: Magnetic frustration as a result of antiferromagnetic exchange and a triangular magnetic crystal lattice

are constrained to a triangle, this leads to the frustrated magnetic moment shown in red at the bottom right of Figure 75. Geometrically frustrated states are realizable experimentally on the two- and the three-dimensional lattices shown in Figure 76.

The presence of frustration in a magnetic sample can be identified experimentally by measuring the magnetic susceptibility as a function of temperature. As stated earlier, an AF

undergoes spontaneous magnetic order at temperatures $T<T_N$. It can be shown [64] that the Curie-Weiss temperature, θ_{CW}, can be extracted via a high-temperature linear fit to $1/\chi$, where

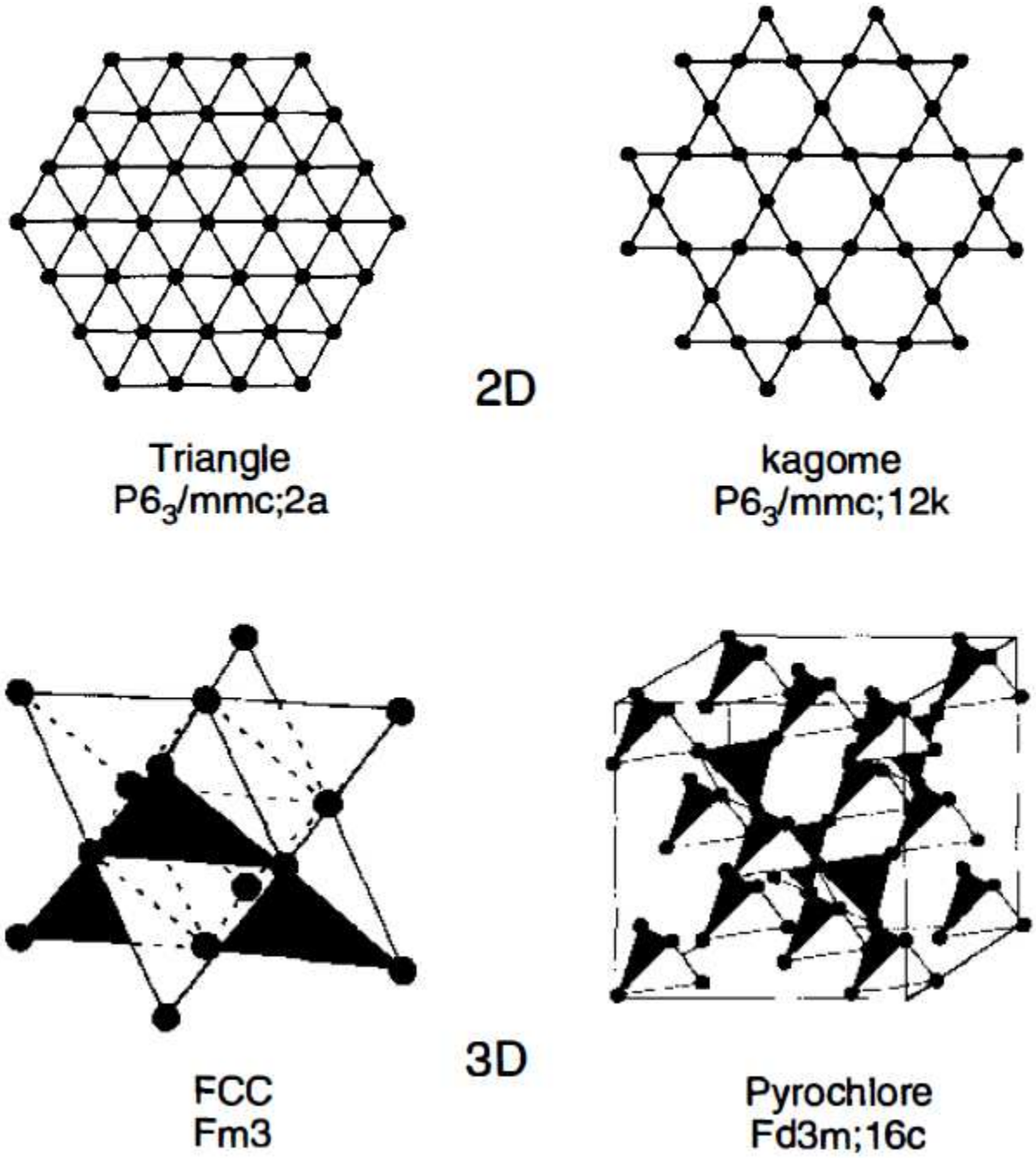

Figure 76: Triangular geometries in two- and three-dimension that lead the magnetic frustration when the nearest-neighbor interactions are antiferromagnetic. The geometries on the left side correspond to lattices with an edge-sharing triangular geometry, while the right side geometries correspond to lattices with a corner-sharing geometry. Scanned from Ref. [64].

θ_{CW} is then the temperature intercept. Since frustration suppresses cooperative ordering within a magnetic system, the ratio of the Curie-Weiss temperature to the Néel temperature in AF magnets may be used as an empirical measure of the frustration, ie

$$f = -\theta_{CW}/T_N \tag{133}$$

When $f > 1$, the system may be considered frustrated. Materials with $f > 10$ are typically considered strongly geometrically frustrated [64]. Figure 77 shows a list of strongly frustrated materials with associated features.

Compound	Magnetic lattice	$-\theta_{cw}$ (K)	T_c (K)	f	Ordered state	Electronic configuration
Two-dimensional magnets						
VCl_2	triangular	437	36	12	AF	$3d^3$
$NaTiO_2$	triangular	1000	<2	>500	—	$3d^1$
$LiCrO_2$	triangular	490	15	33	AF	$3d^3$
$Gd_{0.8}La_{0.2}CuO_2$	triangular	12.5	0.7	16	SG	$4f^7$
$SrCr_8Ga_4O_{19}$	kagome	515	3.5	150	SG	$3d^3$
$KCr_3(OH)_6(SO_4)_2$	kagome	70	1.8	39	AF	$3d^3$
Three-dimensional magnets						
$ZnCr_2O_4$	B-spinel	390	16	24	AF	$3d^3$
K_2IrCl_6	FCC	321	3.1	10	AF	$5d^5$
FeF_3	B-spinel	240	15	16	AF	$3d^5$
$CsNiFeF_5$	B-spinel	210	4.4	48	SG	$3d^8$, $3d^5$
$MnIn_2Te_4$	zinc blende	100	4	25	SG	$3d^5$
$Gd_3Ga_5O_{12}$	garnet	2.3	<0.03	>100		$4f^7$
Sr_2NbFeO_6	perovskite	840	28	30	SG	$3d^4$
Ba_2NbVO_6	perovskite	450	15	30	SG	$3d^3$

Figure 77: Table of strongly frustrated magnets. Scanned from Ref [64], pg. 463

3.4 Spin Glasses

As stated earlier, a spin glass is a magnetic system with randomly-oriented spins frozen in space below some freezing temperature, T_f. The spin glass ground state is degenerate, with a large enough energy barrier between the ground states that prevents the system from being

ergodic. It has been theoretically assumed that to obtain this feature, there must be a significant amount of both magnetic randomness and frustration [62]. However, there has been no conclusive evidence given that shows magnetic randomness is a requirement in the formation of a spin glass and this remains an open question in condensed matter physics.

The study of spin glasses contains many open questions, including the fundamental question of whether the spin glass is a new type of phase transition or simply a failure to achieve thermal equilibrium during the observation time. What is known for spin glasses is that, below T_F, the total magnetization $\sum\langle S_i\rangle_t = 0$, where $\langle\rangle_T$ is the time-average. Additionally, the spins

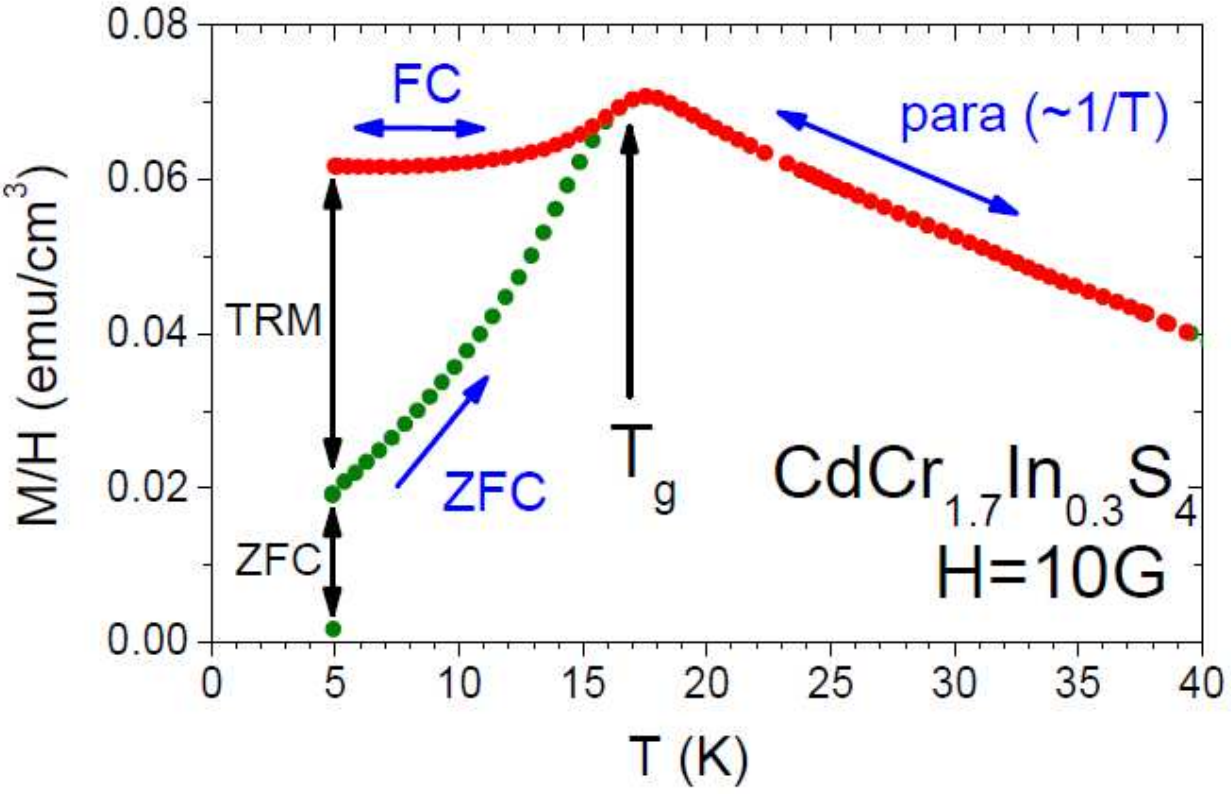

Figure 78: Field cooled (FC) and zero field cooled (ZFC) magnetic susceptibility of $CdCr_{1.7}In_{0.3}S_4$ thiospinel spin glass. Scanned from Ref. [66], pp 4

do not pick out any wave vector, so that $\frac{1}{N}\sum_i \langle S_i \rangle_t \exp(i\boldsymbol{k}\cdot\boldsymbol{R}) = 0$ as $N \to \infty$.

Experimentally, a major feature of a spin glass is thermal magnetic irreversibility in the magnetic susceptibility. Figure 78 shows the typical field-cooled (FC) and zero field-cooled (ZFC) magnetic susceptibility measurements. At the temperature T_g (also referred to as T_f), the susceptibility is seen to bifurcate, indicating thermal magnetic irreversibility. Thermal magnetic irreversibility is also observed in superparamagnetic nanoparticles [65], however the relative flatness of the FC susceptibility observed in spin glasses suggests a collective nature not observed in other irreversible systems. There are many other experimental techniques for identifying spin glasses, including thermo-remanent magnetization and AC susceptibility. A thorough review of these techniques and results can be found in Ref. [66].

4 Spin glassiness and power law scaling in anisotropic triangular spin-1/2 antiferromagnets

Jian Wu, Julia S. Wildeboer, Fletcher Werner, Alexander Seidel, Z. Nussinov and S. A. Solin

Department of Physics and Center for Materials Innovation, Washington University in St. Louis, 1 Brookings Drive, St. Louis, MO 63130

4.1 Abstract

We present data on the magnetic properties of two classes of layered spin S=1/2 antiferromagnetic quasi-triangular lattice materials: $Cu_{2(1-x)}Zn_{2x}(OH)_3NO_3$ ($0 \leq x \leq 0.65$) and its long organic chain intercalated derivatives $Cu_{2(1-x)}Zn_{2x}(OH)_3C_7H_{15}COO.mH_2O$ ($0 \leq x \leq 0.29$), where non-magnetic Zn substitutes for Cu isostructurally. It is found that the intercalated compounds, even in a clean system in the absence of dilution, x=0, show spin-glass behaviour, as evidenced by DC and AC susceptibility, and by time dependent magnetization measurements. A striking feature is the observation of a sharp crossover between two successive power law regimes in the DC susceptibility above the freezing temperature. In contrast to standard theoretical expectations, these power laws are *insensitive* to doping. Specific heat data are consistent with a conventional phase transition in the unintercalated compounds, and glassy behaviour in the intercalated compounds.

4.2 Introduction

The study of both geometric frustration and disorder in quantum magnetism has defined new paradigms of condensed matter for many decades. While frustration plays a major role in compounds like the recently studied “spin liquid” [67] [68] candidate herbertsmithite [69], disorder is thought to be the driving force in systems exhibiting spin glass [70] and quantum Griffiths [71] type behaviour. More controversial is the notion that frustrated interactions alone

may also trigger glassy behaviour in clean quantum spin systems. This debate has been further fueled by recent interest in spin-ice materials [72]. In this Letter, we address this issue in a

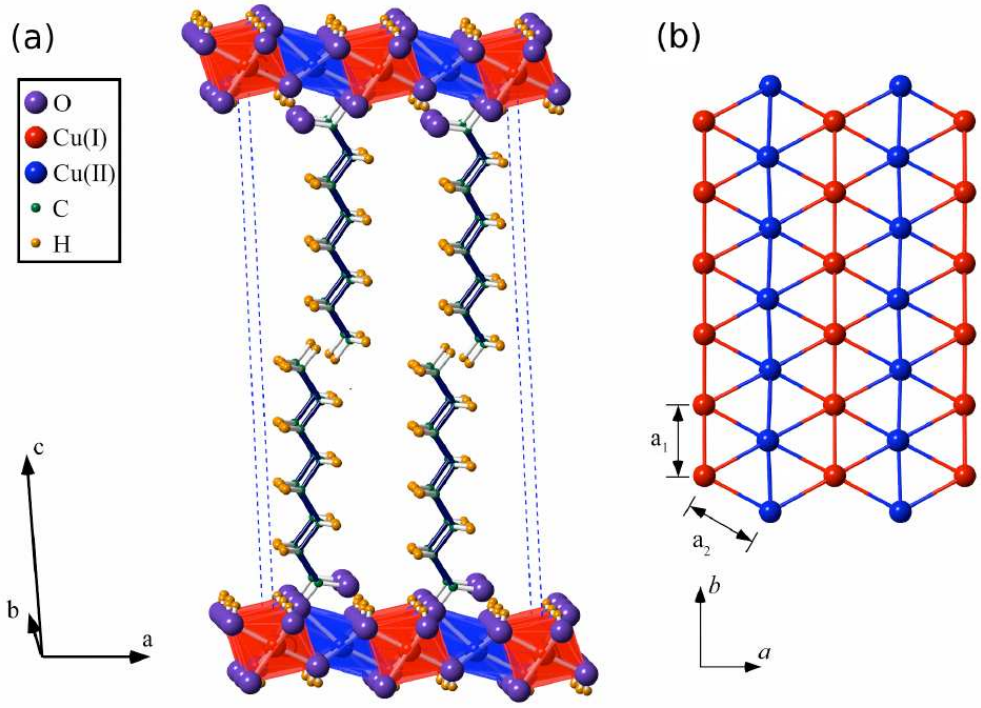

Figure 79: Structure of the long organic chain intercalated CHN compound. a) perspective view of the basal unit. b) c-axis view of the Cu layer and its planar unit cell. a_1=3.03Å, a_2=3.17Å.

different class of materials. In addition, various accounts of glassiness in nearly disorder free spin systems have been given in the literature [73] [74] [75] [76]. While the systems studied in these works all have higher-spin degrees of freedom, in this work we present a case where the relevant magnetic moments have spin-1/2. The systems under investigation are intercalated derivatives of Zn-substituted copper-hydroxy-nitrate (CHN) [77], $Cu_{2(1-x)}Zn_{2x}(OH)_3NO_3$, both in the presence and absence of compositional disorder. We find that in all these systems, spin glassiness is preceded by two regimes where the magnetic susceptibility is characterized by power laws with a sharp crossover. The robustness of these power laws to compositional

disorder is indicative of the fact that the glassiness may be intrinsic, and due to frustration rather than disorder.

In recent years, chemical doping has proven to be an invaluable tool in accessing an extended phase diagram of transition metal oxides, in particular for detecting otherwise inaccessible transitions. Examples are the high temperature superconducting cuprates and pnictides, and various heavy fermion compounds [78] [79] [80] [81]. These systems display some of the most fascinating and mysterious phase diagrams so far found in electronic phases of matter, and due to the importance of chemical doping in their exploration, unraveling the role of disorder is an ever present complication. Glassiness, as well as power law scaling, are frequent companions of the interesting phases found in these compounds.

In this work, we follow this paradigm by applying Zn doping to study a new family of doped frustrated S=1/2 spin systems by building on the nearly triangular geometry of the pure copper (x=0) layered compound CHN. The family of compounds, $Cu_{2(1-x)}Zn_{2x}(OH)_3C_7H_{15}COO.mH_2O$, consists of long organic chain (LOC) intercalated derivatives of Zn-substituted CHN. Antiferromagnetic layers of Cu spin 1/2 ions forming a distorted triangular lattice are separated by as much as 24Å as a result of the LOC intercalation (Figure 79). We report a remarkably robust behaviour of the LOC CHN compounds, which manifests itself through two distinct regimes of power law scaling in the temperature dependence of the DC susceptibility, separated by a sharp crossover. Moreover, we also identify this behaviour in the undoped parent material. We find that Zn doping enhances this effect, showing it to be a robust feature of the physics of the glassy LOC CHN compounds. Furthermore, we present significant new evidence for the glassiness of both the doped and undoped LOC CHN compounds, where Zn doping randomly removes local moments from the Cu^{2+} layer, and so dilutes the magnetic

lattice and its associated magnetic bonds. The ability to control the Zn concentration sheds new light on the relation between compositional disorder and the glassiness of these systems. In the pure copper *x*=0 case, glassy features had been observed earlier [82].

4.3 Structure and preparation

The structure of the LOC CHN compound is shown in Figure 79. The unit cell contains two inequivalent Cu^{2+} ions forming distorted triangular layers. The preparation of the undoped samples follows Refs. [77] for CHN and [82] for the LOC CHN compounds. The method for preparing the Zn-doped samples has been reported earlier [83]. Powder X-ray diffraction measurements have been carried out [83]. For both LOC CHN and unintercalated diluted CHN samples, Zn was found to replace Cu leading to a series of isostructural doped compounds. The LOC CHN samples are characterized by pronounced (00*l*) reflections, as is typical for layered structure compounds with large interlayer distances. From this the interlayer distance was obtained to be 24.2Å, consistent with Ref. [82]. This distance was also found to be independent of Zn doping concentration. A detectable ZnO impurity phase was only observed in the x = 0.65 sample.

The number of water molecules in the gallery, m, in the chemical formula , $Cu_{2(1-x)}Zn_{2x}(OH)_3C_7H_{15}COO.mH_2O$ has not been determined directly, but has been estimated by matching the effective moments of the LOC CHN sample with those of the corresponding CHN samples. If m takes the integer values 1, 1, 3, and 0, for x = 0, 0.13, 0.19, 0.29 LOC CHN samples, respectively [83], the effective moments of two series of samples agree to within 2%. This method of estimating m has little effect on our experimental observations except to introduce a small error in the total molecular weight. This change will be reflected in the calculation of effective moments of Cu^{2+} as noted above.

4.4 DC and AC susceptibility

DC susceptibility data for the diluted CHN system has been reported in Ref. [83]. Both

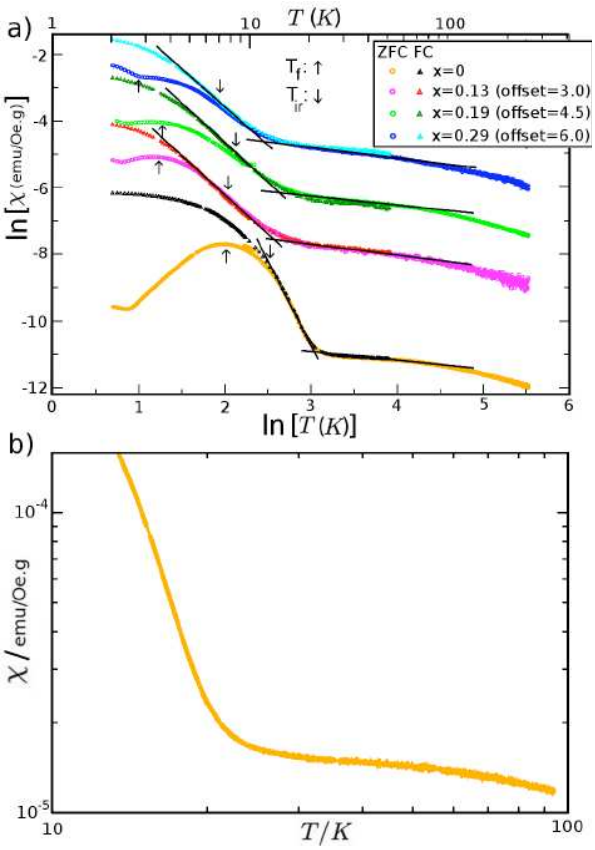

Figure 80: ln(χ) vs. ln(*T*) for the DC susceptibility of long organic chain intercalated CHN samples. a) Both field cooled and zero field cooled data are shown with different offsets for different dopings *x* as indicated. The freezing temperature, T_f, and irreversibilty temperature, T_{ir}, are indicated by arrows. Linear fits identify various temperature regimes where χ(*T*) is well described by power laws. In the lower temperature regimes, FC data was used for the fit. However, the ZFC data is seen to follow similar and in some cases almost identical power laws. b) Close-up of the *x*=0 ZFC data. The two power-law regimes and their sharp crossover are clearly visible.

the Curie-temperature and the Néel temperature vary with Zn concentration, but are on the order of 10K in agreement with density functional values for the exchange couplings [84]. The value of the exchange interaction parameter is known to be sensitive to the Cu-OH-Cu bond angle,

with both ferromagnetic (FM) and anti-ferromagnetic (AFM) values being possible. In CHN the angle is close to the FM-AFM crossover [77] rendering the material weakly anti-ferromagnetic. Interestingly, with increased Zn concentration the Curie constant was found to change sign and become ferromagnetic [83]. There was, however, no FM phase seen at low temperature and a complete analysis of this behaviour would likely need to take into account Dzyaloshinskii-Moriya (DM) interactions, which result from the relatively low symmetry at the Cu site [82].

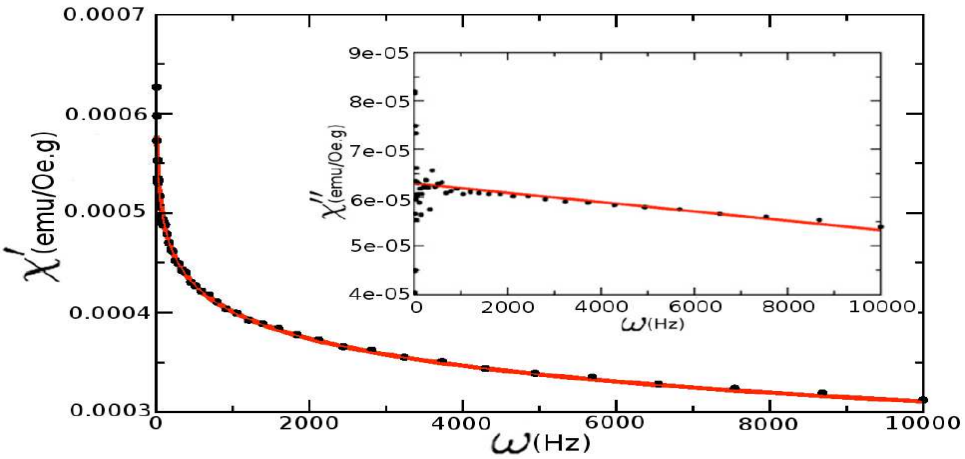

Figure 81: AC susceptibility of x=0 sample at T=10K. The real part is fitted to the functional form $\chi'=\chi_0-c\ln(\omega)$. The linear fit of the imaginary part (inset) approaches $\pi c/2$ at $\omega=0$ to within 2% accuracy.

We will now focus on the LOC CHN samples with x=0, 0.13, 0.19 and 0.29, whose respective Curie constants were found to be −94K, −74K, −67K and −64K. The susceptibility data are shown in Figure 80. A clear difference between the zero field cooled (ZFC) and field cooled (FC) data below a temperature T_{ir}~6−12K is a first indication of the glassiness of the LOC CHN samples. No similarly large effect has been seen in the diluted CHN samples [83]. Note that the FC susceptibility of the x=0 sample grows by two orders of magnitude between 20K and 2K. Such changes have been seen in other spin glasses and electronic glasses in a variety of response functions [85]. It is worth pointing out that in the LOC CHN case, the

ZFC/FC difference actually diminishes at finite Zn concentration compared to the undoped parent compound. This may indicate that the glassiness of the system is indeed driven by frustration rather than disorder. Similarly, the freezing temperature T_f as determined by the peak in the ZFC susceptibility is ~8K for the x=0 sample, and is ~2× lower for the Zn-doped samples.

A remarkable feature seen in the log-log plots of Figure 80 is the presence of a sharp crossover between two distinct power law regimes above T_f. The first of these regimes corresponds to a temperature window typically between 5K and 12K, where $\chi \propto T^{-a}$ with different exponents $a \simeq 5$ for x=0 and $a \simeq 2$ for $x>0$. In a second regime at higher temperatures roughly between 12K and 90K, $\chi \propto T^{-b}$ with $b \simeq 0.3$ for all samples, below a Curie tail with $\chi \propto T^{-1}$ for $T>90K$. This behaviour is slightly more pronounced in the $x>0$ samples which all have very similar exponents, but is clearly identifiable also in the x=0 sample. Hence the sharp crossover between two different power law regimes as a precursor to the spin glass phase appears to be a robust feature of the physics of the LOC CHN samples. To our knowledge, the finding of power law behaviour that is insensitive to doping has not been reported earlier. We note that FC and ZFC data are indistinguishable in the higher temperature regime. In the lower temperature regime, the FC data have been used for the linear fits in Figure 80. However, the ZFC data display power law behaviour with similar exponents even there.

The frequency dependence of the AC susceptibility of the x = 0 LOC CHN sample is shown in Figure 81. The real part χ' was found to be extremely well described by the logarithmic functional form $\chi' = \chi_0 - c\ln(\omega)$ at low frequencies $<10^4$ Hz, a standard behaviour [86] for spin glasses. This is in good agreement with the imaginary part (inset), whose low frequency limit is a non-zero constant that agrees well with $\pi c/2$ as determined from the real part via Kramers-

Kronig relations. These findings provide strong new evidence for spin-glass physics in the x = 0 LOC CHN sample, even though this system seems to have no apparent structural disorder.

4.5 Time dependent magnetization

The time evolution of the isothermal remanent magnetization $M_{ZFC}(t)$ of the LOC CHN samples has been studied in the following steps. Samples were first cooled in zero field to 2 K (well below the freezing temperature) and then kept in a magnetic field, H, for 10 minutes. After

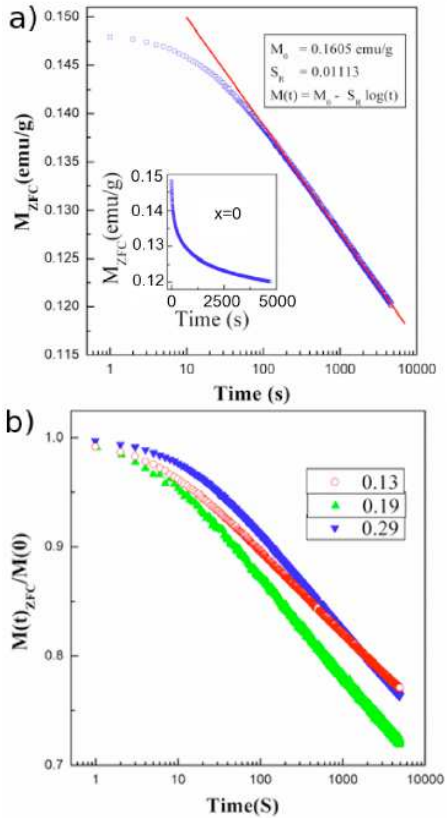

Figure 82: Isothermal remanent magnetization MZFC(t) vs. log(t) at 5000 Oe. a) x=0. Inset: The normal plot of MZFC(t) for x=0. b) The scaled remanent magnetization MZFC(t)/M(0) at 5000 Oe for x=0.13, 0.19 and 0.29.

switching off the applied field, we measured $M_{ZFC}(t)$ for 5000 seconds. The experiment was repeated in 5 different fields (50 Oe, 500 Oe, 5000 Oe, 10000 Oe and 20000 Oe). The data for 5000 Oe are shown in Figure 82. The time dependence of $M_{ZFC}(t)$ of the x = 0 sample is plotted in Figure 82 a), in which we observed a long time slow non-exponential relaxation. For $t \geq 100$s,

$M_{ZFC}(t)$ can be described by $M_{ZFC}(t)=M_0-S_R\log(t)$, in which M_0 is a constant and the coefficient S_R is the magnetic viscosity. This logarithmic decay law is a characteristic feature of spin glass like systems. In order to better compare the relaxation behaviours of other doped samples, a scaled $M_{ZFC}(t)/M(0)$ quantity is plotted in Figure 82b) instead of the absolute values. At 5000 seconds, their $M_{ZFC}(t)$ values slowly decay to 70−80% of the initial values $M(0)$. Their long time decay behaviours all follow the logarithmic form with different coefficients S_R. The time relaxation of $M_{ZFC}(t)$ under the other 4 fields shows similar behaviour and follows a logarithmic decay law after t>100s. The initial values $M_{ZFC}(0)$ increase rapidly with field for H<5kOe and slowly approach their saturation value when H>5kOe.

4.6 Specific heat

Specific heat (C) measurements were performed on a Quantum Design PPMS with the relaxation method [87]. The powder samples were compressed into ten 20mg thin cylindrical disks and attached to a platform by Apiezon N grease. A reference measurement was taken first to obtain the heat capacity of the platform and grease. In the following sample measurement, the reference data was subtracted from the total heat capacity yielding the pure sample C. Figure 83 shows the C data. Sharp peaks in the diluted CHN data indicate a large amount of entropy loss during the antiferromagnetic phase transitions. This supports a picture based on the existence of conventional long-range magnetic order in the diluted CHN samples. The peak position of C/T decreases as the Zn doping increases, which is similar to the doping dependence of the DC susceptibility peaks [83]. We should also note that in the temperature range 2K<T<4K, the specific heat has a roughly T^2 behaviour. This is also seen up to $T\simeq 20K$ or more in the LOC CHN data, Figure 83b), as noted for x=0 in Ref. [82]. We caution that since there are no proper

nonmagnetic materials with an analogous lattice structure available, such as those corresponding to x=1, the pure magnetic contribution cannot be easily separated. To shed more light on this issue, we compared C in zero field to that in a field of B=5T, where the Zeeman energy is

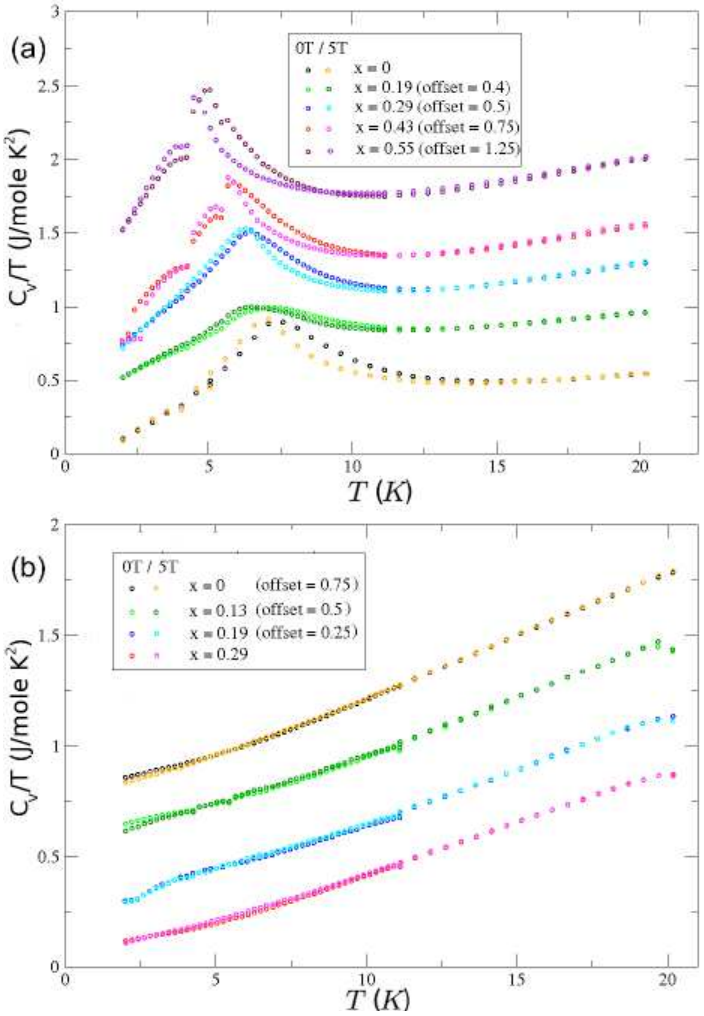

Figure 83: Specific heat divided by temperature, for diluted CHN (a) and long organic chain intercalated CHN (b) samples, with and without an applied magnetic field of B=5T. Data for different Zn concentration x are mutually offset for clarity.

comparable to the magnetic exchange interaction (see above). This has a pronounced effect on the peak structure in the diluted CHN samples, giving further evidence of the magnetic origin of this peak. On the other hand, the effect of the magnetic field on the overall C is very small in the LOC CHN samples. The small difference between B=0 and B=5T is barely visible in Figure

83b), and is found to be of order 0.1J/mol K. This small magnetic field dependence indicates that lattice degrees of freedom dominate *C*.

One may attribute this dominance to the large unit cell of the system, especially for the LOC CHN samples, and to the enhanced phonon density of states at low energies due to the approximately two-dimensional character of the system. Furthermore, the magnetic peak (and the associated field dependence) is seen to be absent in the LOC CHN samples. This is also a common feature seen in many spin glass like systems [86], due to the gradual freezing of spins or spin clusters over a large temperature range. In particular, if spins are locked into large clusters even above T_f, this may provide an additional explanation why magnetic degrees of freedom do not release much entropy at low temperatures, and contribute relatively little to *C* at low-*T*. From the weak magnetic field dependence, we conclude that the approximate T^2-behaviour of *C* is chiefly due to phonons. This is a direct consequence of the quasi-two-dimensional geometry of the system. However, a close inspection of the graphs in Figure 83b) shows that the low-*T* limit of *C*/*T* is non-zero, hence implying a weak linear contribution to *C*. This is the expected low-*T* contribution of a spin glass (or structural glass) phase [85] [62].

4.7 Discussion

The CHN and LOC CHN family of compounds allows a controlled study of the role of non-magnetic impurities in a layered frustrated spin-1/2 compound with glassy behaviour. We have given further evidence for the presence of a spin glass phase in the “clean" (*x*=0) LOC CHN parent compound, and tracked the observed phenomenology as a function of Zn concentration, *x*. The *x*=0 limit in the absence of Zn substitution was seen to be the case where the glassy features were most pronounced. This may strengthen earlier claims according to which the spin glass phase is driven by frustration rather than disorder. It is likely that anisotropy introduced by DM

interactions also plays a role in the observed behavior [82] [88], especially in view of the weakness of the energy scale associated with exchange interactions. We caution that DM terms are particularly sensitive to the symmetry of the local environment, and thus could be more affected by disorder introduced by the organic chains in the LOC CHN samples. Detailed calculations on the strength of these terms and the disorder necessary to reproduce the observed behaviour are left for future studies.

A remarkable effect was found to emerge at temperatures above T_f in the form of two successive power law regimes in the DC susceptibility with a sharp crossover. This effect was furthermore seen to be robust against Zn doping, becoming rather more pronounced in the $x>0$ samples. This, together with the small value of the power law exponent seen at higher temperatures, suggest an unconventional nature of the spin glassiness seen in these compounds.

To see this, we note that the occurrence of power laws above a transition into a glassy state is somewhat reminiscent of the picture developed in Ref. [89]. There it was argued that a quantum Griffiths phase [71] may be unstable to the formation of a cluster glass phase at low temperatures. Above the transition temperature, the quantum Griffiths behaviour is still expected to be seen, which leads to the observation of power laws in thermodynamic quantities [90]. Specifically, the susceptibility is predicted to be of the form $\chi \propto T^{\alpha-1}$ with $\alpha>0$. We note, however, that the value of α in this scenario is not universal, but is expected to depend rather sensitively on doping. This was observed in $CePd_{1-x}Rh_x$ [91], where α changes by a factor greater than 4 in response to a change of doping by a few percent. In contrast, the variation of $\alpha=1-b$ for the high-T power law regimes seen in Figure 80 is less than 10%. In the quantum Griffiths based scenario [90], one also assumes proximity to a quantum critical point, at which α approaches zero. Hence in this scenario, one expects α to be considerably less than 1, whereas $\alpha \approx 0.7$ in our case.

Furthermore, the quantum Griffiths scenario can at present only explain the occurrence of a single power law with exponent less than 1, and offers no direct explanation for the power law behaviour seen at low temperature. To our knowledge, a crossover between different power laws as seen in the LOC CHN compounds has not been previously observed or predicted, and may well be the hallmark of new physics. The stability of the scaling forms and their insensitivity to doping may be consistent with a picture based on self-generated glassiness [92]. In this case, an intrinsic, frustration based mechanism may lead to glassy low temperature physics and overwhelm the doping dependence of the observed power laws. A detailed understanding of this behaviour and the search for possible incarnations in other systems remain an interesting challenge for future work.

4.8 Acknowledgements

We would like to thank the Center for Materials Innovation for support of this work. AS would like to acknowledge support by the National Science Foundation under NSF Grant No. DMR-0907793, as well as discussions with V. Dobrosavljević.

4.9 Addendum: Neutron Scattering

Observing the magnetic ordering in antiferromagnets can be challenging, given that no macroscopically observable magnetic fields are generated when magnetic ordering occurs, as is the case in ferromagnetic and ferrimagnetic ordering. Therefore, neutron scattering may be used as a probe into the magnetic ordering of the system. The neutron has a magnetic moment that couples with the spin of the electron, resulting in a scattering cross section. In the case of ordered electronic moments, elastic neutron scattering, i.e. neutron diffraction, leads to Bragg reflection peaks in the neutron intensities, along with the peaks associated with scattering off of the ionic nuclei. The magnetic Bragg peaks are distinguishable from those created by the crystal lattice because they are temperature dependent, disappearing at temperatures $T>T_c$.

Another neutron scattering technique is inelastic neutron scattering. The inelastic scattering of neutrons involves an exchange of energy between the neutrons and the sample. This exchange results in a shift in the exiting neutron's wavelength relative to the incident neutron. The shift in energy of the exiting neutron may be found using time of flight (TOF) measurements. Inelastic neutron scattering can be used to extract the dynamic structure factor $S(Q,\omega)$, where Q is the change in wave vector and $\hbar\omega$ the change in energy [93].

Whereas elastic neutron scattering is a technique to obtain static information on the samples magnetic and crystal structure, inelastic neutron scattering is used to obtain dynamic information on the magnetic and crystal field excitations in a sample [93].

4.10 Initial Inelastic Neutron Scattering Measurements

The inelastic neutron scattering intensity for a powder sample of Copper Hydroxy Nitrate (CHN) is shown in Figure 85. The onset of magnetic ordering in the CHN sample was previously observed to occur at a Néel temperature of T_N=7K, indicated by both a cusp in the thermal measurement of $1/\chi$, where χ is the magnetic susceptibility, and a correlated peak in the specific heat capacity [94]. The emergence of inelastic scattering at T=2K, highlighted by a dotted red box in Figure 85(B), is suggestive of magnetic ordering with resulting magnon excitations. Figure 84 shows the energy transfer for a single Q momentum value at different temperatures, confirming the emergence of increased inelastic scattering for T<6K. However, the peak is not well-defined and the lack of the peak occurring at all for T<8K, as predicted from previous measurements [83] [94], is puzzling.

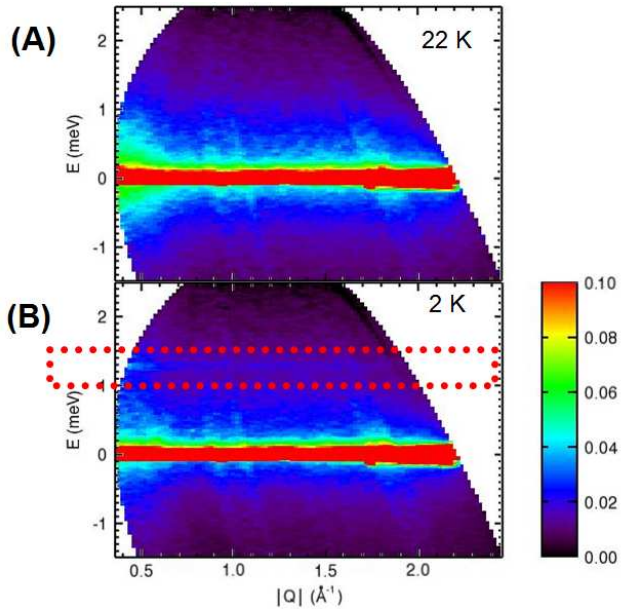

Figure 85: Inelastic neutron scattering data for pure CHN sample at two temperatures: (A) T=22K and (B) T=2K. The T=2K plots suggests the onset of ordering via inelastic magnon scattering. From Ref [98].

It is likely that, if there exists a peak for T<8K, it is masked by the incoherent neutron scattering noise. The high noise in the scattering data is a result of undesirable incoherent neutron scattering off of the many hydrogen ions in the sample, leading to a significant reduction

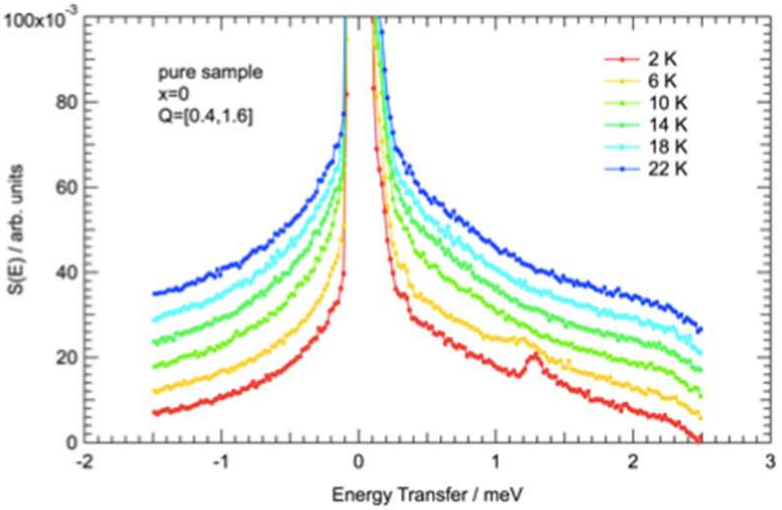

Figure 84: Inelastic scattering intensity data of pure CHN sample at varying temperatures. From Ref [98]

in the signal:noise ratio. This situation can be remedied by synthesizing a deuterated compound,

where the hydrogen isotope deuterium (D or ^{2}H) is substituted into the compound. The incoherent neutron scattering cross section of D is 2.05 fm^2, as compared to Hydrogen's incoherent neutron scattering cross section of 80.27, a factor of nearly 40 times larger [95].

4.11 Deuterated Neutron Scattering

4.11.1.1 *Sample Synthesis*

A deuterated sample of pure copper hydroxy nitrate was synthesized, referred to here-after as deuterated copper hydroxy nitrate (CDN). The synthesis route is shown in Eqs. (134-(136).

$$Cu(s) + 4DNO_3(aq) \rightarrow Cu(NO_3)_2.mD_2O(aq) + 2D_2O(g) + 2NO_2(g) \quad \textbf{(134)}$$

$$Cu(NO_3)_2.mD_2O(aq) + 2NaOD(aq) \rightarrow Cu(OD)_2(s) + 2Na(NO_3)_2(aq) + mD_2O(aq) \quad \textbf{(135)}$$

$$3Cu(OD)_2(s) + Cu(NO_3)_2.mD_2O(aq) \rightarrow 2Cu_2(OD)_3NO_3(s) + \mathrm{m}D_2O(aq) \quad \textbf{(136)}$$

First, 6.05 grams of solid copper pellets were reacted with 8 ml of 65% by weight (bw) deuterated nitric acid. This reaction was carried out over several minutes, creating copper nitrate hydrate, water vapor and noxious nitric oxide. After the reaction rate became negligible, the solution was diluted with D_2O and the remaining copper pellets filtered out. The remaining solution was then vacuum desiccated for four weeks to remove any residual DNO_3.

A fraction (one-third) of the desiccated $Cu(NO_3)_2.mD_2O$ was then reacted with 5 ml of 30% bw NaOD and the solid precipitate $Cu(OD)_2$ was separated by filtering and washing with deuterium six times. The $Cu(OD)_2$ in solution was then combined with the remaining $Cu(NO_3)_2.mD_2O$ and hydrothermally reacted at 65°C for 3 days. After 3 days, the pale blue

precipitate was separated by filtering and washing with deuterium six times, then dried at 75°C

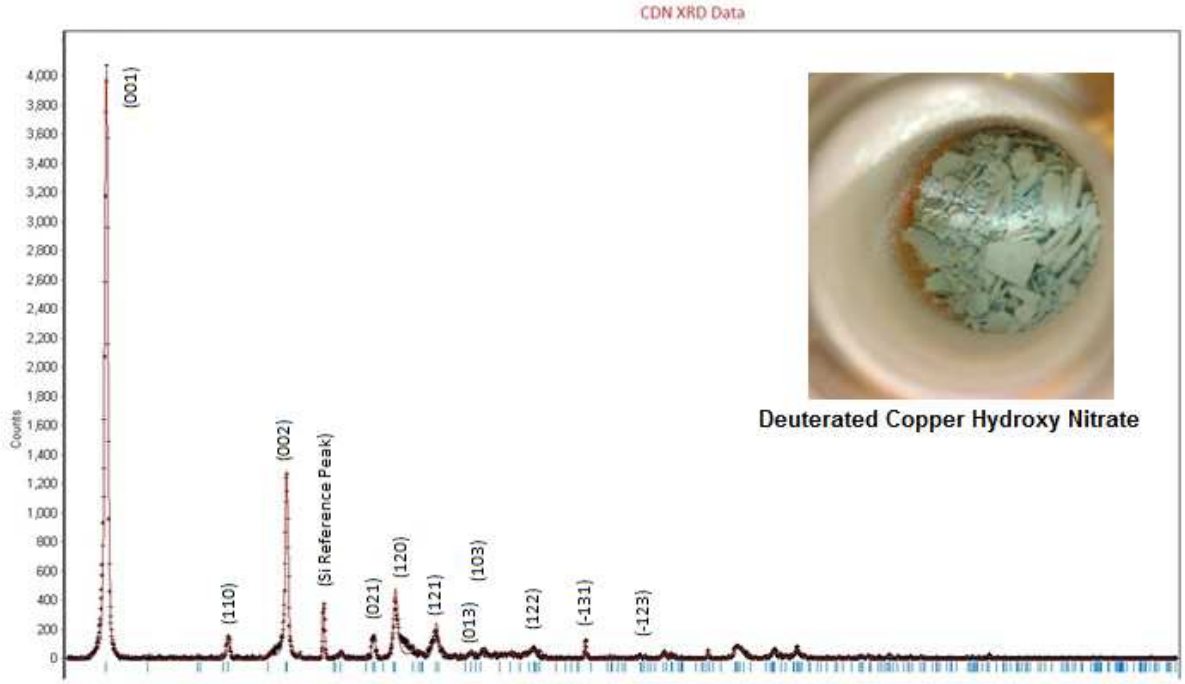

Figure 86: X-ray diffraction (XRD) pattern of CDN with fit and Bragg peaks identified. (inset: powder sample) From Ref [99].

in air for 24 hrs. This process yielded 1.8 grams for CDN.

The powder x-ray diffraction (XRD) of the CDN sample is shown in Figure 86, confirming that the deuterated compound has the same structure as the original compound of interest, CHN. Given the high cost of synthesizing the deuterated compound, no susceptibility and heat capacity data were taken, since both require a sample preparation that potentially contaminates the sample for neutron scattering.

4.11.1.2 *Elastic Neutron Scattering of the Deuterated Sample*

Following structural confirmation, elastic neutron scattering was performed at Oak Ridge National Lab. Figure 87 shows the subtracted neutron scattering data, where the high temperature Bragg peaks have been subtracted to isolate the emergence of any magnetic ordering. Initial indexing has been performed, revealing a thermal ordering occurring at T=6K

along the (*h* 0 0) plane. The minor peaks, indexed as (0 ½ ½) and (0 0 1) do not appear to increase with decreasing temperature and are therefore most likely the ions of the crystal lattice settling into more energetically favorable position as thermal energy is removed from the system. In contrast, the in-plane Bragg peaks are shown to increase in intensity as the sample is cooled, confirming thermal magnetic ordering and supporting the predicted antiferromagnetic ordering at T<14K.

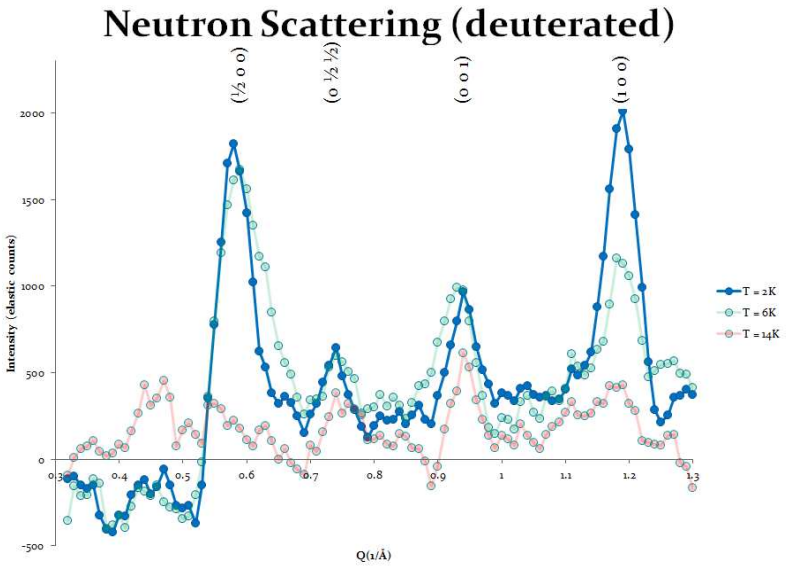

Figure 87: Elastic neutron scattering data of CDN at various temperatures with the structural Bragg peaks (found a high temperature) subtracted out and initial indexing performed. From Ref [97]

5 Closing Statements on the Role of Magnetic Disorder on Spin Glass Formation

We have shown empirical evidence that a cluster spin glass is capable of forming absent the addition of magnetic disorder. While doping was observed to increase the frustration of the system, the pure compound still undergoes a cluster spin glass transition. Additionally, it has been further shown through inelastic neutron scattering experiments that the parent compound, CHN, likely undergoes an antiferromagnetic phase transition at temperature $T<14K$.

The emergence of a cluster spin glass under no imposed magnetic disorder suggests that the historical assumption that magnetic disorder is required to form a spin glass may be wrong. Research into additional examples of non-diluted spin glasses should lend phenomenological insight into the factors driving the frustrated magnetic system into a spin glass phase.

The collected neutron data supports the previously predicted phase transition of the CHN parent compound into an antiferromagnetic state. However, higher resolution neutron beam scattering is required to perform full qualitative analysis of the characteristics of this magnetic ordering. Additionally, fiscally viable synthesis of the long chain, cluster spin glass compound is required to confirm the predicted formation of a cluster spin glass.

Bibliography

[1] J. Vardalas, "Twists and Turns in the Development of the Transistor," *Today's Engineer,* vol. May, May 2003.

[2] D. R. S. Cumming, S. B. Furber and D. J. Paul, *PhiL.C. Trans. R. Soc. A,* vol. 372, no. 2012, 2014.

[3] M. W. Shinwari, M. J. Deen and D. Landheer, *Microelectronics Reliability,* vol. 47, pp. 2025-2057, 2007.

[4] S.A. Solin, T. Thio, D. R. Hines and J. J. Heremans, *Science,* vol. 289, p. 1530, 2000.

[5] T. Zhou, D. Hines and S.A. Solin, *Appl Phys Let,* vol. 78, no. 5, pp. 667-669, 2001.

[6] A. Rowe, D. Hines and S.A. Solin, *Appl Phys Let,* vol. 83, no. 6, p. 1160, 2003.

[7] K. Wieland, Y. Wang, L. Ram-Mohan, S.A. Solin and A. Girgis, *Appl Phys Lett,* vol. 88, p. 052105, 2006.

[8] K. Wieland, et al., *Phys. Rev. B,* vol. 73, no. 15, p. 155305, 2006.

[9] A.K.M. Newaz, et al., *App. Phys. Lett.,* vol. 97, p. 082105, 2010.

[10] Y. Wang, et al., *App. Phys. Let.,* vol. 92, p. 262106, 2008.

[11] A.K.M. Newaz, et al., *Phys Rev B,* vol. 79, p. 195308, 2009.

[12] N. W. Aschcroft and N. D. Mermin, Solid State Physics, United States of America: Thomson Learning, Inc, 1976.

[13] S. Sze, Physics of Semiconductor Devices, New York: John Wiley & Sons, Inc, 1981.

[14] L.C. Tran, F.M. Werner, A.K.M. Newaz and S.A. Solin, *J. Appl. Phys.,* vol. 114, p. 153110, 2013.

[15] P. Drude, *Annalen der Physik,* Vols. 1, 3, pp. 566, 369, 1900.

[16] Y. Wang, "Extraordinary Electroconductance in III-V Metal Semiconductor Hybrid Structures," *Ph.D. Dissertation,* 2008.

[17] G. Burns, Solid State Physics, San Diego: Academic Press, Inc., 1985.

[18] J. Chelikowsky and M. Cohen, *Phys. Rev. B,* vol. 14, p. 556, 1976.

[19] B. E. A. Saleh and M. C. Teich, Fundamentals of Photonics, Hoboken, New Jersey: John Wiley & Sons, 2007.

[20] E. D. Palik, Handbook of Optical Constants of Solids, New York: Academic Press, 1985.

[21] M. Balkanski and R. Wallis, Semiconductor Physics and Applications, Oxford: Oxford University Press Inc., 2000.

[22] B. L. Sharma, Metal-Semiconductor Schottky Barrier Junctions and Their Applications, New York: Plenum, 1984.

[23] F.M. Werner and S.A. Solin, *Unpublished raw data,* 2014.

[24] L. van der Pauw, *Philips Research Reports,* vol. 13, no. 1, pp. 1-9, 1958.

[25] A. Gilbertson, et al., *Appl. Phys. Lett.,* vol. 95, p. 012113, 2009.

[26] J. Lee , et al., *Applied Surface Science,* vol. 233, p. 402–410, 2004.

[27] S. Wolf and R. Tauber, Silicon Processing for the VLSI Era: Volume 1 - Process Technology, 1986.

[28] N. Braslua, J. Gunn and J. Staples, *Solid-State Electronics,* vol. 10, pp. 381-383, 1967.

[29] Y. Suzaki and T. Atsushi, *Appl. Optics,* vol. 14, no. 12, pp. 2809-2810, 1975.

[30] J. T. Wallmark, *Proceedings of the IRE,* vol. 45, no. 4, pp. 474-483, 1957.

[31] J. Henry and J. Livingstone, *Sensors Journal, IEEE,* vol. 2, no. 4, pp. 372-376, 2002.

[32] H. Dember, *Phys Z,* vol. 32, pp. 554-556, 1931.

[33] Model 6220 DC Current Source, Model 6221 AC and DC Current Source Reference Manual, Cleveland: Keithley Instruments, Inc, 2004.

[34] W. Shockley and W. Read, *Phys. Rev.,* vol. 87, p. 835, 1952.

[35] S. Chand and J. Kumar, *Semicond. Sci. technol.,* vol. 12, p. 899, 1997.

[36] K. Maeda, H. Ikoma, K. Sato and T. Ishida, *Appl. Phys Lett.,* vol. 62, p. 2560, 1993.

[37] S. Sze, C. Crowell and D. Kahng, *J. Appl. Phys.,* vol. 35, p. 2534, 1964.

[38] P. Chattopadhyay, *J. Phys. D.,* vol. 29, p. 823, 1996.

[39] J. Ellis and P. Barnes, *Appl. Pys. Lett.,* vol. 76, p. 124, 2000.

[40] C. Sah, R. N. Noyce and W. Shockley, *Proc. IRE,* vol. 45, p. 1228, 1957.

[41] S. Cheung and N. Cheung, *Appl. Phys. Lett,* vol. 49, no. 2, pp. 85-87, 1986.

[42] J. Waldrop, *Appl. Phys. Lettrs,* vol. 44, p. 1002, 1984.

[43] T. Kleinpenning, *Solid-State Electronics,* vol. 22, pp. 121-128, 1979.

[44] J. Lee, et al., *Journal of the Korean Physical Society,* vol. 37, no. 6, pp. 966-970, 200.

[45] B. Ridley, *Proc. Phys. Soc.,* vol. 82, pp. 954-966, 1963.

[46] M. Shaban, K. Nomoto, S. Izumi and T. Yoshitake, *Appl. Phys. Lett.,* vol. 94, p. 222113, 2009.

[47] A. Van Der Ziel, Noise in Solid State Detectors and Circuits, New York: Wiley, 1986.

[48] G. Lu, J. Galvan, C. Jeloyan, G. Goumy and V. Marcoux, *Mater. Sci. Eng., C,* vol. C21, p. 203, 2002.

[49] K. Lee , et al., *J. Electrochem. Soc.,* vol. 155, p. H959, 2008.

[50] D. L. Stein, "Spin Glasses: Still Complex after All These Years," in *Decoherence and Entropy in Complex Systems*, 2004, pp. 349-361.

[51] Y. Ying, J. Kim and Y. Lee, *Journal of the Korean Physical Society,* vol. 58, no. 4, pp. 969-972, 2011.

[52] S. Kirkpatrick, C. Gelatt Jr. and M. Vecchi, vol. 220, no. 4598, pp. 671-680, 1983.

[53] D. Amit, H. Gutfreund, Sompolinsky and H., *Phys. Rev. Lett. ,* vol. 55, p. 1530, 1985.

[54] J. Bryngelson, Wolynes and P.G., *Biopolymers,* vol. 30, p. 177, 1990.

[55] D. Stein, Spin Glasses and Biology, Singapore: World Scientific, 1992.

[56] H. Nishimori, Statistical Physics of Spin Glasses and Information Processing, Oxford:

Oxford University Press, 2001.

[57] B. Odom , et al., "New Measurement of the Electron Magnetic Moment Using a One-Electron Quantum Cyclotron," *Phys. Rev. Lett.*, vol. 97, p. 030801, 2006.

[58] D. J. Griffiths, Introduction to Quantum Mechanics, Pearson Education, 2008.

[59] B. Figgis and J. Lewis, The Magnetochemistry of Complex Compounds, New York: Wiley, 1960.

[60] H. Kramers, *Physics*, vol. 1, p. 182, 1934.

[61] C. D. Hu, *Nature*, vol. 10, pp. 180-181, 2014.

[62] K. Binder and A. Young, *Rev. Mod. Phys.*, vol. 58, p. 801, 1986.

[63] E. L. Nagaev, *Phys.-Usp.*, vol. 39, p. 781, 1996.

[64] A. Ramirez, G. Espinosa and A. Cooper, *Phys. Rev. Lett.*, vol. 64, p. 2070, 1990.

[65] J. Dormann, D. Fiorani and E. Tronc, Advances in Chemical Physics, Vol XCVIII, J. Wiley & Sons, Inc, 1997.

[66] E. Vincent, *arXiv.org*, no. arXiv:cond-mat/0603583, 2006.

[67] P. Anderson, *Science,* vol. 235, p. 1196, 1987.

[68] P. Lee, *Science,* vol. 321, p. 1306, 2008.

[69] J. Helton, et al., *Phys. Rev. Lett.*, vol. 98, p. 107204, 2007.

[70] D. Reich, T. Rosenbaum and G. Aeppli, *Phys. Rev. Lett.*, vol. 59, p. 1969, 1987.

[71] R. Griffiths, *Phys. Rev. Lett.*, vol. 23, p. 17, 1969.

[72] C. Castelnovo, R. Moessner and S. Sondhi, *Nature,* vol. 451, p. 42, 2008.

[73] A. Wills , et al., *Phys. Rev. B.*, vol. 64, p. 094436, 2001.

[74] W. Bisson and A. Wills, *J. Phys.: Condens. Matter*, vol. 20, p. 452204, 2008.

[75] J. Greedan, *J. Mater. Chem*, vol. 11, p. 37, 2001.

[76] H. Zhou , et al., *J. Solid State Chem,* vol. 183, p. 890, 2010.

[77] G. G. Linder, M. Atanasov and J. Pebler, *J. Solid State Chem,* vol. 116, p. 1, 1995.

[78] J. Bednorz and K. Muller, *Rev. Mod. Phys.,* vol. 60, p. 585, 1988.

[79] M. Rottern, M. Tegel and D. Johrendt, *Phys. Rev. Lett.,* vol. 101, p. 107006, 2008.

[80] Z. Fisk, et al., *Science,* vol. 239, p. 33, 1988.

[81] C. Varma, Z. Nussinov and W. V. Saarloos, *Phys. Rep.,* vol. 361, p. 267, 2002.

[82] M. Girtu, et al., *Phys. Rev. B,* vol. 61, p. 4117, 200.

[83] J. Wu, et al., *J. Phys.: Condens. Matter,* vol. 22, p. 334211, 2010.

[84] E. Ruiz, et al., *J. Phys. Chem. B,* vol. 110, p. 115, 2006.

[85] T. Park, et al., "Phys. Rev. Lett.," *2005,* vol. 94, p. 017002, 2005.

[86] K. Fischer and J. Hertz, Spin Glasses, Cambridge University Press, 1993.

[87] R. Bachmann, et al., *Rev. Sci. Instrum.,* vol. 43, p. 205, 1972.

[88] M. Collins and O. Petrenko, *Can. J. Phys,* vol. 75, p. 605, 1997.

[89] V. Dobrosavljevic and E. Miranda, *Phys. Rev. Lett.,* vol. 94, p. 187203, 2005.

[90] T. Vojta and J. Schmalian, *Phys. Rev. B,* vol. 72, p. 045438, 2005.

[91] M. Brando, et al., *J. Phys.: Conf. Ser.,* vol. 200, p. 012016, 2010.

[92] H. Westfahl, J. Schmalian and P. Wolynes, *Phys. Rev. B,* vol. 68, p. 134203, 2003.

[93] G. Squires, Introduction to the Theory of Thermal Neutron Scattering, Dover Publications, 1997.

[94] J. Wu, et al., *EPL,* vol. 93, p. 67001, 2011.

[95] V. F. Sears, *Neutron News,* vol. 3, no. 3, 1992.

[96] K. Narayan and N. Kumar, *App. Phys. Lett.,* vol. 79, no. 12, pp. 1891-1893, 2001.

[97] J. Gardner, et al., *Unpublished data,* 2011.

[98] J. Gardner, et al., *Unpublished data,* 2010.

[99] F.M. Werner and S.A. Solin, *Unpublished data,* 2011.